Direct Force Control for the ICE aircraft

A novel control strategy

Daniël Douwes

September 6, 2019

TUDelft
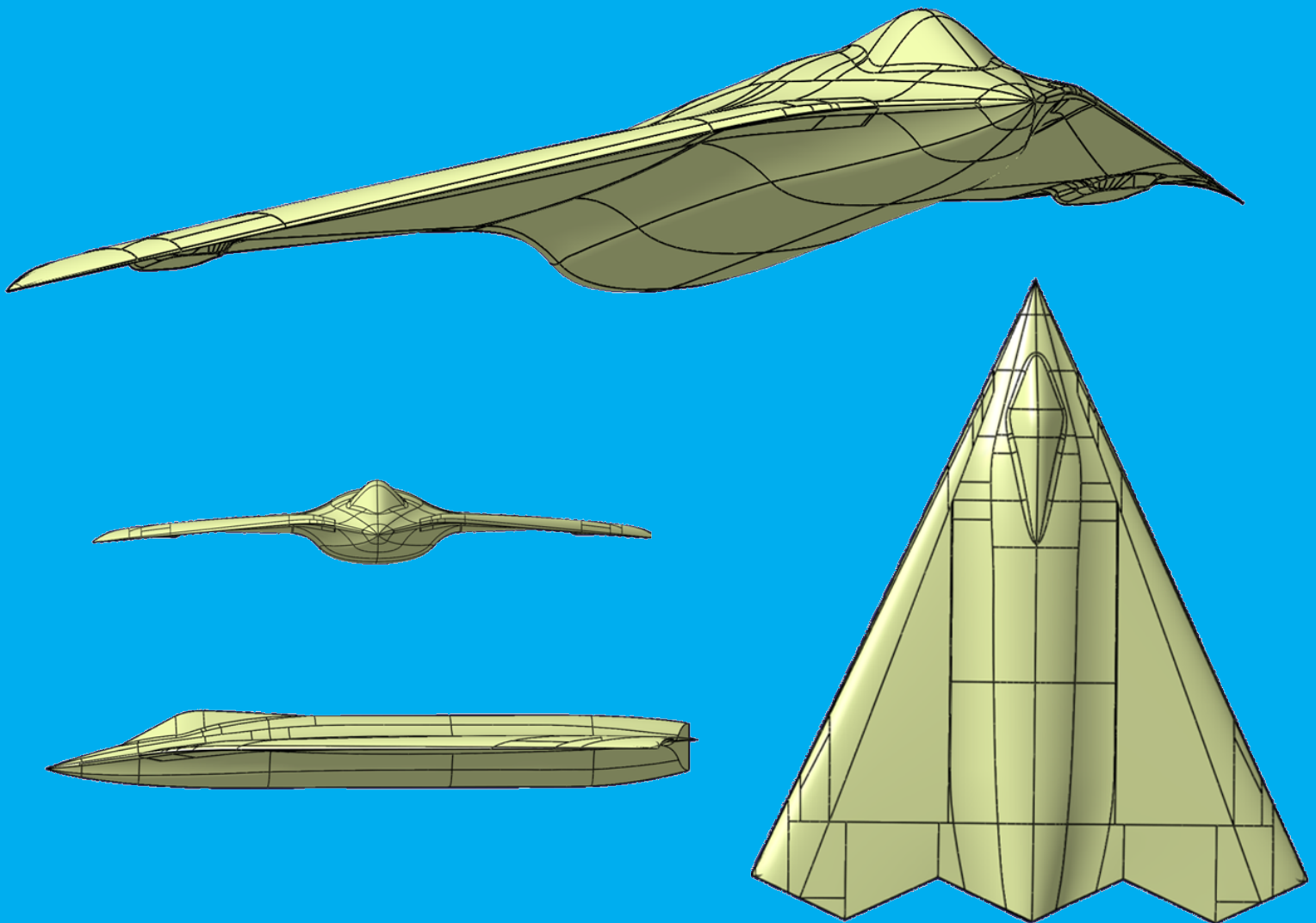
Direct Force Control for the ICE aircraft

A novel control strategy

by

Daniël Douwes

to obtain the degree of Master of Science
at the Delft University of Technology,
to be defended publicly on September 6th 2019 14:00 at Lecture Hall D of the Faculty of Aerospace
Engineering

TU Delft

Summary

Direct Force Control (DFC) in aircraft is the ability to control forces acting on the aircraft body by control effector deflection. This stands in contrast to the conventional method of controlling forces by means of attitude control. Although not a new concept – researched as early as 1963 – usage of DFC in the aircraft industry is sparse. Currently, there is only a a single aircraft which uses DFC as a control strategy: the F-14 Tomcat uses Direct Lift Control (DLC) to control descent rate during carrier approaches. The most important reason for the sparse use is that it requires a control effector suite capable of directly controlling the three moments around the body axes and the three forces along these axes. Conventional aircraft can control all three moments directly by means of elevators, ailerons and rudder and use thrust to directly control axial force. Conversely, they lack the capability to control lateral and vertical force directly and as such are under-determined for these control methods.

The Innovative Control Effectors (ICE) aircraft is a tailless flying-wing fighter aircraft with thirteen control effectors. As such, it is over-actuated and its Control Allocation (CA) problem is under-determined for control of three rotational as well as all six Degrees of Freedom (DoF). Previous research has provided with a Flight Control System (FCS) and CA algorithm capable of solving this problem for three Degrees of Freedom with good results. This thesis builds on that research by investigating the possibility of controlling all six Degrees of Freedom directly.

The Control Allocation algorithm was adapted and made suitable for 6DoF inputs. Usage of control input weights enabled analysis of control effector force generation capacity for each separate body axis as well as combined lateral and vertical forces. This yielded acceleration envelopes for different angles of attack (AoA) and sideslip. If was found that vertical acceleration envelope is strongly influenced by AoA, which is not the case for lateral acceleration and sideslip. A body acceleration feedback loop was implemented and a hedge function based on AoA was implemented for commanded vertical acceleration to counter saturation of the CA algorithm due to unachievable vertical commands.

An additional feedback loop with PID control for body velocities was implemented. The architecture for thrust control was changed from a control loop based on airspeed to a control loop based on commanded axial force as input, permeating the DFC philosophy throughout the control architecture. By using desired axial velocity as input to the inner loop for axial force and thrust, airspeed control was markedly improved. In addition, good command of lateral and vertical velocities up to 20 ft/s – expressly chosen as test speed because such speeds are more than sufficient for the primary use case – was achieved, marking the completion of inner control loop design.

Air-to-air refueling was tabbed in advance as the main use case. The goal was to test tanker tracking performance during steady straight flight and steady turns for different turbulence conditions. A basic tanker model based on KC-135 data was designed and placed in the same simulation as the ICE aircraft. The end of the boom mounted aft of the aircraft provided the aiming point for the ICE aircraft. A simple radar system was designed to mimic real-life boom tracking and tanker state relay.

A comparison between a conventional FCS and a DFC FCS was made with use of this set-up. Tracking performance for turbulence-free steady straight flight proved to be similar, but the DFC system clearly proved to be superior for steady turns. Turbulence rejection was also much better for the DFC system under all conditions. Especially axial and lateral errors were 10 to 100 times larger for the conventional system. Vertical error was also larger for the conventional system, although there was a semblance of convergence for very high turbulence for all situations except for conventional 30° turns.

High-crosswind landings were studies by design and testing of various control strategies. Three different control strategies for both lateral and vertical control were designed to test performance on high-crosswind landings with no, partial or full DFC employment. A standard 3° glide slope to the start of a runway formed the reference track with a flare command starting at 30 ft altitude at the end. To better judge lateral error response, a 300 ft lateral offset was implemented.

The best strategy proved to be controlling lateral error by roll control and controlling vertical error by a hybrid strategy of pitch angle control based on dynamic pressure and direct vertical error control by vertical force control. Fully conventional control provided with faster vertical closure but also was less stable due to roll-pitch coupling, a issue not present in the hybrid strategy. Full DFC control in combination with dynamic pressure pitch control provided superior landing situations but lacked approach path stability. Re-weighting partially solved this issue but was also deemed to be more of a symptom-combating tactic than a permanent solution.

Recommendations for further research are directed both inward and outward. Inward research should pertain to development of a global optimum finder to enable better sustained force command performance. In addition, studies into INCA parameter usage, review of control loop design and possible mode blending could enhance DFC-enabled ICE performance in different situations. Outward research should look at DFC benefits in manual control tasks comparable to the presented benefits for automatic control tasks. Additionally, reflection of DFC possibilities in areas such as fault-tolerant control, flight envelope protection and upset recovery might reveal new areas of interest and application.

Preface

This thesis is the result of nine months of research into a novel control concept. I have tried to embrace the challenge of combining a relatively old and little-used control concept with an innovative aircraft design as much as possible. The fact that there was little previous research has proved to be both a blessing and a curse; getting to choose your own path is as much a liberty as it induces a feeling of flying blind.

Luckily, I did not have to pave this path alone. Therefore, I would like to express thanks first and foremost to my supervisor Coen de Visser. He enthused me from the preliminary meeting we had about this subject and has helped me stay motivated throughout this thesis project. His great mix of encouragement, collaborative thinking and straight-to-the-point but constructive criticism has been of great support. In addition, thanks is in order to everyone who has contributed to the development of this amazing aircraft, in particular Mike Niestroy and Kenneth Dorsett. Without their efforts over the past 2+ decades, this project would not have been possible.

Daniël Douwes

Delft, August 2019

Nomenclature

Acronyms

AMT	All Moving Wing Tips
AoA	Angle of Attack
AS	Active Set
AT	Auto-Throttle
CA	Control Allocation
CCV	Control-Configured Vehicles
DFC	Direct Force Control
DLC	Direct Lift Control
DoF	Degree of Freedom
DSFC	Direct Side Force Control
ELE	Elevator
FCS	Flight Control System
FDM	Flight Dynamics Model
ICE	Innovative Control Effectors
INCA	Incremental Nonlinear Control Allocation
INDI	Incremental Nonlinear Dynamic Inversion
LCA	Linear Control Allocation
LED	Leading Edge Down
LEF	Leading Edge Flap
LEU	Leading Edge Up
LM	Lockheed Martin
LMTAS	Lockheed Martin Tactical Aircraft Systems
MAC	Mean Aerodynamic Chord
MRC	Moment Reference Center
MTV	Multi-axis Thrust Vectoring
PF	Pitch Flap
PID	Proportional, Integral and Differential
QP	Quadratic Programming
RCS	Radar Cross Section

SSD	Spoiler-Slot-Deflector
TED	Trailing Edge Down
TER	Trailing Edge Right
TEU	Trailing Edge Up
USAF	United States Air Force
VOR	VHF Omni-directional Range

Superscripts

$\dot{\diamond}$	Time derivative of variable $\diamond$

Greek Symbols

α	Angle of Attack
β	Angle of Sideslip
γ	Flight path angle
δ_i	Control effector i deflection
$\Delta\delta_c$	Set of commanded actuator deflection increments
θ	Pitch Angle
$\Delta\boldsymbol{\tau}_c$	Set of commanded moment and force increments
$\Delta\boldsymbol{\tau}_{Rc}$	Set of commanded moment increments
$\Delta\boldsymbol{\tau}_{Tc}$	Set of commanded force increments
φ	Roll Angle
χ	Course angle
ψ	Heading Angle
ω	Set of body angular rotations

Latin Symbols

a_{nn}	Command weight of DoF n
b_{ref}	Reference span
d_t	Tanker separation distance
$\mathbb{F}_*$	*-frame
h	Altitude
$I_{xx,yy,zz,xz}$	Moments of Inertia
J_R	Rotational Jacobian matrix
J_F	Full Jacobian Matrix
J_T	Translational Jacobian Matrix
K_D	Derivative gain column

K_I	Integral gain column
K_P	Proportional gain column
P	Position vector
p	Roll rate
q	Pitch rate
r	Yaw rate
S_{ref}	Reference wing area
S_l	Lateral approach strategy
S_v	Vertical approach strategy
$\mathbb{T}_{AB}$	Transformation matrix from frame B to frame A
$\mathbf{u}$	Commanded actuator deflections
$\mathbf{u}_p$	Set of preferred deflections
$\underline{\mathbf{u}}, \overline{\mathbf{u}}$	Minimum, maximum actuator deflections
$u\,v\,w$	Body velocities
V_0	Trimmed body velocities
V_{app}	Final approach speed
v_b	body velocity vector
V_{des}	Desired Airspeed
v_E	Earth-centered velocity vector
V_{TAS}	True Airspeed
$W_{\mathbf{d}}$	Command weighting matrix
$W_{\mathbf{u}}$	Deflection weighting matrix
$[x, y, z]_{cg}$	x-, y- and z-location of Center of Gravity

Subscripts

a	Actual
b	Body
c	Commanded
d	Relative to tanker
e	Error
I	Related to ICE aircraft
t	Related to tanker

List of Figures

List of Tables

Contents

1

Introduction

The advent of fourth-generation fighter aircraft gave rise to new control techniques such as Multi-axis Thrust Vectoring (Su-27 in 2D, MiG-35 in 3D) and flying characteristics like good post-stall control. These techniques warranted an investigation into the possibility of combining such technologies and flying characteristics into a fighter with a small-as-possible radar signature, or Radar Cross Section (RCS) . Aircraft without a vertical tail have a much smaller RCS, but lack lateral-direction control authority. All of the above prompted a program jointly sponsored by the United States Air Force and Navy to study "innovative aerodynamic control concepts for fighter aircraft without vertical tails" (Dorsett and Mehl, 1996).

The concept was called the Innovative Control Effectors aircraft and the result of the program was a set of designs for such a tailless agile fighter aircraft: one land-based version and one carrier-based version. The aerodynamic model data for the land-based version was re-released in a comprehensive paper by Niestroy et al. for research purposes. The ICE's heavily under-determined control allocation problem – thanks to its thirteen control effectors – paves the way for research into control methods using different strategies than conventional aircraft.

The research objective of this thesis is to develop a Direct Force Control method for the ICE aircraft which allows for translation without rotation and rotation without translation. This will be done by constructing a control system based on the Incremental Nonlinear Dynamic Inversion (INDI) approach (see Sieberling et al., 2010) analogous to the Incremental Nonlinear Control Allocation (INCA) method presented by Matamoros and de Visser (2018). This control system will be capable of solving a three-force problem and will subsequently be combined with the existing controller. The fulfillment of this objective will be tested by means of a number of use cases.

The line of reasoning behind this research objective is the following: now that the ICE aircraft has been made controllable in the traditional sense, the next step in fully exploiting the control effector suite is to find novel ways to control the aircraft. Considering the fact that the three moment problem as described by Durham (1994b) has been solved, the next step would be to extend the controller in order to solve a so-called "three-force" problem. This means that in addition to realizing a commanded net moment *around* the X-, Y-, and Z-axis of the aircraft, the controller is able to realize commanded net forces *along* the X-, Y, and Z-axis. It must be noted that the objective is to realize net forces *without* generating net moments.

This research objective cannot be realized at once; it is a multi-faceted problem with numerous uncertainties that have to be dealt with first. The process of solving these uncertainties is guided by four main research questions and a number of sub-questions. These will be given in the next section. Each main question will shortly be elaborated upon to clearly establish the purpose and validity of that particular part of the research.

The research questions treated in this thesis are stated below. They are split in four main research questions with a number of subquestions for all of the four.

1. Is the current control method suitable for adaption into a three-force problem?
   - Is a 1-to-1 adaption of the three-moment problem to the three-force problem technically feasible?

    – Are the current inner- and outer-loop state inputs sufficient for the three-force control problem?
    – Which adaptions do the control loops require for use as a direct force control system?
    – Is it possible to generate rotation-free translational motion?

2. Does the direct force controller perform adequately in terms of performance parameters used to evaluate flight control systems?

    – Which performance parameters can be of use for evaluation of this particular type of control system?
    – Does the control system meet these parameter thresholds?
    – Does the INCA control method provide sufficiently large actuator saturation margins when used in the three-force problem?
    – Which range of direct force commands can be attained with sufficiently small tracking and allocation errors?

3. Which control architecture enables the simultaneous use of both types of control systems?

    – Is it possible to ensure smooth transitions from direct force control to conventional control and vice versa?
    – Is it possible to construct a multi-objective control scheme enabling use of both direct force control and conventional control?
    – Can the multi-objective controller handle every type of control input in every situation in a stable manner?

4. Which specific types of special maneuvers can be achieved using this controller?

    – Is it possible to create an autopilot able to fly conventional trajectories while using both direct force and conventional control with a sufficiently small tracking error?
    – Can the multi-objective controller be used to improve on the current method of air-to-air refuelling?
    – Can direct force control be used to perform high-crosswind landings without the need for yawing and/or rolling?
    – Is it possible to generate translation-free rotations?
    – Can a semi-vertical (cobra) landing be performed?

The remainder of this thesis is structured as follows. The current state of DFC research is treated in chapter 2. The posed research questions are related to topics of study and available prior research for each of those topics is discussed. An in-depth look into the ICE aircraft is available in chapter 3, with effector suite, aerodynamic data origin, model properties and DFC opportunities all being treated. The core thesis content is split into two parts. The development of a DFC-enabled Flight Control System can be found in chapter 4. Making use of this FCS, two use cases are designed, tested and evaluated in chapter 5. Finally, conclusions and recommendations are given in chapter 6.

2

Direct Force Control state of affairs

The set of research questions posed in chapter 1 can be reformulated into a number of topics that serve to identify key areas of the literature review. Each main research question differs significantly from the other questions in terms of theoretical basis and technological development, which is why each topic has its own section in this chapter.

First, the technological basis onto which this research project will commence is discussed in section 2.1. Then, each subsequent section will briefly state the research question it pertains to, as well as the main subject kept in mind during review of relevant literature. Next, important theory and technology in the subject area are discussed. Any possible gaps between question and found answers are discussed as well.

2.1. Technological starting point

The starting point of this research project, as mentioned in chapter 1, is the INCA-based FCS constructed by Matamoros and de Visser for the ICE aircraft. This paper combines numerous technologies into one FCS. The constructed FCS is applied onto the ICE aircraft design (see fig. 2.1a) detailed in Dorsett and Mehl (1996) and Dorsett et al. (1997). The basic aerodynamic data sets for this aircraft have been described and made available by Niestroy et al.. These data sets have been transformed into a multivariate B-spline model using the method in Tol et al. (2016) in order to make optimal use of the data.

Figure 2.1: Two visualizations of the ICE model

(a) A 3D impression of the ICE aircraft (Niestroy et al., 2017)

(b) 2D indication of control effectors (Matamoros, 2017)
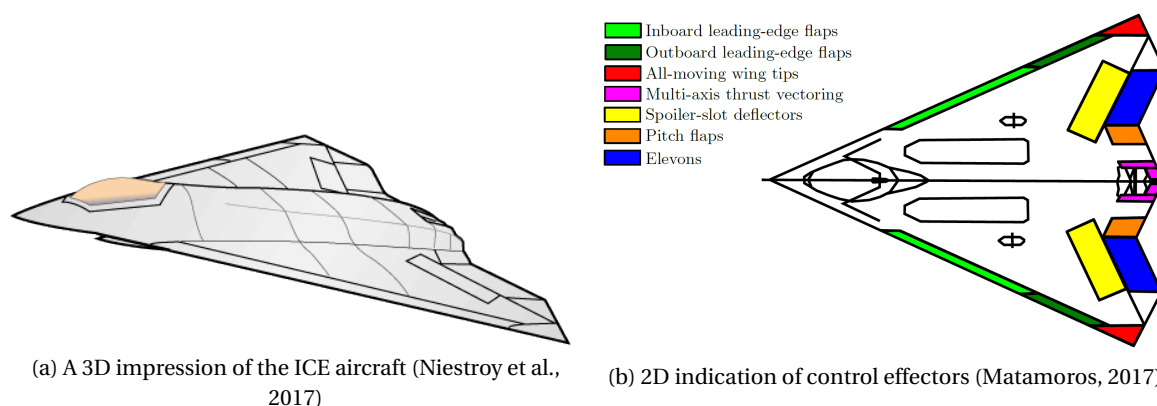
The challenge posed by the unconventional control effector suite of the ICE aircraft (see fig. 2.1b), is threefold:

1. The aircraft exhibits a high degree of control nonlinearity
2. There exist many effector interaction effects
3. The number of control effectors (13) is much higher than the number of controlled moments (3)

The first two points are well-illustrated by Matamoros (2017, p. 27-28). Therefore, the assumptions made by Durham (1993) concerning the linearity of controls does not hold anymore, making use of Linear Control

Allocation (LCA) problem solvers less effective. Hence, the need arises for a nonlinear solver that can deal with such problems. (For a comprehensive overview of both linear and nonlinear control allocation problem solvers, see the survey by Johansen and Fossen (2013))

The third point mentioned above causes the three-moment problem as described by Durham (1994b) to become highly under-determined and much more complicated. A higher degree of complexity places more stringent requirements on the real-time capacities of the used solver. Matamoros and de Visser demonstrate a number of candidate solvers for both an LCA- and INCA-based FCS. The solver based on Härkegård's Active Set (AS) method showed very promising results both in terms of tracking error and real-time performance.

2.2. Direct Force Control

The demonstrated successful implementation of an FCS able to accurately control the moments acting on the aircraft opens the door to new possibilities. As stated in chapter 1, the counterpart of angular acceleration control is translational acceleration control: manipulation of forces instead of moments. This section of the literature review therefore is concerned with the following question: which methods already exist to generate a pure net control force acting on an aircraft? The search has been divided into three parts; one part for each aircraft body axis. Footage from the San Diego Air and Space Museum of a modified F-16 brilliantly demonstrates the principles of direct force control discussed in the following subsections.

2.2.1. Direct Lift Control

The most prevalent force direction is the one of forces acting along the Z-axis: weight and lift[1]. Weight is dependent on aircraft configuration, payload, fuel usage, etc and cannot be manipulated in-flight without taking rigorous measures (e.g. fuel dumping or payload usage). What's more, weight can only be reduced, causing each manipulation of the force caused by weight to be non-reversible. Therefore, weight manipulation is not taken into account when looking at force control along the Z-axis.

This leaves manipulation of the lift force. Changing the lift force without causing a rotation is called Direct Lift Control. The concept of DLC has been the subject of a number of studies, including simulations (Douglas Aircraft Company, 1963, Grantham et al., 1971, Johnson et al., 1969) and flight tests in which different variations of DLC systems were tested, like symmetric ailerons connected with elevators (Stickle et al., 1968) and exhaust-blown main flaps, both standalone flights (Taylor Jr., 1969) and verified with wind tunnel data (Rolls et al., 1969). The aforementioned reports were mainly focused on demonstrating the use of DLC and the application into corrections during landing approaches. Pinsker (1968) first presented a comprehensive overview of the theory behind DLC, as well as desireable control characteristics of DLC systems.

DLC technology eventually developed into so-called Control-Configured Vehicles (CCV) , as described by Rynaski and Weingarten (1972). The CCV subject contained much more than simply DLC, however. Its subject matter also included the use of active controllers, deliberate destabilization of aircraft and drag minimization methods, for example. Further development of CCV was supported by flight tests with a B-52 aircraft utilizing CCV technologies, documented in Arnold and Murphy (1973). The same year, Mcneill et al. performed research on the possibilities of using CCV techniques, especially DLC, when performing precision flight tasks. They state that "Initial flight tests using *DLC* indicated that the task of formation flying and, hence, in-flight refueling could be eased by actuating the *DLC* flaps through the conventional control stick", indicating the potential improvements in precision control enabled by DLC in such flight scenarios.

An example of a more modern aircraft making use of DLC is the F-14 Tomcat. According to the pilot manual for the F-14D, enabling the DLC mode puts the spoilers in a higher-than-normal position, slightly reducing lift. To compensate for the change in pitching moment, the elevators are trimmed down slightly (United States Navy, 2004). If the pilot wants to increase descent rate, rolling a thumb wheel on the control stick forward puts the spoilers at a larger angle, losing more lift. The reverse occurs if the pilot wants to decrease descent rate by rotating the thumb wheel aft. Figure 2.2 illustrates the position of the thumb wheel on the F-14 control stick. The fact that the larger-than-zero neutral position of the spoilers sacrifices some lift is offset by allowing the use DLC only when flaps are extended to counter said loss of lift. The approach is the only flight scenario, however, in which DLC can be employed.

---

[1] Note that, strictly speaking, the Z-axis only coincides with the weight and lift force vectors when pitch & roll angle and angle of attack are zero, respectively. It can be assumed that these angles sufficiently small for steady straight symmetric flight conditions that the small-angle approximation holds.
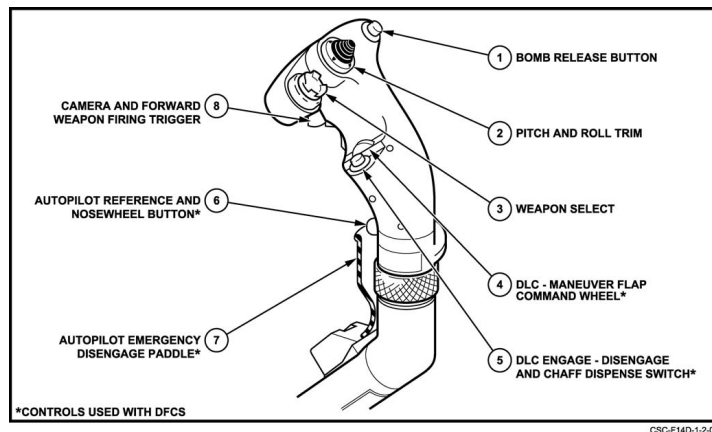
Figure 2.2: Illustration of the thumb wheel (No. 4) used with DLC
(United States Navy, 2004)

The example of the F-14 illustrates the limited deployment of DLC as an auxiliary maneuvering technique. Other areas like gust load alleviation have been explored as well (see Schänzer, 1977, Wang et al., 2017). Attempts have also been made to implement DLC as a tool to increase maneuverability while also developing handling criteria for the control method (Tomczyk, 1998, 2005). Research has also been performed on the topics of combining DLC with a predictor-tunnel display to improve trajectory control in simulations (Sachs and Holzapfel, 2008) and decoupling of flight path control and pitch angle (Zhou, 1995, Liu et al., 2011, Moravszki et al., 2018).

It must be noted that the research mentioned in this section nearly exclusively pertains to classical aircraft configurations in which there is a distinct separation of main wing and horizontal tail surfaces, a situation that does not hold for the ICE configuration. The decades of research, however, show that there is a sound theoretical and technological basis from which can be drawn when designing a DLC controller for the ICE aircraft. Furthermore, the developed guidelines for DLC handling parameters still can be applied when evaluating a DLC system. It also stands to reason that the application of thrust vectoring opens up new possibilities in this area that can mitigate the lack of dedicated elevators.

2.2.2. Longitudinal Force control

The second symmetrical direction in which force control can be exerted is along the X-axis by controlling thrust and drag[2] forces. It must be noted that for drag, the interest lies only in control methods which alter the drag force without having a mayor impact on the magnitude of lift. Therefore, control methods like spoilers are not considered, since the use of such devices also greatly impacts lift besides altering drag.

Most devices commonly called airbrakes or speedbrakes are therefore not applicable to this type of control, as most speedbrakes on commercial airliners are in fact spoilers. However, studies by Mertol (2008) and Cui et al. (2018) have conducted research into the aerodynamic effects of different types of airbrakes not considered spoilers. The main points of interest in these studies is both the magnitude of the created drag as well as the side effects created by employing these control surfaces. Implemented examples of speedbrakes include the double spoiler on the aforementioned F-14 (United States Navy, 2004, p.2-95) and the well-known application of split rudders on the B-2 which can double as speedbrakes.

The other possibility of longitudinal force control is altering thrust. The engine dynamics of the ICE model do not include any form of lag, which makes any changes in commanded thrust instantaneous. This assumption is not likely to hold in reality, as it can be assumed that produced thrust does not follow commanded thrust without any form of lag. Due to the secretive nature of the properties of jet engines, such engine models are very hard to obtain. If quickly obtaining such information proves impossible, a conservative best guess can serve as a placeholder until the model can be appended with the correct engine dynamics. In addition, longitudinal force control using incremental drag control can be expected to yield more reliable results due to this (temporary) lack of engine information and should therefore be considered the preferable option.

---

[2]Again, it is assumed that the angle of attack is sufficiently small to assume that the drag force is aligned with the X-axis.

2.2.3. Lateral force generation

The third and final direction of force control pertains to forces along the Y-axis. In principle, a perfectly symmetrical aircraft should not experience any net lateral forces during normal flight conditions due to the cancellation of equal and opposing forces on both sides of the X-Z symmetry plane. In conventional aircraft control suites the vertical tail provides directional stability by serving as a stabilizing surface when experiencing sideslip and the rudder acts as a control effector able to exert a lateral force on the aircraft. The lateral control authority of the rudder, however, is not used very often: straight symmetrical flight does not require for rudder control and aircraft usually make coordinated turns, which are by definition turns without any side force acting on the aircraft.

Nonetheless, preliminary research by Jenkins (1973) and Mercier and Duffy (1973) investigated Direct Side Force Control (DSFC), a means to improve lateral control authority. By simulating the application of DSFC, they showed that this technique could be of great benefit in flight conditions like final approaches with limited visibility and high-crosswind landings. Their methods of applying DSFC are limited, however, as Jenkins only names the use of vanes directing engine exhausts laterally, whereas Mercier and Duffy lists a very large number of options, none of them very feasible, except for thrust vectoring. None of these methods were tested in real-life flight scenarios. Further simulation research on full lateral control in dive bombers (Brulle, 1977) strengthens the pilot-supported point that DFC is best applied by using a thumb-controlled button on the joystick as well as providing with (un)acceptable coupling characteristics to be kept in mind.

Later research by Grunwald and Stengel (1985) provides an elaborate theoretical model for full lateral control authority as well as an in-depth flight study into the actual performance of said model. The problem with this study, however, is the fact that the aircraft used during flight tests employs both a vertical tail as well as two vertical-canard-like structures (dubbed side force panels by the authors) intersecting either wing around the midpoint. Also recall the footage from the San Diego Air and Space Museum: the additional canards are required in order to counter the yawing moment created by the rudder side force. Without them, pure lateral translation would be impossible. The total absence of both these surfaces as well as a vertical tail and rudder on the ICE aircraft further compounds this issue.

There have been a number of studies into the problem of directional stability and control for aircraft without a tail, however. Gillard and Dorsett (1997) summarized the effectiveness of All Moving Wing Tips (AMT) in terms of yaw control over a wide range of angles of attack by using data gathered in (Dorsett et al., 1997). Research by Ngo et al. (1996) led to a two-loop FCS for a tailless aircraft similar to the ICE aircraft able to provide combined longitudinal and lateral control. An indirect adaptive control strategy for tailless aircraft was proposed by Eberhardt and Ward (1999) to optimize interaction between parameter estimation and control allocation. The notion that these designs mainly focus on AMTs as yaw control effectors indicates that there could be unexploited gains in the area of thrust-vectoring yaw control.

2.2.4. Three-force problem conversion

It has been demonstrated that a large number of studies have already addressed the topic of Direct Force Control, most notably in the vertical direction. Unfortunately, there is little subject matter on the topic of solving a three-force problem for aircraft. The application of the three-force problem has been partially implemented in Gai et al. (2018). In Mitchell and Vogel (2003) the authors demonstrate promising force control authority along the X- and Z-axes combined with pitch control using an INCA-based FCS for a Canard-Rotor-Wing vehicle. This method is not directly applicable for the ICE aircraft, however, as the control suites differ greatly. Its usefulness is also limited due to the lack of control in the three asymmetric degrees of freedom.

It might be possible, however, to base the three-force problem architecture on the the control method used for the FCS in Matamoros and de Visser (2018), which uses a Jacobian matrix containing the incremental control moments generated by the control effectors. In that case, a Jacobian containing the incremental control forces is required. To this end, Van Oorspronk (2018, p.14) gives the general definition of the entire Jacobian matrix, which therefore also contains the incremental control force coefficients. No use is made of these coefficients, however, as he states that "Calculating the dynamic inversion ... only requires the Jacobian of three moment coefficients l,m,n" (Van Oorspronk, 2018, p.32). The availability of the desired partial Jacobian therefore is not expected to be an issue, but successful implementation in an FCS employing control in all three force directions has yet to be demonstrated. This can therefore be seen as a crucial component to the successful development of said FCS. For a full derivation of the Jacobian of a multivariate B-spline simplex function such as the one used for the aerodynamic data set, please refer to appendix A.

2.3. Direct force control performance evaluation

The next part of the research will pertain to the evaluation of the DFC FCS that has been constructed for the ICE aircraft model and relates to the question "does the direct force controller perform adequately in terms of performance parameters used to evaluate flight control systems?". Prior research by Pinsker (1968), Hoh et al. (1981) and Tomczyk (2005) has identified key performance indicators to be used in DFC applications. Further research must be performed, however, to determine which parameters are most suitable for evaluation of the constructed FCS. This is due to the fact that the aforementioned research pertains to classical *manned* aircraft, whereas the ICE aircraft could be developed into an *unmanned* fighter to relax maneuvering limits normally applied to manned fighter jets. It might therefore be necessary to re-define parameter limits.

Additionally, the stability characteristics of the INCA FCS must be determined. Recent research has yielded methods that can be applied when working with INDI-based systems (van 't Veld et al., 2018, Wang et al., 2018). Furthermore, the range of attainable force commands has to be determined. However, a search into the attainable forces problem did not yield any results. Therefore, the best apparent approach right now seems to be mirroring the method used when determining the attainable moments set as described by Durham (1994a) and refined for nonlinear systems in (Bolender and Doman, 2004). It remains to be seen if this approach proves effective as no further literature on the subject could be found.

2.4. Simultaneous FCS usage

The main topic of the third part of this research is the simultaneous usage of two flight control modes. As shown in the case of the F-14 (DLC) and the CCV F-16 (full translational control), the DFC mode is manually controlled by an auxiliary device operated by the thumb. Therefore, sequential manual operation of both the existing FCS and the to be constructed FCS is possible due to separation of control inputs.

It does, however, become a more complex multi-objective control allocation problem when both systems simultaneously receive inputs. In fact, due to the primary (commanded moment) and secondary (minimizing control effort) optimization goals already implemented by Matamoros and de Visser, the simultaneous use of both FCS systems would create a dual primary-secondary control allocation problem. It stands to reason that a reformulation of such a parallel situation into a single primary and a single secondary goal can be beneficial for both controller effectiveness as well as real-time performance.

As already mentioned, current literature does not provide with a large theoretical basis on this subject, the adapted version of the combined force-moment problem described in Gai et al. (2018) being a rare exception. They rewrite the control allocation problem into the form of a sequential quadratic programming problem and use the methods in (Härkegård, 2004). However, sound arguments are given by Matamoros and de Visser for selection of the control allocation problem solving method outlined in (Härkegård, 2002). Therefore, a more in-depth analysis is needed in order to select the best method for the newly formulated control allocation problem.

2.5. Special Maneuvers

The last part of the research is interested in the execution of a number of special maneuvers making use of the both the conventional and the force control FCS. Of special interest is in-flight refuelling, which was already identified by Mcneill et al. as a flight task of interest that can be made easier by using direct force control. NATO Standardization Organization (2013, p.2A-2) documentation provides standard refuelling patterns that can be implemented in a model for testing FCS tracking performance during refuelling.

Other areas of interest could be high-crosswind landings without sideslip or bank, effectively creating the same landing attitude and trajectory as zero-crosswind landings. The limitations of this maneuver would be the maximum attainable side force in landing configurations to counter such crosswinds. This maneuver could find application in landings on aircraft carriers, for example, where there is very little time and space to correct nonzero sideslip and bank angles right before touchdown. Straight landing trajectories would greatly improve safety in such situations.

A final special maneuver is the use of Pugachev's Cobra (described in Joyce 2014, p.81) in high-speed approaches, e.g. to enable steep flight paths. In this maneuver, the Cobra is performed right before the landing in order to lose a lot of airspeed and touch down at a reasonable velocity. This maneuver is hardly ever used outside of airshows, let alone before landing, but simulation footage by CHRISXTR3M3GAMING (2015) demonstrates a cobra landing. The ICE aircraft's thrust vectoring and high AoA control properties make it a good candidate for executing such a type of landing.

3

ICE Aircraft

The origin of the Innovative Control Effectors aircraft is a novel aircraft concept developed by Lockheed Martin Tactical Aircraft Systems (LMTAS). The goal was a new, tailless, agile fighter with a low RCS. The design should also use multi-axis thrust vectoring systems yielding increased high-AoA control demonstrated in fourth-generation fighters such as the Su-27 and prototype versions of the F-16 (Dorsett and Mehl, 1996). To this end, a joint research program was created to investigate possible designs.

This program consisted of two phases. The purpose of the first phase was to identify suitable land- and carrier-based planforms as well as investigate five innovative actuator types of interest Dorsett and Mehl (1996). Study topics were RCS, aerodynamic testing, structural modelling, stability analysis and control law design, among others. This study resulted in the identification of the three most promising control concepts and their proposed utilization in both ICE types.

The second phase consisted of a more thorough study into the two proposed configurations. The main goal of this phase was to better identify the stability, control and performance of the two previously chosen designs. Gathering more data on the aforementioned control effectors was an important secondary objective. Research areas included high-speed wind tunnel testing, rotary and balance tests and stability & control analysis, primarily for yaw control (Dorsett et al., 1997). The data gathered in this study phase was re-released in the form of a research model in Niestroy et al. (2017). This research model forms the core of the model used in this thesis. As only the land-based ICE configuration – dubbed the Configuration 101 series USAF Baseline (Dorsett and Mehl, 1996) – was included in this research model, only the land-based version of the ICE aircraft has been studied.

This chapter is structured as follows. First, an overview of the effector suite configuration is discussed in section 3.1. The other model properties and data sets are treated in section 3.2. Next, section 3.3 will describe the challenges resulting from said configuration and review previous work done to account for these challenges. Finally, the link to the topic of DFC is made in section 3.4 by underlining the unexplored opportunities of the ICE aircraft.

3.1. ICE effectors
The ICE control suite consists of 7 different types of effectors. These are shown schematically in fig. 3.1. Each of those is briefly discussed, naming main purpose, strong and weak points and possible other notes of interest.

Leading Edge Flaps (LEF)
The leading edge flap system consist of two sub-parts: the inner and outer flaps. Positive deflection is Leading Edge Down (LED) for both systems, with the inner flaps being limited to LED deflections due to expected actuator integration and RCS issues. LED deflections cause an increase in yawing moment by means of increased suction, whereas Leading Edge Up (LEU) deflections cause adverse yaw. The ability to use differential deflections yields increased lateral-directional control at high AoA by means of redirecting the leading edge vortex system. Control effectiveness is nonlinear in both roll and yaw, in addition to a large degree of interaction between the inboard and outboard flaps (Dorsett and Mehl, 1996).

All-Moving Wing Tips (AMT)
The AMTs can be deflected from 0° to 60° Trailing Edge Down (TED) . By increasing profile and induced drag, TED deflections produce a yawing moment which is fairly constant over the full range of AoA tested. This makes the AMTs an outstanding source of yaw control, even at high AoA. When compared to an F-16 rudder, the AMTs provide similar control power, with the added benefit of sustained control for higher AoA. Trailing Edge Up (TEU) deflections are excluded, as the increased roll control does not weigh up to the adverse yaw produced above $\alpha = 10°$ (Dorsett and Mehl, 1996). Trailing Edge Down deflections do not suffer from said adverse yaw effects. In addition, TED deflections of the AMTs alone produce sufficient control power as an anti-spin measure, as well as being largely unaffected by either sideslip or rotation rate (Dorsett et al., 1997)

Spoiler-Slot-Deflectors (SSD)
The SSDs consist of two elements: an upper-surface and a lower-surface component. The upper-surface component acts like a conventional spoiler whereas the lower-surface component has the hinge aft of the surface and deflects the air upward. The spoiler and deflector are opened simultaneously to redirect air through the slot to the upper wing surface. Compared to a conventional spoiler, this configuration provides more lateral-directional control up to higher AoA. Unfortunately, SDD usage has detrimental effects on the effectiveness of the pitch flaps and elevons as well as required nose-up trim deflections. (Dorsett and Mehl, 1996). As with the AMTs, SSD yaw power is largely unaffected by sideslip or rotation rate and provides sufficient spin recovery control. Sideslip does have a significant effect on SSD roll power, however (Dorsett et al., 1997).

Elevons (ELE)
The elevons can be deflected up to 30° both TEU and TED, the latter being seen as positive deflection. The elevons are primarily responsible for roll control (asymmetric deflection) and pitch control (symmetric deflection). SSD usage limits the pitch control effectiveness, however, as Dorsett and Mehl note that the elevons alone are not enough to trim out the aircraft for $\alpha \geq 15°$. Elevons have little effect in yaw control, with either TEU or TED deflections of the right elevon producing small positive increments in yaw moment, fairly constant over the entire range of AoA (Dorsett et al., 1997).

Pitch Flaps (PF)
The pitch flaps, like the elevons, have a 30° TEU (negative) and 30° TED (positive) deflection range. They can only be deflected symmetrically, however, and as such only provide additional pitch control. According to Dorsett and Mehl, "small surfaces with pitch priority ... are invaluable for aircraft employing SSD concepts." The pitch flaps also alleviate elevon deflection requirements for longitudinal trim.

Multi-axis Thrust Vectoring (MTV)
The Multi-axis Thrust Vectoring system is able to deflect thrust around pitch and yaw axes. The thrust vectoring system contributes to both maximum roll control by means of elevon-induced yaw mitigation as well as high-AoA lateral-directional control (Dorsett and Mehl, 1996). The thrust-vectoring deflection limit is 15° from the aircraft X-axis in all directions using a low-observable multi-axis nozzle concept. A more modern approach would be using fluidic thrust vectoring control, however, as already alluded to by Bowlus et al.

3.2. ICE Model

The high-fidelity aerodynamic model presented in Niestroy et al. (2017) is based on five sets of wind tunnel test data and constitutes the core of the simulation model used to obtain the results presented in this thesis. The model contains six sets of coefficient data tables; one for each degree of freedom. Each set contains two, three or four airframe coefficient tables – depending on the degree of freedom – and fifteen control effector coefficient tables.

3.2.1. Model elements and properties

The Simulink model created by Lockheed Martin (LM) consists of a number of core elements. In addition to the aforementioned aerodynamic data tables, the model contains sub-models for actuator trim and dynamics, a thrust vectoring system, environment models – consisting of a wind model with horizontal wind, shear, continuous Dryden turbulence and discrete gusts, as well as a COESA atmospheric mode and the WGS84 gravity model – incidence angle calculation models and a 6DoF Euler state propagation block. The model's airframe reference data used in the ICE simulation block are taken from Niestroy et al. (2017) and are shown in table 3.1 below.
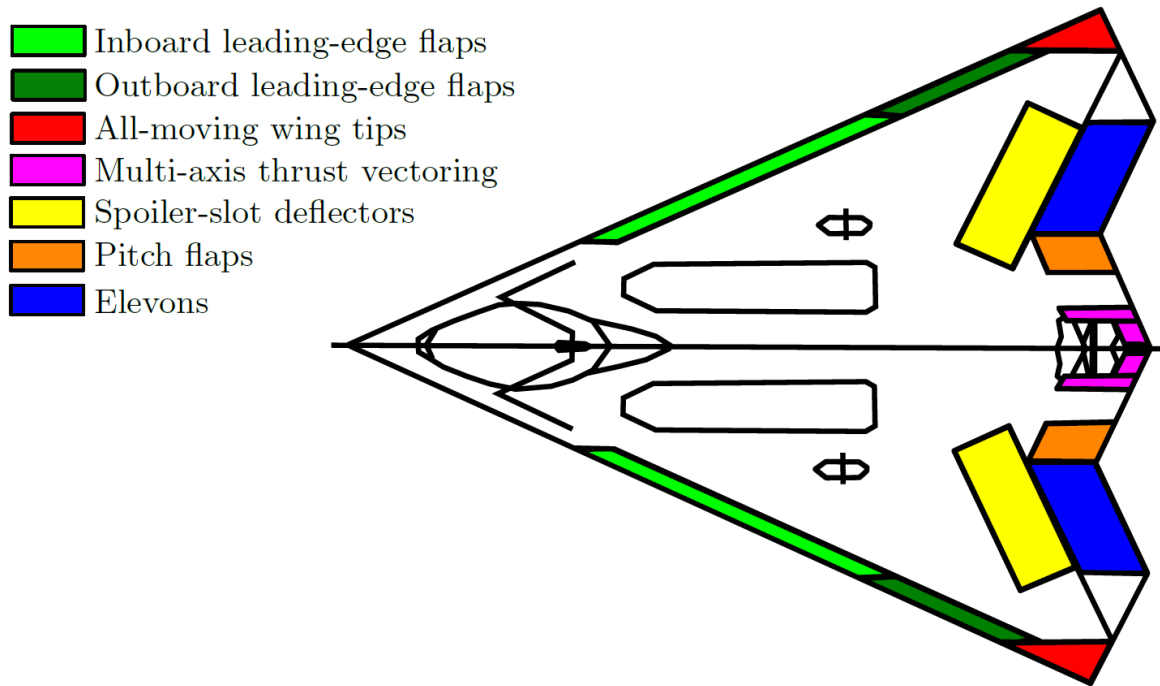
Figure 3.1: Top view of the ICE control effector suite Matamoros (2017)

Table 3.1: ICE model reference data

Parameter	Value
Reference wing area (S_{ref})	808.6 ft^2
Reference span (b_{ref})	37.5 ft
Mean Aerodynamic Chord (MAC)	345 in
FS LEMAC	160.84 in
Moment Reference Center (MRC)	38% MAC
WL MRC	100.0 in

The model is trimmed at a number of different airspeed, mass and altitude conditions. The three available mass configurations are given in table 3.2 below. All available combinations of airspeed and altitude are shown in fig. 3.2, with trimmed conditions highlighted. All data is taken from Niestroy et al. (2017). Weight is in lbf, CG location in inches and intertia in slug·ft^2.

Table 3.2: Mass configuration properties

Configuration	Weight	x_{cg}	y_{cg}	z_{cg}	I_{xx}	I_{yy}	I_{zz}	I_{xz}
Lightweight	25,989	40% $\bar{c}$	0	88.97	35,497	67,500	83,800	-250
Nominal (50% fuel)	32,750	38.84% $\bar{c}$	0	88.97	35,479	78,451	110,627	-525
Heavyweight	37,084	36% $\bar{c}$	0	88.97	42,576	81,903	18,379	-525
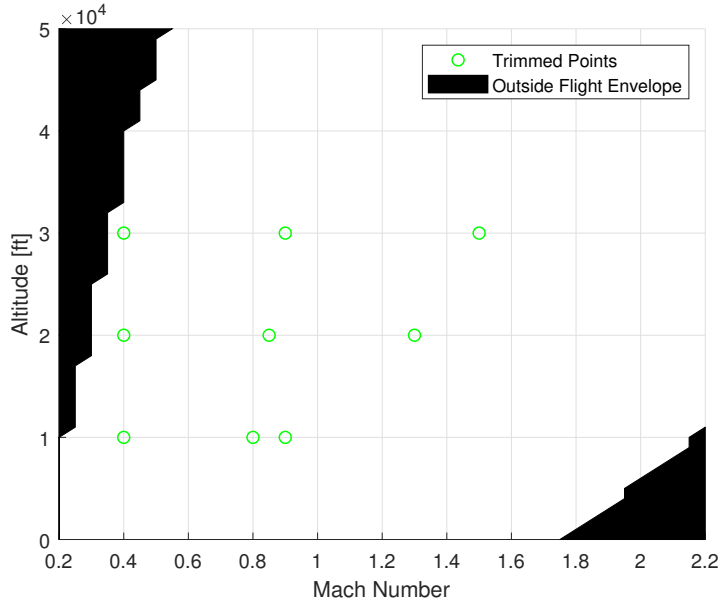
Figure 3.2: Defined flight envelope and trimmed conditions

3.2.2. Control effector properties

Each control effector has its own deflection limits, positive deflection definition, no-load rate limit and dynamics type. These are listed in table 3.3 below.

Table 3.3: Control effector properties and limits

Effector	Symbol	Deflection Limits (°)		Rate Limit (°/s)	Dynamics Type
Inboard LEFs	$\delta_{lif}, \delta_{rif}$	[0, 40]	LED (+)	40	$H_s(s)$
Outboard LEFs	$\delta_{lof}, \delta_{rof}$	[-40, 40]	LED (+)	40	$H_s(s)$
All-Moving Wingtips	$\delta_{lamt}, \delta_{ramt}$	[0, 60]	TED (+)	150	$H_f(s)$
Spoiler-Slot-Deflectors	$\delta_{lssd}, \delta_{rssd}$	[0, 60]		150	$H_f(s)$
Elevons	$\delta_{lele}, \delta_{rele}$	[-30, 30]	TED (+)	150	$H_f(s)$
Pitch Flaps	δ_{pf}	[-30, 30]	TED (+)	150	$H_f(s)$
Multi-Axis Thrust Vectoring	$\delta_{ptv}, \delta_{ytv}$	[0, 15]	TED, TER[1] (+)	15	$H_f(s)$

The slow actuator dynamics are represented by the following transfer function:

$$H_s(s) = \frac{18 \cdot 100}{(s+18)(s+100)} \tag{3.1}$$

The fast actuator dynamics are represented by the following transfer function.

$$H_f(s) = \frac{40 \cdot 100}{(s+40)(s+100)} \tag{3.2}$$

3.2.3. Model reference frames

All aerodynamic coefficient data tables are represented in the right-handed aerodynamic model frame $\mathbb{F}^m$. The origin and axis definitions are as follows:

— Origin: in the MRC as given in table 3.1, which is assumed to be the C.O.G.
— X_m: aft along the longitudinal axis of the aircraft
— Y_m: to the right
— Z_m: upwards to complete the system's right-handedness

---

[1]Trailing Edge Right

The aircraft model itself, however, uses the standard aircraft body frame axis system $\mathbb{F}^b$. That system is defined per the set of rules below and shall be used from this moment on throughout the thesis, unless states otherwise.

— Origin: in the MRC as given in table 3.1, which is assumed to be the C.O.G.
— X_b: forward along the longitudinal axis of the aircraft
— Y_b: to the right
— Z_b: downwards to complete the system's right-handedness

The correct axis transformation is applied to the aerodynamic model coefficients to obtain the correct aircraft model coefficient orientation. The transformed set of coefficients is subsequently used to propagate the aircraft state.

3.2.4. Coefficient set structure

Each set of coefficient tables, as previously stated, contains either two, three or four data tables describing the airframe contribution to the aerodynamic coefficients, in addition to the 15 tables accounted for by the 13 actuators. The general structure of each data set is given below. Keep in mind that these coefficients are given in the $\mathbb{F}^m$ frame. Coefficients apply over the entire set of DoFs, unless noted otherwise.

Table 3.4: General description of coefficient set elements

Coefficient	Description	Dependencies
C_{i_α}	Bare airframe coefficient, controls neutral, no sideslip	$f(\alpha, M)$
$C_{i_{\alpha\beta}}$	Bare airframe coefficient due to sideslip	$f(\alpha, \beta, M)$
$C_{i_{\delta_1}}$	Isolated contribution of left inboard LEF	$f(\alpha, \beta, \delta_1)$
$C_{i_{\delta_{11}}}$	Isolated contribution of right inboard LEF	$f(\alpha, \beta, \delta_{11})$
$C_{i_{\delta_5}}$	Isolated contribution of left AMT	$f(\alpha, \beta, \delta_5)$
$C_{i_{\delta_{15}}}$	Isolated contribution of right AMT	$f(\alpha, \beta, \delta_{15})$
$C_{i_{\delta_9}}$	Isolated contribution of left SSD	$f(\alpha, \beta, \delta_9)$
$C_{i_{\delta_{19}}}$	Isolated contribution of right SSD	$f(\alpha, \beta, \delta_{19})$
$C_{i_{\delta_1\delta_2}}$	Contribution of left outboard LEF influenced by left inboard LEF	$f(\alpha, \beta, \delta_1, \delta_2, M)$
$C_{i_{\delta_{11}\delta_{12}}}$	Contribution of right outboard LEF influenced by right inboard LEF	$f(\alpha, \beta, \delta_{11}, \delta_{12}, M)$
$C_{i_{\delta_2\delta_5}}$	Contribution of left AMT influenced by left outboard LEF	$f(\alpha, \delta_2, \delta_5)$
$C_{i_{\delta_{12}\delta_{15}}}$	Contribution of right AMT influenced by right outboard LEF	$f(\alpha, \delta_{12}, \delta_{15})$
$C_{i_{\delta_3\delta_5}}$	Contribution of left ELE influenced by left AMT	$f(\alpha, \delta_3, \delta_5)$
$C_{i_{\delta_{13}\delta_{15}}}$	Contribution of right ELE influenced by right AMT	$f(\alpha, \delta_{13}, \delta_{15})$
$C_{i_{\delta_3\delta_9}}$	Contribution of left ELE influenced by left SSD	$f(\alpha, \delta_3, \delta_9, M)$
$C_{i_{\delta_{13}\delta_{19}}}$	Contribution of right ELE influenced by right SSD	$f(\alpha, \delta_{13}, \delta_{19}, M)$
$C_{i_{\delta_4\delta_9\delta_{19}}}$	Contribution of PF influenced by SSDs	$f(\alpha, \delta_4, \delta_9, \delta_{19}, M)$
$C_{i_p}\frac{pb}{2V}$	Bare airframe coefficient due to roll rate ($i = l, n$)	$f(\alpha, M)$
$C_{i_q}\frac{qc}{2V}$	Bare airframe coefficient due to pitch rate ($i = Z, m$)	$f(\alpha, M)$
$C_{i_r}\frac{rb}{2V}$	Bare airframe coefficient due to yaw rate ($i = l, n$)	$f(\alpha, M)$

The aerodynamic body coefficients can be written in terms of the elements in table 3.4 by expanding the general case and applying the correct transformations. This yields the following results:

$$
\begin{aligned}
-C_{X_b} = C_{X_m} = &+ C_{X_\alpha} + C_{X_{\alpha\beta}} + C_{X_{\delta_1}} + C_{X_{\delta_{11}}} + C_{X_{\delta_5}} + C_{X_{\delta_{15}}} \\
&+ C_{X_{\delta_9}} + C_{X_{\delta_{19}}} + C_{X_{\delta_1\delta_2}} + C_{X_{\delta_{11}\delta_{12}}} + C_{X_{\delta_2\delta_5}} + C_{X_{\delta_{12}\delta_{15}}} \\
&+ C_{X_{\delta_3\delta_5}} + C_{X_{\delta_{13}\delta_{15}}} + C_{X_{\delta_3\delta_9}} + C_{X_{\delta_{13}\delta_{19}}} + C_{X_{\delta_4\delta_9\delta_{19}}}
\end{aligned}
\tag{3.3}
$$

$$
\begin{aligned}
C_{Y_b} = C_{Y_m} = &+ C_{Y_\alpha} + C_{Y_{\alpha\beta}} - C_{Y_{\delta_1}} + C_{Y_{\delta_{11}}} + C_{Y_{\delta_5}} - C_{Y_{\delta_{15}}} \\
&+ C_{Y_{\delta_9}} - C_{Y_{\delta_{19}}} - C_{Y_{\delta_1\delta_2}} + C_{Y_{\delta_{11}\delta_{12}}} + C_{Y_{\delta_2\delta_5}} - C_{Y_{\delta_{12}\delta_{15}}} \\
&+ C_{Y_{\delta_3\delta_5}} - C_{Y_{\delta_{13}\delta_{15}}} + C_{Y_{\delta_3\delta_9}} - C_{Y_{\delta_{13}\delta_{19}}} + C_{Y_{\delta_4\delta_9\delta_{19}}}
\end{aligned}
\tag{3.4}
$$

$$-C_{Z_b} = C_{Z_m} = + C_{Z_\alpha} + C_{Z_{\alpha\beta}} + C_{Z_{\delta_1}} + C_{Z_{\delta_{11}}} + C_{Z_{\delta_5}} + C_{Z_{\delta_{15}}}$$
$$+ C_{Z_{\delta_9}} + C_{Z_{\delta_{19}}} + C_{Z_{\delta_1\delta_2}} + C_{Z_{\delta_{11}\delta_{12}}} + C_{Z_{\delta_2\delta_5}} + C_{Z_{\delta_{12}\delta_{15}}}$$
$$+ C_{Z_{\delta_3\delta_5}} + C_{Z_{\delta_{13}\delta_{15}}} + C_{Z_{\delta_3\delta_9}} + C_{Z_{\delta_{13}\delta_{19}}} + C_{Z_{\delta_4\delta_9\delta_{19}}} + C_{Z_q}\frac{q\bar{c}}{2V} \tag{3.5}$$

$$C_{l_b} = C_{l_m} = + C_{l_\alpha} + C_{l_{\alpha\beta}} - C_{l_{\delta_1}} + C_{l_{\delta_{11}}} + C_{l_{\delta_5}} - C_{l_{\delta_{15}}}$$
$$+ C_{l_{\delta_9}} - C_{l_{\delta_{19}}} - C_{l_{\delta_1\delta_2}} + C_{l_{\delta_{11}\delta_{12}}} + C_{l_{\delta_2\delta_5}} - C_{l_{\delta_{12}\delta_{15}}}$$
$$+ C_{l_{\delta_3\delta_5}} - C_{l_{\delta_{13}\delta_{15}}} + C_{l_{\delta_3\delta_9}} - C_{l_{\delta_{13}\delta_{19}}} + C_{l_{\delta_4\delta_9\delta_{19}}} + C_{l_p}\frac{pb}{2V} + C_{l_r}\frac{rb}{2V} \tag{3.6}$$

$$C_{m_b} = C_{m_m} = + C_{m_\alpha} + C_{m_{\alpha\beta}} + C_{m_{\delta_1}} + C_{m_{\delta_{11}}} + C_{m_{\delta_5}} + C_{m_{\delta_{15}}}$$
$$+ C_{m_{\delta_9}} + C_{m_{\delta_{19}}} + C_{m_{\delta_1\delta_2}} + C_{m_{\delta_{11}\delta_{12}}} + C_{m_{\delta_2\delta_5}} + C_{m_{\delta_{12}\delta_{15}}}$$
$$+ C_{m_{\delta_3\delta_5}} + C_{m_{\delta_{13}\delta_{15}}} + C_{m_{\delta_3\delta_9}} + C_{m_{\delta_{13}\delta_{19}}} + C_{l_{\delta_4\delta_9\delta_{19}}} + C_{m_q}\frac{q\bar{c}}{2V} \tag{3.7}$$

$$C_{n_b} = C_{n_m} = + C_{n_\alpha} + C_{n_{\alpha\beta}} - C_{n_{\delta_1}} + C_{n_{\delta_{11}}} + C_{n_{\delta_5}} - C_{n_{\delta_{15}}}$$
$$+ C_{n_{\delta_9}} - C_{n_{\delta_{19}}} - C_{n_{\delta_1\delta_2}} + C_{n_{\delta_{11}\delta_{12}}} + C_{n_{\delta_2\delta_5}} - C_{n_{\delta_{12}\delta_{15}}}$$
$$+ C_{n_{\delta_3\delta_5}} - C_{n_{\delta_{13}\delta_{15}}} + C_{n_{\delta_3\delta_9}} - C_{n_{\delta_{13}\delta_{19}}} + C_{n_{\delta_4\delta_9\delta_{19}}} + C_{n_p}\frac{pb}{2V} + C_{n_r}\frac{rb}{2V} \tag{3.8}$$

From here on out, C_{i_b} shall be written as C_i for $i = X, Y, Z, l, m, n$ unless stated otherwise.

In order to be able to investigate aircraft behaviour over a larger AoA range, the base airframe coefficient tables with a range of $-5° \le \alpha \le 90°$ were mirrored in $\alpha = 0°$ by Matamoros and de Visser to obtain airframe coefficient data tables for $-90° \le \alpha \le +90°$. This approach was found to produce positive drag coefficients for low negative AoA ($-4° \le \alpha \le 0°$) in some instances. To counter this, the original data tables were used over their full range, with the data for $6° \le \alpha \le 90°$ being used to extend the data table range to $-90°$ with odd mirroring in $0°$ as before. The advantage is that the positive drag coefficients do not arise anymore with the trade-off being a jump in lift and drag coefficients between $-5°$ and $-6°$.

3.2.5. Thrust Vectoring System
The thrust vectoring system is instrumental in maintaining lateral-directional control authority at low speeds as well as improving maximum roll control (Dorsett et al., 1997). The limits placed on the vectoring system are the 15° omnidirectional deflection limit, the 150°/s rate limit and the actuator dynamics. Note that the thrust vectoring system only controls thrust *direction* and does not not control thrust *setting*, which is controlled by the Auto-Throttle (AT) system.

The TV system makes use of the pitch and a yaw deflection angles $\delta_{p_{tv}}$ and $\delta_{y_{tv}}$, respectively. These angles are controlled by the INCA algorithm in the same fashion as the other actuator deflections. Due to the fact that a simultaneous deflection of 15° would lead to a total deflection of $\sqrt{2} \cdot 15°$, an additional constraint is applied to prevent such a situation:

$$\sqrt{\delta_{p_{tv}}^2 + \delta_{y_{tv}}^2} \le \delta_{tv_{max}} \tag{3.9}$$

The Trust Vectoring system in Matamoros and de Visser (2018) was found to contain small inaccuracies for large deflections. Therefore, the TV equations for thrust-induced forces and moments were reformulated to ensure 100% accuracy. These can be found below in eqs. (3.10) to (3.14). Here, a positive δp_{tv} denotes a downward nozzle deflection and a positive δt_{tv} denotes a nozzle deflection to the right. Note that the forces and moments are defined in the $\mathbb{F}^b$ frame. The aforementioned TV constraints still apply. The visual representation of this system is shown in fig. 3.3.

$$T_X = T\cos(\delta_{p_{tv}})\cos(\delta_{y_{tv}}) \tag{3.10}$$

$$T_Y = -T\cos(\delta_{p_{tv}})\sin(\delta_{y_{tv}}) \tag{3.11}$$

$$T_Z = -T\sin(\delta_{p_{tv}}) \tag{3.12}$$

$$M_Y = rT_Z = -rT\sin(\delta_{p_{tv}}) \tag{3.13}$$

$$M_Z = -rT_Y = rT\cos(\delta_{p_{tv}})\sin(\delta_{y_{tv}}) \tag{3.14}$$

M_X is not shown as it is always zero. The Jacobian terms for these equations – whose usage is explained later in this chapter – then follow as

Table 3.5: Jacobian terms for thrust vectoring forces and moments

	$\partial\delta_{p_{tv}}$	$\partial\delta_{y_{tv}}$
∂T_X	$-T\sin(\delta_{p_{tv}})\cos(\delta_{y_{tv}})$	$-T\cos(\delta_{p_{tv}})\sin(\delta_{y_{tv}})$
∂T_Y	$-T\sin(\delta_{p_{tv}})\sin(\delta_{y_{tv}})$	$-T\cos(\delta_{p_{tv}})\cos(\delta_{y_{tv}})$
∂T_Z	$-T\cos(\delta_{p_{tv}})$	0
∂M_Y	$-rT\cos(\delta_{p_{tv}})$	0
∂M_z	$-rT\sin(\delta_{p_{tv}})\sin(\delta_{y_{tv}})$	$rT\cos(\delta_{p_{tv}})\cos(\delta_{y_{tv}})$
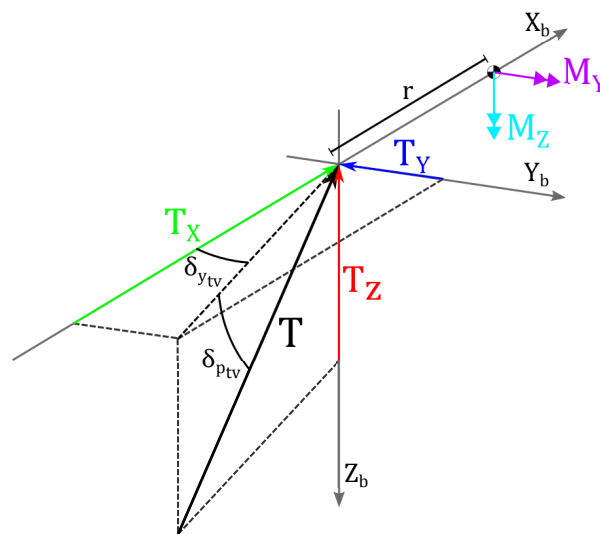
Figure 3.3: Schematic representation of the TV system

3.3. Nonlinear interdependent effector behaviour

The ICE effector suite is designed for high maneuverability and low RCS and as such employs novel control concepts. Two major drawbacks of the described control suite are control power nonlinearities and high levels of interdependence. Three examples of these phenomena are illustrated in figs. 3.4a to 3.4c. As such, conventional control allocation methods do not suffice; linear approximation would severely degrade model fidelity and therefore hamper correct control allocation.
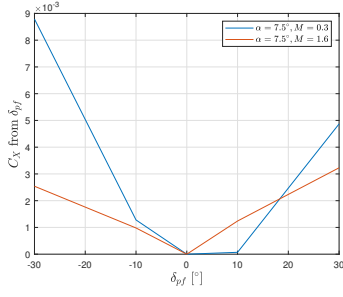
(a) Nonlinear behaviour of C_X for varying δ_{pf} for two different M
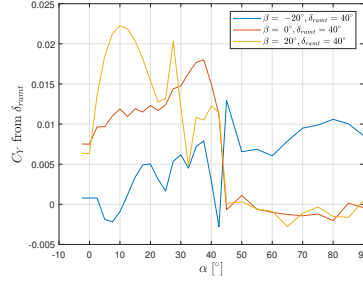
(b) Effect of α and β on C_Y generated by the right AMT
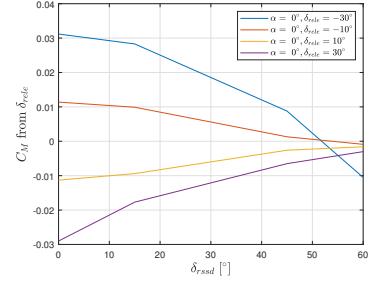
(c) Increasing δ_{rssd} degrades C_M generated by the right elevator

To this end, an Incremental Nonlinear Control Allocation method was developed for the ICE in Matamoros and de Visser (2018). The resultant inner loop design and accompanying algorithm have shown promising results as a solution to the Control Allocation (CA) issues discussed above.

$$
J(\alpha, \beta, M, \boldsymbol{\delta}) = \begin{bmatrix} \sum_{j=1}^{20} \frac{\partial C_{X_j}^s(\boldsymbol{x}, \boldsymbol{\delta})}{\partial \delta_1} & \sum_{j=1}^{20} \frac{\partial C_{i_j}^s(\boldsymbol{x}, \boldsymbol{\delta})}{\partial \delta_2} & \cdots & \sum_{j=1}^{20} \frac{\partial C_{X_j}^s(\boldsymbol{x}, \boldsymbol{\delta})}{\partial \delta_{13}} \\ \sum_{j=1}^{20} \frac{\partial C_{Y_j}^s(\boldsymbol{x}, \boldsymbol{\delta})}{\partial \delta_1} & \sum_{j=1}^{20} \frac{\partial C_{i_j}^s(\boldsymbol{x}, \boldsymbol{\delta})}{\partial \delta_2} & \cdots & \sum_{j=1}^{20} \frac{\partial C_{Y_j}^s(\boldsymbol{x}, \boldsymbol{\delta})}{\partial \delta_{13}} \\ \vdots & \vdots & \ddots & \vdots \\ \sum_{j=1}^{20} \frac{\partial C_{n_j}^s(\boldsymbol{x}, \boldsymbol{\delta})}{\partial \delta_1} & \sum_{j=1}^{20} \frac{\partial C_{n_j}^s(\boldsymbol{x}, \boldsymbol{\delta})}{\partial \delta_2} & \cdots & \sum_{j=1}^{20} \frac{\partial C_{n_j}^s(\boldsymbol{x}, \boldsymbol{\delta})}{\partial \delta_{13}} \end{bmatrix} \tag{3.15}
$$

The algorithm uses an incremental control approach centered around the Jacobian of a spline model based on the aerodynamic data tables, which was constructed using the method outlined in Tol et al. (2016). An example of such a matrix is shown in eq. (3.15) and a full Jacobian derivation explanation can be found in appendix A. For the thrust vectoring system, the Jacobian is the terms in table 3.5. Using an Active Set approach developed in Härkegård (2002), the INCA algorithm dynamically drives the actuators by means of incremental deflection commands. A detailed description of the algorithm can be found in section 4.1.

By taking an incremental approach and using the Jacobian to determine the best possible set of control increments for that particular time instance, the issues caused by nonlinearities, inter-dependency effects, actuator dynamics and aerodynamic uncertainties are mitigated. A Quadratic Programming (QP) solver has shown to produce the best results in terms of aircraft controllability and control demand satisfaction.

3.4. DFC opportunities

The INCA algorithm has shown satisfactory results, but the system has only been tested for FCS based on rotational control. For conventional aircraft, this is where the story would end. The ICE effector suite, however, houses more opportunities due to the large number of control effectors. Once a challenge, the underdetermined control allocation problem now becomes an area of strength.

For conventional aircraft, there are – oversimplifying slightly – three control surfaces available: elevators, ailerons and rudder. Therefore, such a control effector suite can only *directly* control three Degrees of Freedom: the rotational DoFs. Of course, the thrust setting directly controls the axial force as well. It is possible to re-design control architecture such that the effectors control the other two translational DoFs, but this would mean sacrificing control authority over one or more rotational DoFs. One can only imagine what the result would be if the rudder were to be employed as a means of directly controlling side force in lieu of controlling yawing moment; the effects would be disastrous. Of course, side force can still be controlled, but this happens *indirectly* by means of either sideslip or bank angle adjustment. The same goes for normal force along the lines of pitch angle control.

The ICE aircraft, however, should theoretically be able to *directly* control *all six* Degrees of Freedom at once. That theoretical notion now becomes a distinct possibility due to the availability of Matamoros and de Visser's INCA solution to the CA problem. This could open the door to a completely new type of FCS design, with all sorts of associated benefits ánd drawbacks. The goal of this thesis is to test this hypothesis and further investigate DFC usage for practical use cases.

$$4$$

Direct Force Control

This chapter treats the development of the set of DFC control laws and loops. First, the extension requirements for the current model as described by Matamoros and de Visser are given and discussed in section 4.1. Next, the isolated DFC capacities are studied in section 4.2. These results are subsequently used in section 4.3 to construct the necessary control laws and loops. Finally, an FCS capable of simultaneously controlling rotation and translation is presented in section 4.4.

4.1. INCA Algorithm extension

The goal of the CA algorithm is to find the set of actuator deflections that ensure satisfaction of the incremental moment command while minimizing actuator deflection. In other words, the error between commanded and realized moment increments as well as the actuator deflections have to be minimized. Matamoros and de Visser have posed this minimization problem as follows:

$$\min_{\mathbf{u}} \mathscr{J} = W_{\mathbf{d}} ||\mathrm{J}_{\mathrm{R}} \mathbf{u} - \Delta \boldsymbol{\tau}_{\mathrm{R}c}||_2 + \epsilon W_{\mathbf{u}} ||\mathbf{u} - \mathbf{u}_p||_2 \qquad (4.1)$$

$$\underline{\mathbf{u}} \leq \mathbf{u} \leq \overline{\mathbf{u}}$$

Here, $W_{\mathbf{d}}$ is a diagonal command weighting matrix, J_{R} is the rotational Jacobian matrix, $\mathbf{u}$ is the set of commanded actuator deflections, $\Delta \boldsymbol{\tau}_{Rc}$ the set of commanded moment increments, $W_{\mathbf{u}}$ a diagonal deflection weighing matrix , $\mathbf{u}_p$ is the set of preferred deflections and $\underline{\mathbf{u}}$, $\overline{\mathbf{u}}$ are the minimum and maximum actuator deflections, respectively . Equation (4.1) can be rewritten into a form suitable for implementation in the Active Set algorithm from Härkegård (2002).

$$\min_{\mathbf{u}} \left\| \begin{bmatrix} W_{\mathbf{d}} \mathrm{J}_{\mathrm{R}} \\ \epsilon W_{\mathbf{u}} \end{bmatrix} \mathbf{u} - \begin{bmatrix} W_{\mathbf{d}} \Delta \boldsymbol{\tau}_{\mathrm{R}c} \\ \epsilon W_{\mathbf{u}} \mathbf{u}_p \end{bmatrix} \right\|_2 \qquad (4.2a)$$

$$\mathrm{J}_{\mathrm{R}} \mathbf{u} = \Delta \boldsymbol{\tau}_{Rc} \qquad (4.2b)$$

$$C\mathbf{u} \geq U \qquad (4.2c)$$

By setting $C = [I - I]^T$ and $U = [\underline{\mathbf{u}} - \overline{\mathbf{u}}]^T$, the constraint of eq. (4.1) is satisfied. The usage of eqs. (4.2a) to (4.2c) in the Active Set method is shown below in Algorithm 1. This example of pseudocode illustrates the Active Set-Quadratic Programming solver method for Incremental Control Allocation pioneered in Matamoros and de Visser (2018).

In order to be able to test the DFC capacities of the ICE aircraft, the ICE model has to be extended with a number of DFC control loops. This means that the 3DoF algorithm code has to be adapted in order to take 6DoF parameters and produce the same result: the ideal incremental control deflections which produce the desired control forces and moments with minimal deflection.

Adaption of the algorithm is quite straightforward. As the control effector suite itself is not subject to change, only the primary objective of minimizing $W_{\mathbf{d}} ||\mathrm{J}_{\mathrm{R}} \mathbf{u} - \Delta \boldsymbol{\tau}_{\mathrm{R}c}||_2$ is appended. Working back to front:

Algorithm 1: Incremental Control algorithm based on Active Set Quadratic Programming

---

Let $\mathbf{u}_0$ be a feasible starting point. A point is feasible if it satisfies the constraints in eqs. (4.2b) and (4.2c). Let the working set $\mathcal{W}$ contain (a subset of) the active inequality constraints at $\mathbf{u}_0$.

for $k = 0, 1, 2, ... N - 1$ **do**

    Given $\mathbf{u}^k$, find the optimal perturbation $\mathbf{p}$, considering the constraints in the working set as equality constraints and disregarding the remaining inequality constraints. Solve

$$\min_{\mathbf{u}} \left\| \begin{bmatrix} W_{\mathbf{d}} J_{\mathrm{R}} \\ \epsilon W_{\mathbf{u}} \end{bmatrix} (\mathbf{u}^k + \mathbf{p}) - \begin{bmatrix} W_{\mathbf{d}} \Delta \boldsymbol{\tau}_{\mathrm{R}c} \\ \epsilon W_{\mathbf{u}} \mathbf{u}_p \end{bmatrix} \right\|$$

$$G\mathbf{p} = 0 \tag{4.3}$$

$$\mathbf{p}_i = 0, \ i \in \mathcal{W}$$

    if $\mathbf{u}^k + \mathbf{p}$ is feasible **then**

        Set $\mathbf{u}^{k+1} = \mathbf{u}^k + \mathbf{p}$ and compute the Lagrange multipliers, $\binom{\mu}{\lambda}$, where μ is associated with eq. (4.2b) and λ with the active constraints in eq. (4.2c).

        if all $\lambda \geq 0$ **then**

            $\mathbf{u}^{k+1}$ is the optimal solution to eq. (4.2a)

        else

            Remove the constraint associated with the most negative λ from the working set.

        end

    else

        Determine the maximum step length α such that $\mathbf{u}^{k+1} = u^k + \alpha \mathbf{p}$ is feasible. Add the primary bounding constraint to the working set.

    end

end

$\Delta \boldsymbol{\tau}_{\mathrm{R}c}$: The 3x1 pseudo-control input vector $\Delta \boldsymbol{\tau}_{\mathrm{R}c}$ is appended with a set of three force increment commands $\Delta \boldsymbol{\tau}_{\mathrm{T}c}$ for the Translational DoFs and therefore becomes the 6x1 input vector $\Delta \boldsymbol{\tau}_c$ containing the commanded moment and force increments, respectively. Note that this symbol therefore is *not* equal to the $\Delta \boldsymbol{\tau}_c$ used in Matamoros and de Visser (2018).

J_{R}: The 3x13 rotational Jacobian matrix J_{R} is row-appended with another 3x13 Jacobian matrix J_{T} for the Translational DoFs. It therefore becomes J_{F}, a 6x13 Jacobian matrix containing the partial derivatives of all control effectors w.r.t. all DoFs.

$W_{\mathbf{d}}$: Lastly, the diagonal 3x3 command weighting matrix $W_{\mathbf{d}}$ is extended to a diagonal 6x6 $W_{\mathbf{d}}$ matrix containing weights corresponding to the commanded increments of each of the 6DoF. This matrix will be used extensively in the upcoming sections to isolate and identify translational force control properties and limits.

4.2. Force Generation Capacities

This section treats the isolated DFC capacities of each body axis. Isolated in this context means that the focus lies on a single body axis. It also serves as an introduction into the working principle of direct force control used in this thesis. First the base of the FSC is given, after which the capacities of axial force generation and combined lateral & vertical force generation are treated.

4.2.1. Translational Flight Control System base

In order to test the DFC capacities of the ICE aircraft the full aircraft simulation model has to be extended with a Translational FCS loop. This loop enables commanding translational accelerations and observing the system responses to these commands. The set-up is shown in fig. 4.1 below.

Note that this schematic only depicts elements relevant to the current section and therefore does not show the full architecture. For example, the other eight algorithm inputs are not shown for clarity's sake. Also note that the new notation conventions are readily adopted. The shown control loop architecture holds until noted otherwise. In addition, the model block only contains the aerodynamic tables and coefficient handling
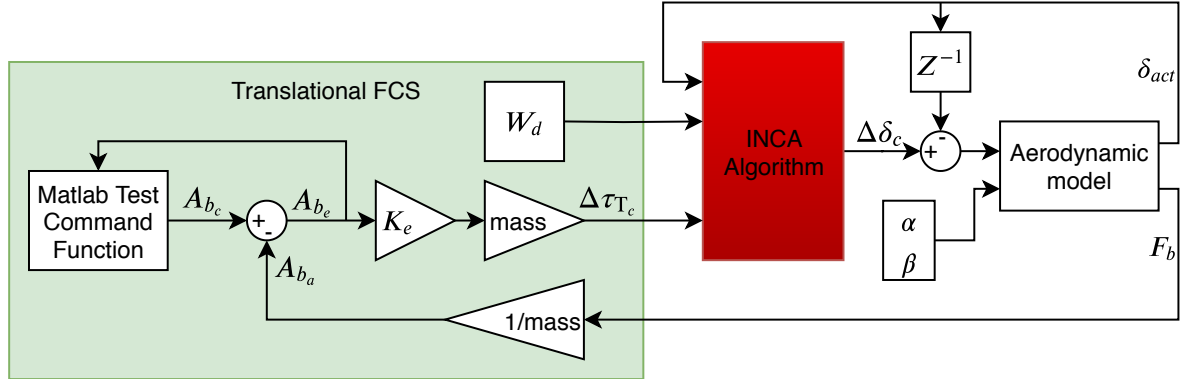
Figure 4.1: Initial Translational FCS loop

blocks. Therefore, the aircraft states are not propagated by means of the 6DoF Euler block mentioned in section 3.2.1.

Focusing on a single Degree of Freedom is achieved by manipulating the command weights in $W_\mathbf{d}$. For each section in this chapter, the weights in $W_\mathbf{d}$ are adapted to enable focus on the subject of interest. To this end, $W_\mathbf{d}$ becomes a 6x6 zero matrix with elements a_{nn} attaining a value of 1. Here, n is the order number of the involved Degree of Freedom, with the order being as follows:

n	1	2	3	4	5	6
DoF	roll	pitch	yaw	surge	sway	heave

The usage of weights will be discussed before a set of results is presented.

4.2.2. Axial forces

The forces that can be generated in X-direction are assumed to be purely negative, i.e. it is assumed that generation of forward forces is not possible. This assumption stems from the logical fact that there is no actuator in the actuator suite able to generate negative drag. There is the possibility of positive axial forces as a result of the effect of α on resultant force projection. However, a search through the aerodynamic data tables confirms the validity of the aforementioned assumption: the vast majority of the axial terms of the control effectors is positive, corresponding to negative axial body forces. Using the set-up shown in fig. 4.1, the maximum suite-generated axial force coefficients could be determined. These were calculated by transforming the recorded maximum acceleration using eq. (4.4).

$$C_{X_k} = \frac{m\, A_{X_k}}{0.5\, \rho\, V_{TAS}^2\, S_{ref}} \tag{4.4}$$

Two cases have been tested for various trim points, as can be seen in table 4.1. For C_{Xcon}, $a_{nn} = 1$ for $n = [4,5,6]$ and $A_{Y_c} = 0$, $A_{Z_c} = 0$ to explore controlled axial force generation. For C_{Xiso}, only $a_{44} = 1$ to investigate isolated force generation capacity. For each case, the maximum acceleration is the acceleration for which the acceleration error of all involved Degrees of Freedom is ≤ 0.5 ft/s^2. In other words, $A_{b_e} \leq 0.5$.

The data in table 4.1 do not seem to indicate a particular combination of trim point and mass configuration for which either controlled or isolated force generation is markedly better. Figure 4.2a shows the average of all coefficients for both cases for each trim point. In order to visualize the effect of secondary thrust vectoring effects, both average sets are plotted against dynamic pressure in fig. 4.2b. As dynamic pressure increases, the average difference between controlled and isolated C_X seems to increase. When computing the relative increase, however, there does not seem to be any discernible trend.

Table 4.1: Different values for axial effector suite force generation coefficient

Trim Point	Lightweight		Nominal		Heavyweight	
	C_{Xcon}	C_{Xiso}	C_{Xcon}	C_{Xiso}	C_{Xcon}	C_{Xiso}
1	-0.1293	-0.1662	-0.1319	-0.1474	-0.0703	-0.0615
2	-0.1164	-0.1210			-0.1158	-0.1202
3			-0.1159	-0.1204	-0.1157	-0.1226
4	-0.0641	-0.0641	-0.1385	-0.1385	-0.1304	-0.1438
5	-0.1161	-0.1222	-0.1078	-0.1284	-0.0930	-0.1279
6	-0.0779	-0.0831			-0.1075	-0.1359
7	-0.1264	-0.1404	-0.0885	-0.0085	-0.0801	-0.0801
8	-0.1178	-0.1206	-0.1202	-0.1206	-0.1201	-0.1201
9	-0.1028	-0.1358	-0.0944	-0.1221	-0.1040	-0.1824
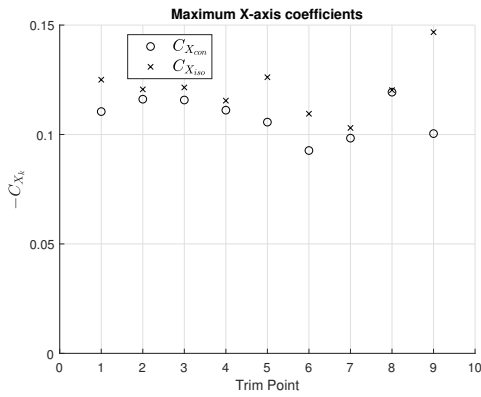
(a) Average axial coefficients per trim point
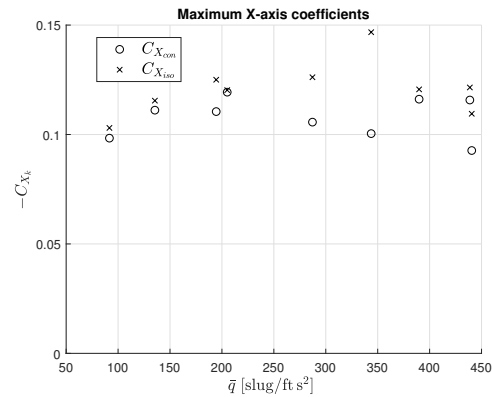
(b) Axial coefficients against dynamic pressure

4.2.3. Combined lateral and vertical forces

The usage of different weight combinations influences the effector suite's force generation capacities, sometimes up to 50%. Therefore, lateral and vertical force generation are evaluated in unison to better encompass simultaneous lateral and vertical control. For this section, $a_{nn} = 1$ for $n = [5, 6]$. Axial force generation is not actively controlled. Again, the same logic as in section 4.2.2 is applied to determine achievable accelerations. The results for the trimmed lightweight condition at FL200 with $V_{TAS} = 880$ ft/s are shown in fig. 4.3a. Keep in mind that downward accelerations are positive.

The red boundary shows all acceleration combinations that can be achieved by the system regardless of collateral axial force. The black boundary shows those combinations for which excess thrust levels are high enough to compensate for the increase in negative axial force w.r.t. the trimmed condition. Therefore, accelerations that are within the red but outside the black boundary generate such a large amount of drag that a decrease in axial velocity cannot be avoided.

The effects of differing angles of attack on acceleration envelope have been studied as well and are shown in figs. 4.3b and 4.3c. As can be expected, the maximum positive vertical force that can be generated decreases with increasing angle of attack. At $\alpha = \alpha_{trim} + 5°$ the effector suite completely loses the ability to generate positive forces along the Z-axis. Likewise, a decrease in angle of attack deteriorates the maximum negative acceleration. Here, the limit is $\alpha = \alpha_{trim} - 9°$. The vertical acceleration limits over the entire range of AoA is shown in fig. 4.4
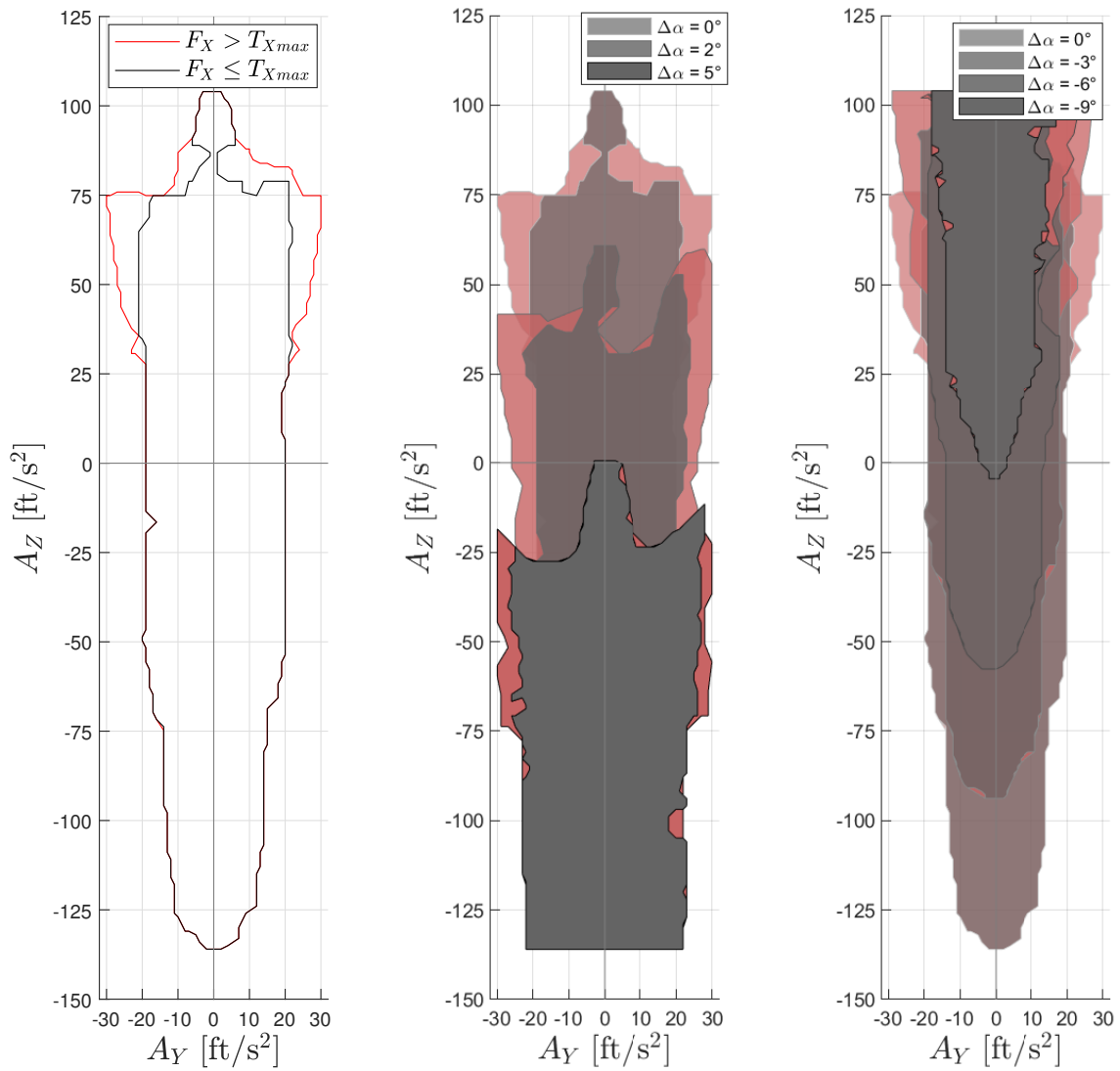
(a) Counterable and uncounterable acceleration limits for trim point at FL200, V_{TAS} = 880, lightweight

(b) Effect of increasing α on maximum positive acceleration at FL200, V_{TAS} = 880, lw

(c) Effect of decreasing α on maximum negative acceleration at FL200, V_{TAS} = 880, lw
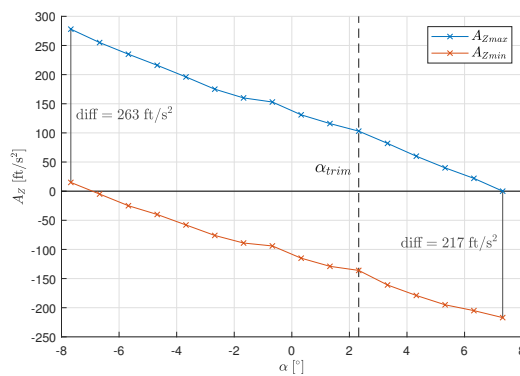
Figure 4.4: Upper and lower A_Z limits at FL200, V_{TAS} = 880, lw

Clearly, the ICE aircraft is much more capable of generating vertical forces than lateral forces. This comes as no surprise, especially when keeping in mind the challenges in lateral-directional control already discussed

in Bowlus et al. (1997). In addition, most effectors are very adept at deflecting airflow upwards or downwards; in fact, all effectors are able to do such a thing. This does not hold true for lateral airflow deflection. The pitch flaps are completely unable to do such a thing, whereas the elevons and SSDs are somewhat capable of generating side force, but it is not their primary function. There are other effectors, like the AMTs, which do provide very good yaw control. However, as this partly depends on drag generation, good yaw control does not necessarily relate to good lateral force generation.

The effect of a changing angle of sideslip on lateral force generation, shown in fig. 4.5, is much smaller than the effect seen in figs. 4.3b and 4.3c. This is mainly due to the fact that C_{Y_β} is not nearly as large as C_{Z_α}. In addition, only 8 of the 15 effector suite coefficients are dependent on β which decreases the impact a change in sideslip has on force generation. These factors ensure positive lateral force generation is possible up to $\beta = 30°$, which is the largest angle of sideslip available in the dataset from Niestroy et al. (2017) and therefore the largest angle tested.
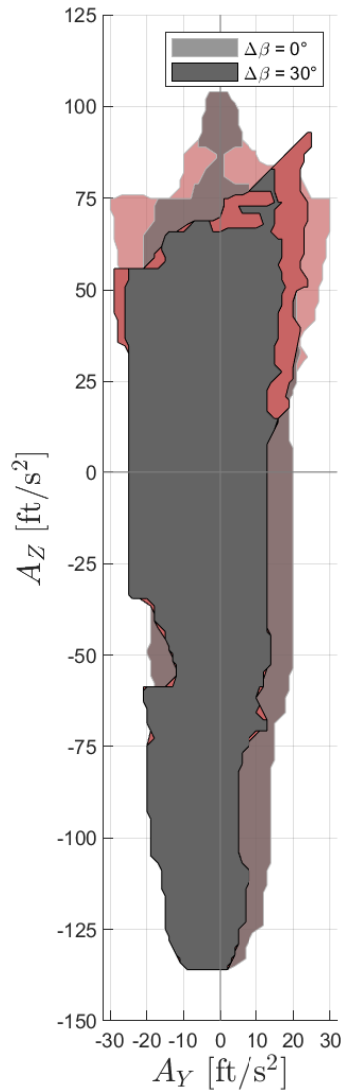
Figure 4.5: Effect of sideslip on acceleration envelope at FL200, $V_{TAS} = 880$, lw

Table 4.2: Maximum coordinated lateral accelerations at $A_Z = 0$ for increasing angle of sideslip in ft/s^2

$\Delta\beta$	0°	5°	10°	20°	30°
$A_{Y\,max}$	20	14	11	12	13
$A_{Y\,min}$	-19	-21	-30	-24	-25

4.3. Translational Velocity loop extension

The results from the previous sections have demonstrated that lateral force control is very much possible. Therefore, the addition of a velocity control loop warrants investigation. To this end, the acceleration control loop in fig. 4.1 is both changed and appended. The aerodynamic model is replaced by the full ICE model; the 6DoF Euler state propagation block is now used to generate the full aircraft state.

Figure 4.6: Translational Velocity Control Loops

In addition, a hedge block is placed in the vertical acceleration loop. As the data in figs. 4.3b, 4.3c and 4.4 have shown, AoA has a profound impact on vertical force generation. It has been observed that a sustained large nonzero acceleration error in one of the channels has a large negative effect on the force control of the other channels. In other words, pushing the vertical acceleration beyond the known limits as a function angle of attack of heavily deteriorates lateral and axial force control. To counter this, the following hedge parameter is implemented:

$$K_{A_Z} = \begin{cases} 1 & \text{sgn}(A_{Z_c}) \neq \text{sgn}(\alpha) \\ f_K & \text{sgn}(A_{Z_c}) = \text{sgn}(\alpha) \end{cases} \tag{4.5}$$

$$f_K(\alpha, b, f, c) = \max(0, \min(1, \frac{-2|\alpha - c|}{b(1-f)} + \frac{f}{1-f} + 1)) \tag{4.6}$$

Here, b is the total bandwidth for which A_z is nonzero, f is the fraction of the bandwidth for which A_z is unrestricted and c is the center of the bandwidth. Using $b = 10$, $f = 0.8$ and $c = 0$, the result is a function which is 1 for $|\alpha| \leq 0.5bf$, then linearly decreases from 1 to 0 over the next $b(1-f)/2$ on either side and is zero for $|\alpha| > 0.5b$. This function ensures that infeasible vertical acceleration commands do not cause saturation of the INCA algorithm and control along other axes is maintained. This procedure is not required for lateral control because β does not cause such saturation (also see fig. 4.5 and table 4.2).

Since state propagation is enabled for the current set-up, prolonged vertical acceleration commands will at some point cause K_{A_Z} to decrease to zero. Conversely, there is a limit to the vertical body velocities the ICE aircraft can attain. Assuming $\beta = 0°$, the vertical velocity limits with the aforementioned parameters for eq. (4.6) are -41.1 ft/s and +112.3 ft/s deviations from the trimmed condition for FL200, $V_{TAS} = 880$ ft/s and the lightweight mass configuration, for example. Other values will apply for other trim points.

The acceleration subsystem is completed by addition of a saturation block, restricting maximum commanded acceleration to purely negative values for the X-axis and ± 20ft/s^2 for the Y- and Z-axis. These values were chosen because this creates a square acceleration envelope for which all acceleration commands can be met, avoiding channel saturation and the associated cross-coupled performance deterioration.

The velocity subsystem is a straightforward feedback loop with a PID system. A constant vertical velocity V_0 is added to the commanded velocity to ensure the aircraft returns to the trimmed condition for zero commands. This measure prevents the angle of attack from returning to zero, which would result in a nonzero flight path angle γ.

4.3.1. Lateral and Vertical velocity control

The modifications treated in the previous section enable evaluation of translational velocity control properties. Commanded velocity have been limited to ± 20 ft/s, as such speeds are more than adequate for the cardinal use case, air-to-air refueling. The result is shown in fig. 4.7.

Figure 4.7: Body velocity control using DFC

In line with previous observations, lateral control is slower than vertical control. The main reason is that the achievable accelerations are larger for vertical control. Differences in actuator dynamics type do not seem to play a part; the SSDs, AMTs and MTV – all with fast dynamics – are the largest contributors to lateral force generation. The PID parameters are as shown below in eq. (4.7), with each column representing the parameters for a DoF.

$$\begin{bmatrix} 1 & 7 & 8 \\ 0 & 0 & 0 \\ 0 & 7 & 5 \end{bmatrix} \tag{4.7}$$

Up to this point, only a_{nn} with $n = [5,6]$ were set to 1 in $W_{\mathbf{d}}$. As can be expected, also setting $a_{44} = 1$ ensures that airspeed RMS is much lower than the situation in which axial force control by means of actuators is not applied. What is very surprising is that this comes at very little cost in terms of translational velocity control capacity. Table 4.3 shows relevant parameters for the exact same velocity command sequence. Rise time corresponds to the time needed to realize a velocity error of less than 0.5 ft/s. Using axial control totally prevents airspeed overshoot as well as decreasing maximum airspeed error. Dips in airspeed are of a lower magnitude and airspeed also recovers much faster to the set level. The axial control seems to minimize drag, which is supported by the fact that thrust usage over time is 43% lower.

Table 4.3: Error and rise time for different $W_{\mathbf{d}}$ settings

Setting	RMS V_{TAS}	RMS V_Y	RMS V_Z	Avg rise time V_Y	Avg rise time V_Z
$a_{44} = 0$	9.27	8.01	4.71	2.40	1.51
$a_{44} = 1$	3.47	8.71	4.47	2.74	1.52

4.4. Merged Rotational and Translational Control

The systems and results presented in sections 4.2 and 4.3 show that DFC is very much possible and implementation of a velocity control system yields favorable results in terms of translational velocity control. In order for this control philosophy to be feasible in real-life, however, all six Degrees of Freedom have to be controlled simultaneously. Therefore, the system discussed in section 4.3 is merged with the existing rotational control system from Matamoros and de Visser (2018) to form a full-fledged FCS. This system is depicted in fig. 4.8.

The primary goal of the depicted FCS is to enable translational control while keeping the attitude angles of the aircraft at set values. Therefore, the rotational control system requires inputs from an outer-loop system.
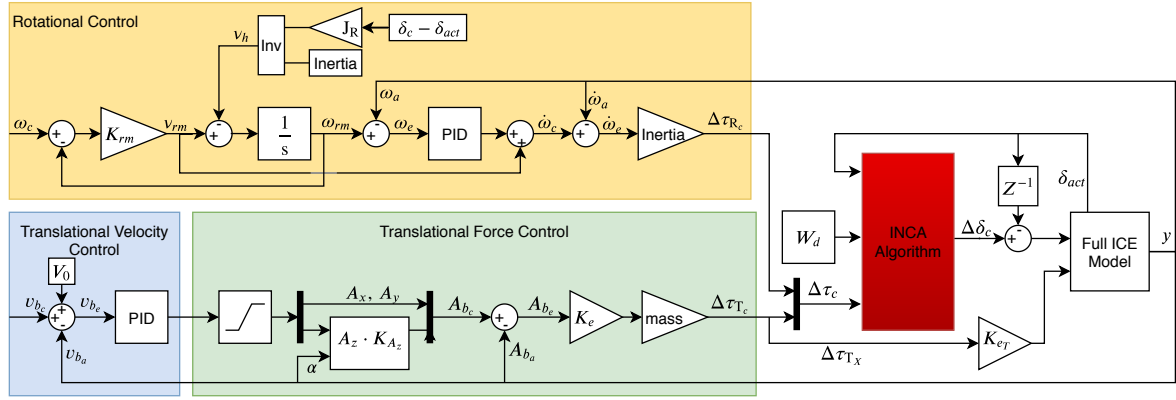
Figure 4.8: Full 6DoF inner loop control schematics

The control laws are as shown below.

$$
\begin{bmatrix} \dot{\varphi} \\ \dot{\theta} \\ \dot{\psi} \end{bmatrix} = K_P \begin{bmatrix} \varphi_c - \varphi_a \\ \theta_c - \theta_a \\ \mathrm{w}2\pi(\psi_c - \psi_a) \end{bmatrix} + K_I \int \begin{bmatrix} \varphi_c - \varphi_a \\ \theta_c - \theta_a \\ \mathrm{w}2\pi(\psi_c - \psi_a) \end{bmatrix} + K_D \frac{d}{dt} \begin{bmatrix} \varphi_c - \varphi_a \\ \theta_c - \theta_a \\ \mathrm{w}2\pi(\psi_c - \psi_a) \end{bmatrix} \text{ with } \tag{4.8}
$$

$$
\mathrm{w}2\pi(\theta) = \theta - 2\pi \cdot \mathrm{round}(\theta/2\pi) \text{ and } K = \begin{bmatrix} 2 & 0.1 & 0.5 \\ 5 & 0.1 & 5 \\ 2 & 0.1 & 0.1 \end{bmatrix}
$$

$$
\omega_c = \begin{bmatrix} p \\ q \\ r \end{bmatrix} = \begin{bmatrix} 1 & \sin\varphi\tan\theta & \cos\varphi\tan\theta \\ 0 & \cos\varphi & \sin\varphi \\ 0 & \sin\varphi/\cos\theta & \cos\varphi/\cos\theta \end{bmatrix}^{-1} \begin{bmatrix} \dot{\varphi} \\ \dot{\theta} \\ \dot{\psi} \end{bmatrix} = \begin{bmatrix} 1 & 0 & -\sin\theta \\ 0 & \cos\varphi & \sin\varphi\cos\theta \\ 0 & -\sin\varphi & \cos\varphi\cos\theta \end{bmatrix} \begin{bmatrix} \dot{\varphi} \\ \dot{\theta} \\ \dot{\psi} \end{bmatrix} \tag{4.9}
$$

By using $\varphi_c = 0$, $\theta_c = \theta_{trim}$ and $\psi_c = 0$, the attitude is fixed to the trimmed case and straight, steady, level flight is ensured for $v_{b_c} = 0$. In essence, rotation is countered as much as possible and the actuator suite should only generate net lateral and vertical forces – and the associated axial forces. The diagonal of $W_{\mathbf{d}}$ is set to $[1, 2, 1, 0.5, 1, 1]$. $K_e = [1, 2.2]$. Preliminary results are shown in fig. 4.9.

As expected, control authority over body velocities deteriorates due to the addition of three rotationals DoFs. Overall translational control is maintained, however, and rotational control is excellent. Most notably, rise time for vertical control decreases the most and now is about the same as lateral control rise time. When performing translational-isolated control tests, vertical response speed was much higher (see fig. 4.7).

The final step in designing a basic translational control system is adding an outer loop for position control. The translational counterpart to the attitude states is the XYZ position. Unlike the attitude, however, the position is constantly changing; the airspeed, and therefore the ground speed[1], is always nonzero, after all. Depending on the desired course $\mathcal{X}$ and the desired flight path angle γ, either one, two or all three elements that constitute position have nonzero derivatives. If $\mathcal{X} = \begin{bmatrix} 0 & \pi & 2\pi & 3\pi \end{bmatrix}/2$ or $\gamma = \begin{bmatrix} -\pi & 0 & \pi \end{bmatrix}/2$ then one derivative is zero. If both conditions are satisfied, two derivatives are zero.

The angles $\mathcal{X}$ and γ depend on the frame in which they are defined, however. This also holds for the initial position of the aircraft. Therefore, it is important to clearly define the relative position and orientation of the frame of reference in which X, Y, Z, $\mathcal{X}$ and γ are calculated. Possible options are an earth reference frame fixed at a specific point, a frame based on runway angle and inner marker position or a frame based on another aircraft's position and orientation. The first option will be expanded further in this section, whereas the latter cases are treated in chapter 5.

For the basic design of the translational position control outer loops, a simple test situation suffices. In this case, the position reference frame will be an position-fixed earth reference frame. Flat earth assumptions

---

[1]Disregarding the case for which the velocity of the air around the aircraft is exactly equal and opposite to the airspeed
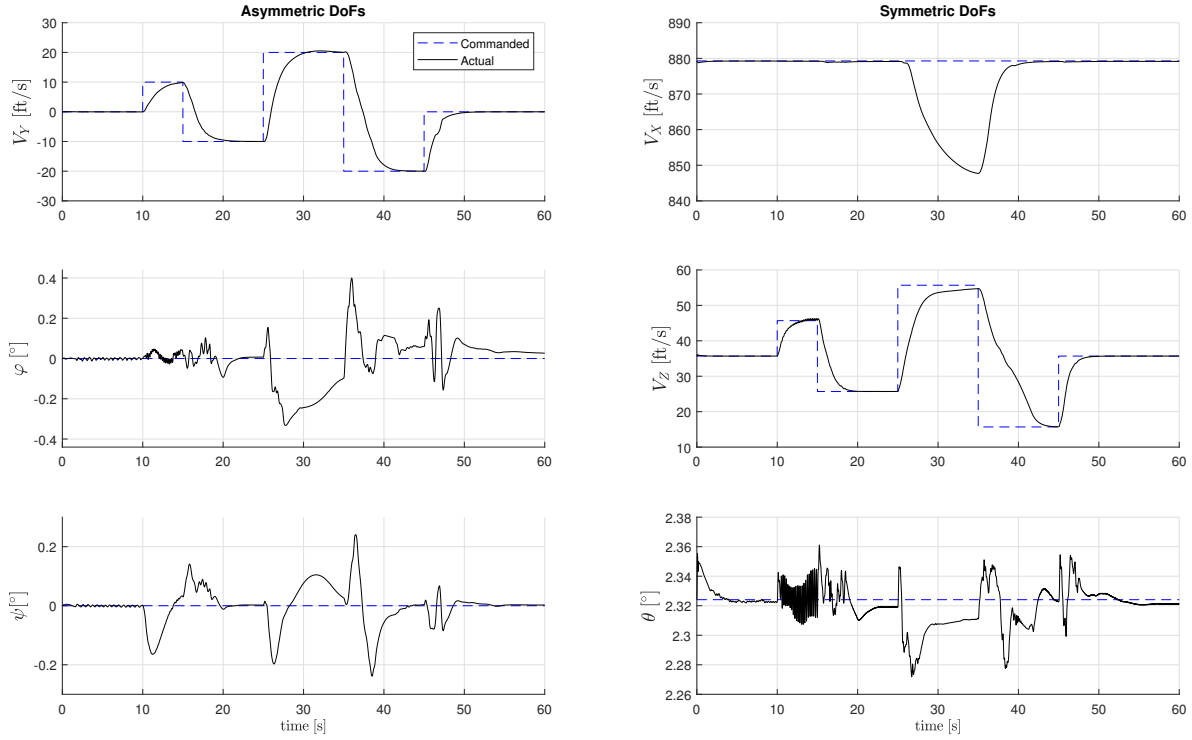
Figure 4.9: Simultaneous rotational and translational control

apply. Due to the fact that the simulation model is in essence an infinite plane with a center, the origin of the reference frame will be said center. The ICE aircraft starting position and orientation w.r.t. this center can be varied as needed.

The most straightforward case is a starting position at a trimmed altitude above the center with trimmed attitude and zero heading angle. In short, the aircraft follows a line parallel to X-axis of the reference frame on a plane with a specified altitude, not unlike following a 0° FROM VOR radial. The reference point in this case is a point on said line with the exact same X-coordinate as the aircraft. The reference point moves as the aircraft progresses and the X-position error therefore is always zero; this error is not of interest for translational position control at this point. Of course nonzero headings can be set as well, but the situation is essentially the same. The translational control laws are as follows:

$$v_{E_c} = K_P \begin{bmatrix} X_c - X_a \\ Y_c - Y_a \\ Z_c - Z_a \end{bmatrix} + K_I \int \begin{bmatrix} X_c - X_a \\ Y_c - Y_a \\ Z_c - Z_a \end{bmatrix} + K_D \frac{d}{dt} \begin{bmatrix} X_c - X_a \\ Y_c - Y_a \\ Z_c - Z_a \end{bmatrix} \text{ with } K = \begin{bmatrix} 1 & 0 & 1 \\ 2.5 & 0 & 2 \\ 3 & 0 & 1.5 \end{bmatrix} \quad (4.10)$$

v_{E_c} is the earth-centered velocity command and is limited to ± 15 ft/s for all elements. By using the angles of the body frame w.r.t. the position frame φ, θ and χ, it is possible to transform the earth frame velocity command into a body velocity command by the well-known 3-2-1 transformation.

$$v_{b_c} = \begin{bmatrix} 1 & 0 & 0 \\ 0 & \cos\varphi & \sin\varphi \\ 0 & -\sin\varphi & \cos\varphi \end{bmatrix} \begin{bmatrix} \cos\theta & 0 & -\sin\theta \\ 0 & 1 & 0 \\ \sin\theta & 0 & \cos\theta \end{bmatrix} \begin{bmatrix} \cos\psi & \sin\psi & 0 \\ -\sin\psi & \cos\psi & 0 \\ 0 & 0 & 1 \end{bmatrix} \begin{bmatrix} v_X \\ v_Y \\ v_Z \end{bmatrix}_E \quad (4.11)$$

The obtained body velocity command v_{b_c} is fed into the previously outlined systems to complete the loop. The result is a system depicted in fig. 4.10. A preliminary test is shown in fig. 4.11. As with the 6DoF velocity test, the attitude is kept at the trimmed condition by means of rotational control. The X-position is a reference signal of $V_{des} \cdot t$, Y position is as described in the preceding paragraphs and Z position is altitude. To facilitate plotting, the ICE X-position w.r.t. the reference position is given instead of the actual ramp input and actual position. Note that control of X-position is of a dual nature: both the axial force generated by the effector

suite deflections and the thrust produced by the engine combine to provide axial force control.
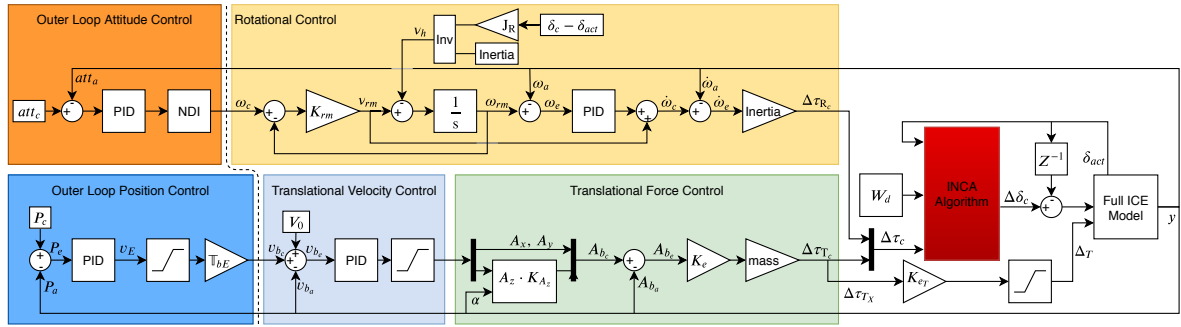
Figure 4.10: Full FCS with outer loop attitude and position control systems
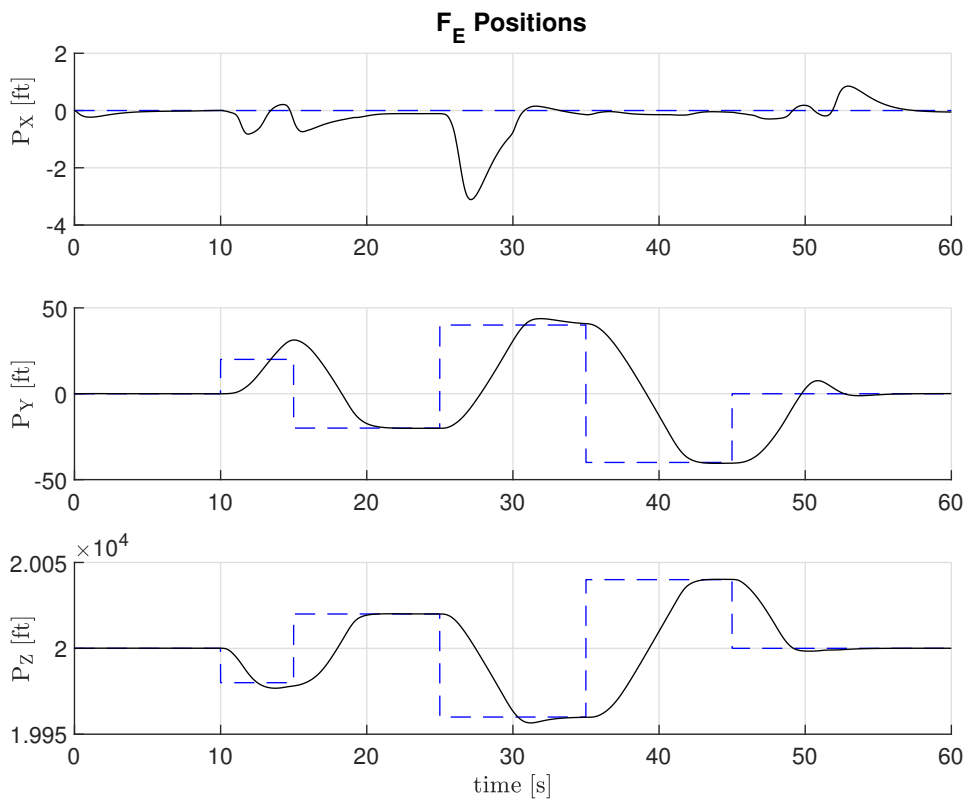
Figure 4.11: Lateral positional control in ft with trimmed attitude and speed hold mode

The translational position control loop works as intended: all elements of the commanded position vector can be followed to a satisfactory degree. As with Full-DoF control, lateral and vertical control response speed is approximately the same. Lateral control does suffer from slight overshoot, however, which can be explained by the previously explained difference in control capacity. Note that axial control is first explored here and performs very well, with very little axial deviation. In addition, the clear downside of using DFC for position control – generating sudden additional drag – is on display around $t = 26$.

The achievement of producing the results shown in fig. 4.11 marks the end of the DFC FCS design phase. The primary goal of designing a Full-DoF FCS has been achieved, thereby answering one of the most important research questions. In addition, the FCS performs well enough to continue investigation into practical use cases with real-life application value.

<div style="text-align: right; font-size: 3em;">5</div>

Practical DFC use cases

The first part of the goal stated in section 3.4 has been achieved: It is indeed possible to *directly* control all six Degrees of Freedom to a degree where control inputs are honored. The positive proof of the 6DoF hypothesis is a major achievement, but useless if the DFC FCS doesn't actually perform better than a conventional control system. If a 6DoF control philosophy does not provide significant control and stability increases, there is no point in actually using such a system.

The applicability of a DFC FCS is tested by means of maneuvers in two categories: air-to-air refueling in section 5.1 and high-crosswind approaches in section 5.2. Each category is divided into further study cases and will be explained in said sections. Conclusions specific to each maneuver category will be given as well.

5.1. Air-to-Air refueling

By far one of the most interesting uses of DFC is during air-to-air refueling scenarios. Such tasks require a very high degree of precision. The use of a more direct control approach – using direct translational control instead of indirect rotational control to achieve lateral displacement – could enable better tracking results for both manual and automatic control. Human controllers prefer systems with first-order behaviour (McRuer and Jex, 1967) as such systems require the least adaption on the human controller's part. Therefore, controlling position by controlling translational velocity is a good candidate.

Of course, systems in which only rotational control is available can be designed such that a translational velocity input is used to compute the adequate rotations. The drawback is that this method requires an additional control loop with associated delays. Therefore, even automatic position control – which does not suffer from issues like maximum effort, concentration loss and other problems associated with manual control – can benefit from the use of a control system in which translational commands are directly linked to translational velocities.

To this end, an air-to-air refueling scenario has been implemented. A Flight Dynamics Model (FDM) for a KC-135 tanker aircraft has been added to the existing simulation model. In addition, the ICE aircraft has been fitted with a "radar". This is a subsystem mimicking radar behaviour which enables the ICE aircraft to find, track and position itself w.r.t the tanker.

5.1.1. Tanker model

The tanker model is based on feedback loops around a 6DoF Euler state propagation block – the same block used in the ICE model. Subscript $_t$ denotes a tanker-related property. The state vector is $[x\ y\ z\ u\ v\ w\ A_x\ A_y\ A_z\ \varphi\ \theta\ \psi\ p\ q\ r\ \dot{p}\ \dot{q}\ \dot{r}\ V_{E_x}\ V_{E_y}\ V_{E_z}\ M\ \alpha\ \beta\ V\ \bar{q}]^T$. The variables M, α, β, V and $\bar{q}$ are calculated using the appropriate blocks. The other variables are state propagation block outputs. The atmosphere model is the 1976 COESA-extended model. Tanker model data were taken from (Smith, 2007, p.62) and Shollenberger et al. (1983) and can be found in table 5.1 and eqs. (5.1) and (5.2).

<div style="text-align: center;">27</div>

Parameter	Value	Unit
m_t	245683	lbs
I_{xx_t}	3797251	slug ft^2
I_{yy_t}	3576204	slug ft^2
I_{zz_t}	7210255	slug ft^2
I_{xz_t}	234574	slug ft^2
S_{ref_t}	2433	ft^2

Table 5.1: Tanker model data

The linear approximation for C_L with α in degrees is

$$C_L = C_{L_0} + \alpha C_{L_\alpha} = 0.2 + 0.116\alpha \tag{5.1}$$

For sideslip, the lateral force coefficient equation with β in degrees is

$$C_Y = \beta C_{Y_\beta} = -0.025\beta \tag{5.2}$$

Forces along the X-axis are assumed to be balanced by the thrust in such a way that the net X-force delivered by the thrust system is driven by the difference between the projection of u on the horizontal plane and a set speed. The first order transfer function $H_T = 1/(s+1)$ is applied to model engine response delay. For the lateral forces, it is assumed that side force due to sideslip and gravity due to roll angle are the acting forces. In the Z-direction, the vertical component of the lift force and gravity are the actors. As such, the forces used as input for the 6DoF Euler block are as follows:

$$\begin{bmatrix} X \\ Y \\ Z \end{bmatrix} = \begin{bmatrix} H_T(K_{P_T} + K_{I_T}\int + K_{D_T} \, d/dt)m(V_{set} - u\cos\theta - w\sin\theta) \\ \beta C_{Y_\beta}\bar{q}S_{ref} + mg\sin\varphi\cos\theta \\ -(C_{L_0} + \alpha C_{L_\alpha})\bar{q}S_{ref} + mg\cos\varphi\cos\theta \end{bmatrix} \text{ with } K_T{}^1 = \begin{bmatrix} 5 & 0 & 10 \end{bmatrix} \tag{5.3}$$

The tanker's attitude is automatically controlled by means of roll angle control in the roll channel, altitude control in the pitch channel and sideslip control in the yaw channel. The first control law is

$$\gamma_c = K_{P_\gamma}(h_c - h_a) + K_{I_\gamma}\int (h_c - h_a) + K_{D_\gamma}\frac{d}{dt}(h_c - h_a) \text{ with } K_\gamma = \begin{bmatrix} 0.001 & 0 & 0.001 \end{bmatrix} \tag{5.4}$$

γ_c is limited to $\pm 10°$. Next, commanded roll angle and angle of sideslip are added:

$$\begin{bmatrix} \dot{\varphi}_c \\ \dot{\theta}_c \\ \dot{\beta}_c \end{bmatrix} = K_{P_1}\begin{bmatrix} \varphi_c - \varphi_a \\ \gamma_c - \theta_a + \alpha_a \\ \beta_c - \beta_a \end{bmatrix} + K_{I_1}\int\begin{bmatrix} \varphi_c - \varphi_a \\ \gamma_c - \theta_a + \alpha_a \\ \beta_c - \beta_a \end{bmatrix} + K_{D_1}\frac{d}{dt}\begin{bmatrix} \varphi_c - \varphi_a \\ \gamma_c - \theta_a + \alpha_a \\ \beta_c - \beta_a \end{bmatrix} \text{ with } K_1 = \begin{bmatrix} 1 & 0 & 0.7 \\ 1 & 0 & 0.85 \\ 3 & 0.5 & 0 \end{bmatrix} \tag{5.5}$$

By means of dynamic inversion, the commanded body rates are obtained:

$$\begin{bmatrix} p_c \\ q_c \\ r_c \end{bmatrix} = A^{-1}\left(\begin{bmatrix} \dot{\varphi}_c \\ \dot{\theta}_c \\ \dot{\beta}_c \end{bmatrix} - \mathbf{b}\right) \text{ with} \tag{5.6}$$

$$A = \begin{bmatrix} 1 & \sin\varphi\tan\theta & \cos\varphi\tan\theta \\ 0 & \cos\varphi & -\sin\varphi \\ \frac{w}{\sqrt{u^2+w^2}} & 0 & \frac{-u}{\sqrt{u^2+w^2}} \end{bmatrix} \text{ and}$$

$$\mathbf{b} = \begin{bmatrix} 0 \\ 0 \\ \frac{1}{\sqrt{u^2-w^2}}\left(\frac{-uv}{V}a_x + \left(1-\frac{v}{V^2}\right)a_y - \frac{vw}{V^2}a_z\right) \end{bmatrix} \text{ where } \begin{bmatrix} a_x \\ a_y \\ a_z \end{bmatrix} = \begin{bmatrix} A_x - g\sin\theta \\ A_y + g\sin\varphi\cos\theta \\ A_z + g\cos\varphi\cos\theta \end{bmatrix}$$

---

[1]For all K_n, the columns corresponds to K_{P_n}, K_{I_n} and K_{D_n}

p_c, q_c and r_c are limited to $\pm 5°/s$, $\pm 1°/s$ and $\pm 10°/s$, respectively. The commanded rotational rate derivatives are calculated using

$$\begin{bmatrix} \dot{p}_c \\ \dot{q}_c \\ \dot{r}_c \end{bmatrix} = K_{P_2} \begin{bmatrix} p_c - p_a \\ q_c - q_a \\ r_c - r_a \end{bmatrix} + K_{I_2} \int \begin{bmatrix} p_c - p_a \\ q_c - q_a \\ r_c - r_a \end{bmatrix} + K_{D_2} \frac{d}{dt} \begin{bmatrix} p_c - p_a \\ q_c - q_a \\ r_c - r_a \end{bmatrix} \text{ with } K_2 = \begin{bmatrix} 5 & 0 & 10 \\ 5 & 0 & 5 \\ 5 & 0 & 5 \end{bmatrix} \tag{5.7}$$

By means of matrix multiplication, the commanded moments are generated:

$$H_{\delta_t} \begin{bmatrix} M_{X_c} \\ M_{Y_c} \\ M_{Z_c} \end{bmatrix} = H_{\delta_t} \left(I_t \begin{bmatrix} \dot{p}_c \\ \dot{q}_c \\ \dot{r}_c \end{bmatrix} \right) = H_{\delta_t} \left(\begin{bmatrix} I_{xx_t} & 0 & I_{xz_t} \\ 0 & I_{yy_t} & 0 \\ I_{xz_t} & 0 & I_{zz_t} \end{bmatrix} \begin{bmatrix} \dot{p}_c \\ \dot{q}_c \\ \dot{r}_c \end{bmatrix} \right) = H_{\delta_t} \begin{bmatrix} I_{xx_t} \dot{p}_c + I_{xz_t} \dot{r} \\ I_{yy_t} \dot{q}_c \\ I_{xz_t} \dot{p}_c + I_{zz_t} \dot{r} \end{bmatrix} \text{ with } H_{\delta_t} = \frac{1}{s+1} \tag{5.8}$$

The assumption is made that the tanker's effectors are able to generate the commanded moments. Also, rotational coefficients are disregarded. For fidelity's sake, the first order transfer function H_{δ_t} is implemented to mimic actuator position delay. Therefore, the commanded moments with delay applied are the moments used as input for the state propagation block. To avoid transient vertical behavior at the start of a simulation, the tanker's initial attitude and body velocities – and therefore AoA – are trimmed.

5.1.2. Radar model

The radar model passes five variables to the rotational and translational outer loops. It is the connection between the tanker aircraft and the ICE aircraft. The five variables are separation distance d_t in ft, relative heading ψ_d, relative elevation angle γ_d, tanker roll angle φ_t and tanker heading angle ψ_t, all in radians. It can reasonably be assumed that a modern radar system is able to generate all stated variables Morgan, with the possible exception of φ_t. A possible solution could be a data link between tanker and ICE aircraft. As such communication is not the subject of this thesis, the assumption is made that φ_t can be passed and is readily available for use in the ICE's FCS computers.

Since there is no actual off-the-shelf radar model, basic mathematics substitutes for this absence. It will become clear that the used equations are a very simplified version of reality, but as radar dynamics and modelling are not a topic of interest in this piece, the fidelity of the equations is not subject to rigorous requirements and therefore will suffice to ensure the system meets the purpose it serves. The first three variables are calculated as shown below, whereas the two latter are passed from the tanker state. Note that variables with subscript $_I$ are from the ICE aircraft state.

$$d_t = \sqrt{(X_t - X_I)^2 + (Y_t - Y_I)^2 + (Z_t - Z_I)^2} \tag{5.9}$$

As the relative heading and elevation angles are passed in the ICE body frame, the position of the tanker has to be calculated in the body frame first. For the remainder of this section *only*, use $X = X_t - X_I$, $Y_E = Y_t - Y_I$ and $Z = Z_t - Z_I$ in the inertial earth-reference frame and use subscripts E for the aircraft-carried earth reference frame (North East Down) and b the body frame. As the orientations of the inertial and aircraft-carried earth reference frames are equal, we can use $X_E = X$, $Y_E = Y$ and $Z_E = Z$ to calculate

$$\begin{bmatrix} X \\ Y \\ Z \end{bmatrix}_b = \mathbb{T}_{bE} \begin{bmatrix} X \\ Y \\ Z \end{bmatrix}_E = \begin{bmatrix} 1 & 0 & 0 \\ 0 & \cos\varphi & \sin\varphi \\ 0 & -\sin\varphi & \cos\varphi \end{bmatrix} \begin{bmatrix} \cos\theta & 0 & -\sin\theta \\ 0 & 1 & 0 \\ \sin\theta & 0 & \cos\theta \end{bmatrix} \begin{bmatrix} \cos\psi & \sin\psi & 0 \\ -\sin\psi & \cos\psi & 0 \\ 0 & 0 & 1 \end{bmatrix} \begin{bmatrix} X \\ Y \\ Z \end{bmatrix}_E \tag{5.10}$$

$$\psi_d = \text{atan2}^{\dagger}(Y_b, X_b) \tag{5.11}$$

$$\gamma_d = \text{atan2}\left(-Z_b, \sqrt{X_b^2 + Y_b^2}\right) \tag{5.12}$$

[†]See https://nl.mathworks.com/help/matlab/ref/atan2.html

5.1.3. Outer loop adjustments and setpoints

Before the radar input data is fit for use in the FCS – both in the DFC and the conventional case – some additional transformations are in order. These ensure the radar data is usable as setpoints for the rotational and translational outer loops. First, rotational control adjustments are treated for both the DFC and Conventional system, after which the translational contrl adjustments for the DFC system are treated.

Rotational Outer Loops

In the DFC case, the rotational outer loop has one simple task: ensure roll and heading angle match those of the tanker. As before, the pitch channel is used to keep the ICE aircraft at the trimmed pitch angle. Therefore, insertion of radar data into the rotational outer loop is straightforward by setting $\varphi_c = \varphi_t$ and $\psi_c = \psi_t$ and using the equations detailed in section 4.4.

For the conventional case, rotational control is responsible for station keeping by means of controlling attitude. Lateral position error is the first input in the roll channel, vertical position error is the first input in the pitch channel and sideslip is the first input in the yaw channel. Calculation of Y_e and Z_e is provided in eq. (5.21). The control laws are as follows:

$$\psi_c = K_{P_1} Y_e + K_{I_1} \int Y_e + K_{D_1} \frac{d}{dt} Y_e \text{ with } K_1 = \begin{bmatrix} 0.005 & 0 & 0.01 \end{bmatrix} \tag{5.13}$$

$$\begin{bmatrix} \varphi_c \\ \gamma_c \end{bmatrix} = K_{P_2} \begin{bmatrix} \psi_c - \psi_a + \psi_t \\ Z_e \end{bmatrix} + K_{I_2} \int \begin{bmatrix} \psi_c - \psi_a + \psi_t \\ Z_e \end{bmatrix} + K_{D_2} \frac{d}{dt} \begin{bmatrix} \psi_c - \psi_a + \psi_t \\ Z_e \end{bmatrix} \text{ with } K_2 = \begin{bmatrix} 4 & 0 & 10 \\ 0.001 & 0 & 0 \end{bmatrix} \tag{5.14}$$

φ_c is limited to $\pm 30°$ and γ_c is limited to $\pm 10°$.

$$\begin{bmatrix} \dot{\varphi}_c \\ \dot{\theta}_c \\ \dot{\beta}_c \end{bmatrix} = K_{P_3} \begin{bmatrix} \varphi_c - \varphi_a \\ \gamma_c - \theta_a + \alpha_a \\ \beta_c - \beta_a \end{bmatrix} + K_{I_3} \int \begin{bmatrix} \varphi_c - \varphi_a \\ \gamma_c - \theta_a + \alpha_a \\ \beta_c - \beta_a \end{bmatrix} + K_{D_3} \frac{d}{dt} \begin{bmatrix} \varphi_c - \varphi_a \\ \gamma_c - \theta_a + \alpha_a \\ \beta_c - \beta_a \end{bmatrix} \text{ with } K_3 = \begin{bmatrix} 2 & 0 & 0.1 \\ 2 & 0 & 2 \\ 2 & 1 & 0 \end{bmatrix} \tag{5.15}$$

Note that $\beta_c = 0$ unless stated otherwise.

$$\begin{bmatrix} p_c \\ q_c \\ r_c \end{bmatrix} = A^{-1} \left(\begin{bmatrix} \dot{\varphi}_c \\ \dot{\theta}_c \\ \dot{\beta}_c \end{bmatrix} - \mathbf{b} \right) \text{ with } A, \mathbf{b} \text{ as in eq. (5.6) using } [\varphi \, \theta \, \psi]_I \tag{5.16}$$

These commanded body rates are the input for the unaltered rotational inner loops. As the previously used DFC thrust input system is unavailable, the axial position error has to be entered into the A/T system to be able to control thrust. The control law for the commanded airspeed is as follows:

$$V_c = V_{des_t} \frac{\cos \theta_t}{\cos \theta_I} + K_P X_e + K_D \frac{d}{dt} X_e \text{ with } K_P = 0.25, K_D = 1 \tag{5.17}$$

The term $K_P X_e + K_D \frac{d}{dt} X_e$ is limited to ± 100 ft/s. V_c is entered in the unaltered velocity control loop.

Translational Outer Loops

The translational control loop adjustment starts with using the radar inputs. These have to be converted to positions in the body frame, which are then converted to positions in the ICE aircraft-carried earth reference frame. This second conversion is an necessity as the total position consists of the position difference between the two aircraft and the position of the boom w.r.t. the tanker center of gravity. These can easily be added in the ICE-carried earth reference frame if the position of the boom can be converted into a vector in the tanker-carried earth reference frame, which is a straightforward transformation already demonstrated. Therefore, the equations to obtain the position error in the ICE-carried earth reference frame are the following:

$$P_{I_b} = \begin{bmatrix} X \\ Y \\ Z \end{bmatrix}_b = \begin{bmatrix} d_t \cos \gamma_d \cos \psi_d \\ d_t \cos \gamma_d \sin \psi_d \\ -d_t \sin \gamma_d \end{bmatrix} \tag{5.18}$$

$$P_{I_E} = \mathbb{T}_{Eb} P_{I_b} = \begin{bmatrix} \cos\psi_I & -\sin\psi_I & 0 \\ \sin\psi_I & \cos\psi_I & 0 \\ 0 & 0 & 1 \end{bmatrix} \begin{bmatrix} \cos\theta_I & 0 & \sin\theta_I \\ 0 & 1 & 0 \\ -\sin\theta_I & 0 & \cos\theta_I \end{bmatrix} \begin{bmatrix} 1 & 0 & 0 \\ 0 & \cos\varphi_I & -\sin\varphi_I \\ 0 & \sin\varphi_I & \cos\varphi_I \end{bmatrix} \begin{bmatrix} X \\ Y \\ Z \end{bmatrix}_b \tag{5.19}$$

$$P_{boom_E} = \mathbb{T}_{Eb} P_{boom_t} = \begin{bmatrix} \cos\psi_t & -\sin\psi_t & 0 \\ \sin\psi_t & \cos\psi_t & 0 \\ 0 & 0 & 1 \end{bmatrix} \begin{bmatrix} \cos\theta_t & 0 & \sin\theta_t \\ 0 & 1 & 0 \\ -\sin\theta_t & 0 & \cos\theta_t \end{bmatrix} \begin{bmatrix} 1 & 0 & 0 \\ 0 & \cos\varphi_t & -\sin\varphi_t \\ 0 & \sin\varphi_t & \cos\varphi_t \end{bmatrix} \begin{bmatrix} x_{boom} \\ y_{boom} \\ z_{boom} \end{bmatrix} \tag{5.20}$$

$$P_{e_E} = P_{I_E} + P_{boom_E} \tag{5.21}$$

The position error P_{e_E} of the ICE aircraft w.r.t the end of the boom in the ICE-carried earth reference frame can be entered into the outer translational control loops by substitution of $P_c - P_a$ in eq. (4.10). With that, the connection between the tanker aircraft and the ICE DFC FCS is completed, making it suitable for testing.

5.1.4. FCS comparison
The ability of the conventional and the DFC FCS to follow a tanker in an air-to-air refueling is tested in four types of scenarios, divided into two pattern categories and three turbulence categories. A schematic breakdown is given in table 5.2.

Table 5.2: Various tanker tracking cases

| Turbulence | Turn | |
ICE	No	Yes
No	$0° \times [100, 1000]$ ft	$[10°, 20°, 30°]$
Yes	$[1, 2, \ldots, 6] \times 0°$	$[1, 2, \ldots, 6] \times [10°, 20°, 30°]$

In total, this gives 58 datasets. For selected scenarios, the results for both FCS types will be graphed, quantitatively interpreted and discussed. First, offset effects will be discussed. Next, influence of turbulence in steady straight flight is analyzed. Finally, steady turns without and with turbulence are treated.

In practice, a refueling scenario will start with the receiver aircraft at some offset to the end of the refueling boom. Therefore, the effect of different offset distances is observed for both FCS types. Offset denotes boom end distance from the inertial $\mathbb{F}_E$ frame, which is the starting position for the ICE aircraft after altitude has been added. In the tanker state propagation block, boom end to tanker C.O.G. distance is added to the offset to ensure a correct tanker starting position. The results are shown in fig. 5.1.

Throughout this section, position errors are presented in the tanker body frame. Z_e has been reversed, such that the graphical results can be interpreted as altitude errors, with a negative error indicating a lower receiver aircraft altitude w.r.t the tanker altitude.
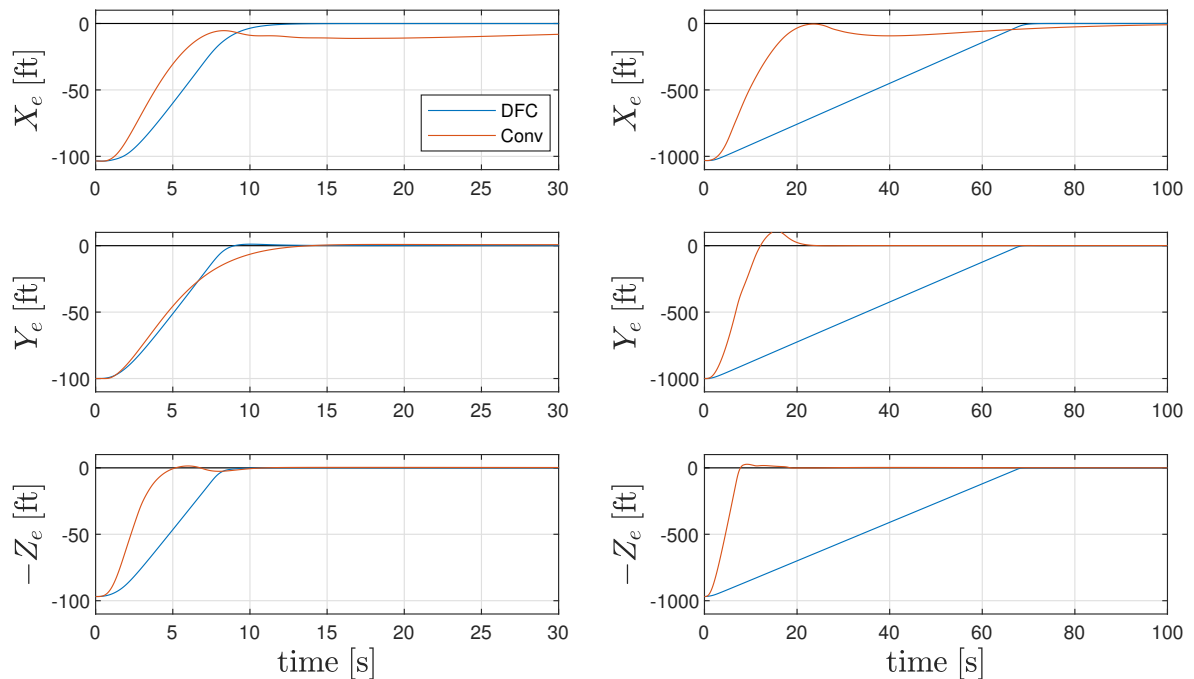
Figure 5.1: Position errors for both FCS with initial tanker offsets of [100, 100, 100] (left) and [1000, 1000, 1000] (right)

Clearly, the DFC method of control is not suitable for traversing large distances. This is due to the limitation of ±15 ft/s placed on the system. In fact, it takes the DFC system 72, 68.5 and 68.5 seconds to get X_e, Y_e and Z_e, respectively, within 1 ft. These rise times are 236%, 131% and 154% larger than the conventional settling times. The contrast with the 100 ft offset situation is very large. Although rise times for the conventional system are better for lateral and vertical distance, the DFC settling times are 48%, 44% and 14% less than the conventional settling times.

It must be said that additional tuning might enhance conventional settling times by better damping of higher-order dynamics, but the point about the stark contrast stands nonetheless. A counterargument can also be made for the fact that additional tuning of the translational DFC loops will enhance their rise and settling times as well.

There is, however, a limit as to what translational velocities are controllable with snappy responses. Using higher velocity limits without overshoot requires generation of more lead by means of error differentiation in the PIDs, which can deteriorate precision tracking. As the latter is much more valuable for air-to-air refueling scenarios – which will become apparent later in this section – the usage of higher limit velocities does not improve overall system performance in said scenarios. As such, a FCS designed around DFC-based displacement is simply not the best choice for traversing large distances; the underlying design philosophy does not match such a control task. On the other hand, the differences between rise and setting times are a reflection of the point made at the start of section 5.1 about the effect higher-order systems. The design philosophy behind the DFC system is to avoid such higher-order dynamics and therefore enable better tracking of high-frequency inputs. It is to this end that the DFC system's rise and settling times are much closer than for the conventional system.

The scenarios tested above have ideal atmospheric conditions. To increase situation fidelity, turbulence is added. This is done by enabling the built-in Dryden Wind Turbulence Model block. Used parameters are shown in table 5.3 below. Since scenarios are at high altitude, low-altitude parameters are omitted. The block's connections to the rest of the model are discussed in the next paragraph.

The Probability of Exceedance, which sets the intensity of the turbulence, is used as as variable as is varied throughout this section. It takes the form 10^{-k}, with $k = [1, 2, \ldots, 6]$, as in table 5.2. A higher value for k

Table 5.3: Dryden Turbulence Parameters

Parameters	Value
Specification	MIL-F8785-C
Model Type	Continuous Dryden (+q -r)
Scale length	533.4
Wingspan	b_{ref_I}
Noise sample time	0.01
Noise seeds [ug vg wg pg]	[23341 23342 23343 23344]

indicates a higher intensity. A value of 2 is considered light turbulence, 3 is moderate and 5 is severe. The generated parameters $V_{wind} = [ug\ vg\ wg]^T$ in ft/s and $\omega_{wind} = [pg\ qg\ rg]^T$ in rad/s are added to the body velocities and angular rates. The resultant velocities are used to calculate V, α, β, M and $\bar{q}$ and these parameters are added to the state of the aircraft. The resultant angular rates are directly fed back into the aerodynamic model.

To best sketch a turbulence-affected situation, a selection of the 12 available dataset is shown graphically in fig. 5.2. In addition, all datasets will be quantified in terms of tracking error. All straight turbulence scenarios have an offset of [100 100 100].
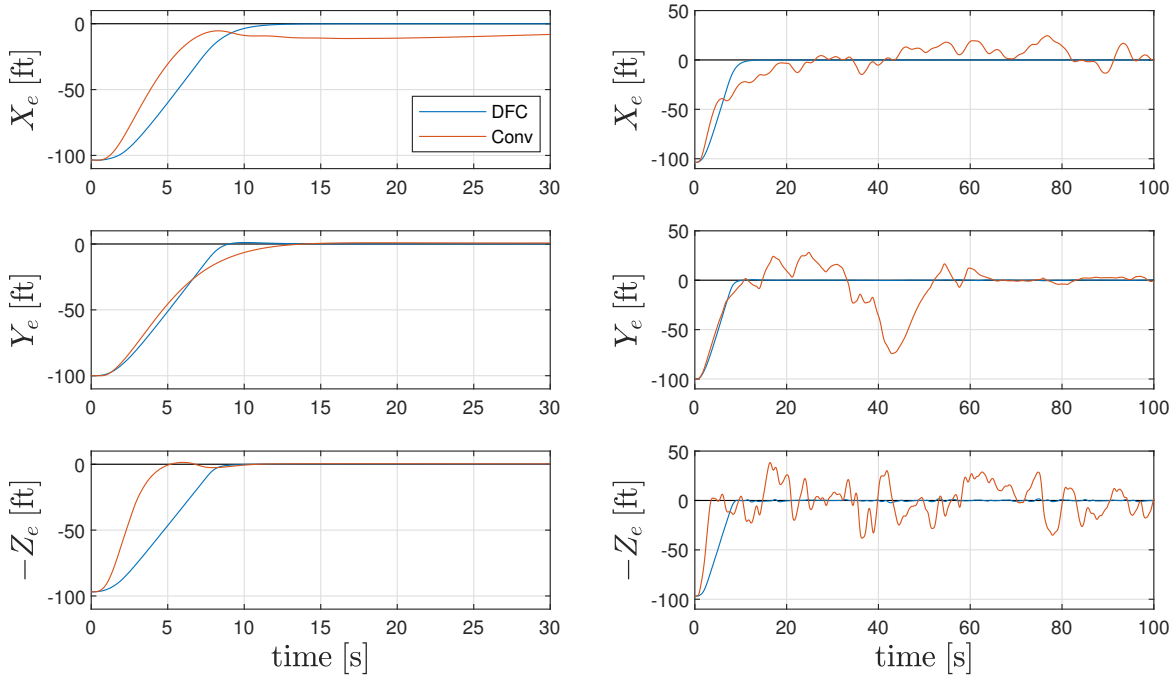
Figure 5.2: Position error during approach with offset [100, 100, 100] for $k = 1$ (left) and $k = 3$ (right)

The graphs on the left side are very similar to the steady approach scenario shown on the left side of fig. 5.1. Clearly, turbulence has very little effect on either system. For the increased turbulence shown on the right side of fig. 5.2, this is not the case: especially lateral control in the conventional system suffers greatly. Axial and vertical error also clearly deteriorate. On the other hand, the DFC system seems largely unaffected. Visually, the graphs for $k = 1$ and $k = 3$ do not seem to differ – except for the shorter time space, that is. It will become apparent that there is in fact a difference, but this difference is very small.

For the steady turn scenarios, the initial offset is set to [0 0 0]; the aircraft is in perfect position w.r.t the boom. The roll angle applicable to the scenario is multiplied by the Heaviside function $H_{10}(t)$ and that value is entered in substitution of φ_c in eq. (5.5). 10%-90% rise times are [3.62 4.30 5.44] seconds and 2% settling

times are [6.35 7.29 8.65] seconds for 10°, 20° and 30°, respectively.

The Root Mean Square error is used to compare different datasets across different systems, turbulence settings, roll angles and axes. For all datasets, the first 20 seconds (on a total of 100 seconds) are not used to calculate RMS. This measure ensures transient behaviour due to initial offset or turn start is disregarded and therefore comparison between steady-state errors of straight and turn scenarios is possible.
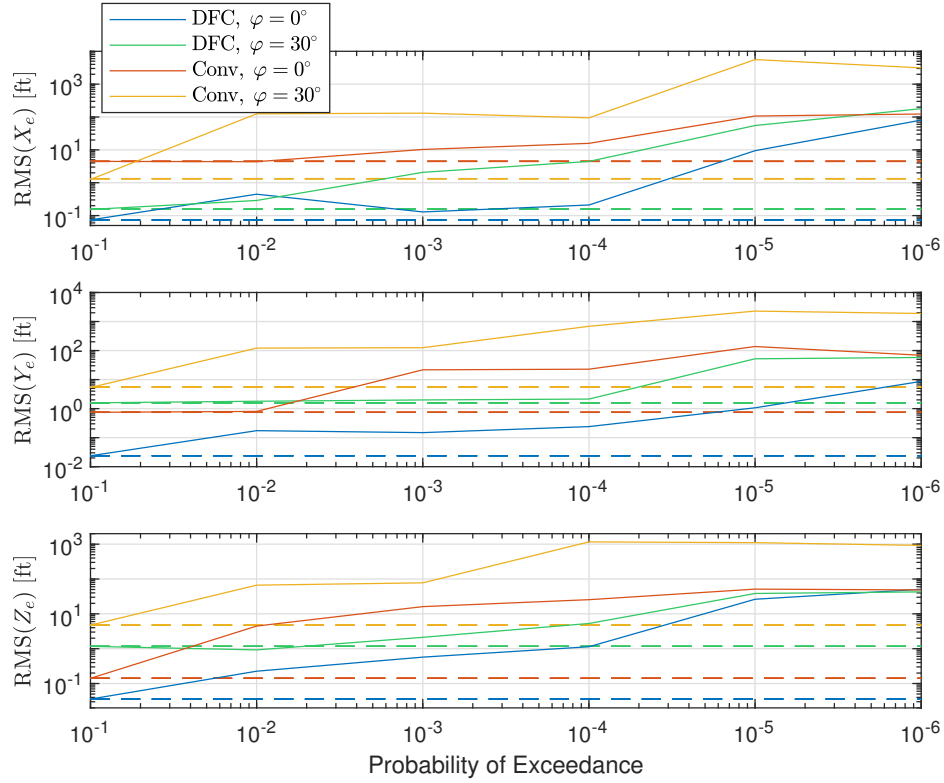
Figure 5.3: Comparison of FCS types by RMS values of turbulence-free baseline and all turbulence settings

It is abundantly clear from fig. 5.3 that the DFC system performs better in every single situation. In fact, the DFC system performs better than the Conventional baseline in axial and lateral direction for all but the two most severe turbulence settings. This can be expected, as the axial A/T system and the lateral three-outer-loop control system are the biggest weaknesses. For the DFC system, a deviation in θ has a much larger effect on vertical control than similar deviations of φ and ψ have on lateral control. This might explain the difference in performance w.r.t. the Conventional baseline for the steady scenario; the Conventional baseline is better than the DFC baseline. When it comes to vertical turbulence rejection, however, the DFC system is still much better than the Conventional system. The baseline for the 30° turn is also better for the DFC system.
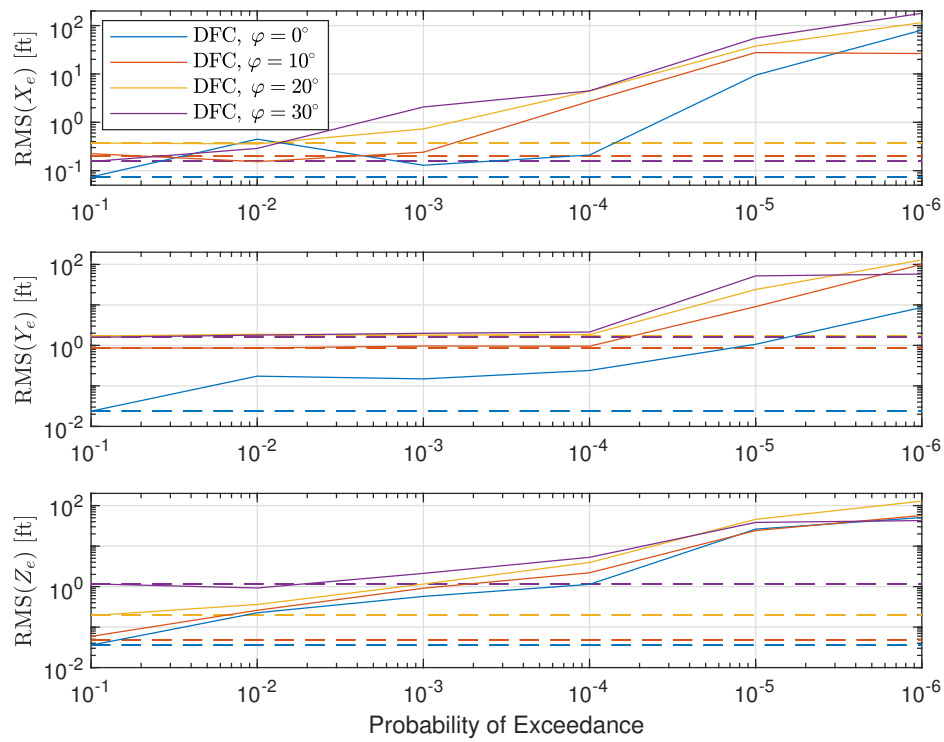
Figure 5.4: Effect of roll angle on position RMS and turbulence-free baselines for the DFC system with turbulence-free baselines

An increasing roll angle has a negative effect on the tracking performance. The order of the error is relatively the same, however, as magnitude of turbulence has a larger effect than roll angle. When looking at the differences between axes, the axial turn baselines are all very low, whereas turn baselines for lateral error are larger, but all of the same order. In addition, lateral control barely deviates from the baseline up to $k = 4$, a feat not seen for axial or vertical control. Vertical baselines suffer the most from increasing roll angle.
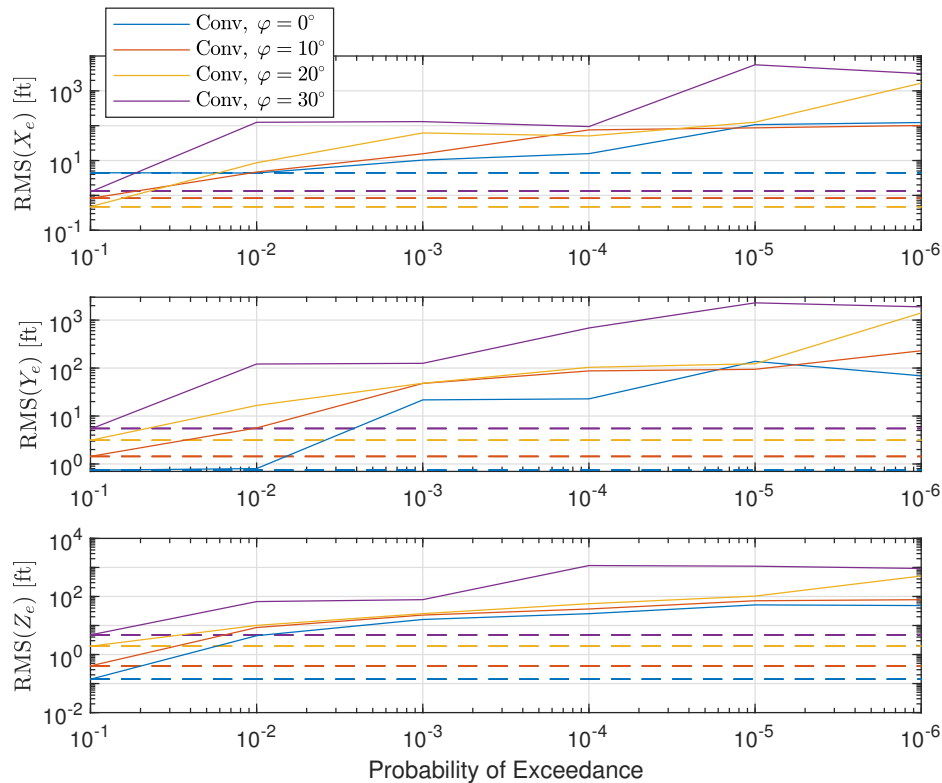
Figure 5.5: Effect of roll angle on position RMS and turbulence-free baselines for the Conventional system

Conventional baselines are more predictable in the sense that a higher roll angle induces a higher baseline for all translational control directions. This also mostly holds true for turbulence-affected scenarios. High-turbulence and roll angle combinations suffer from gain margin deterioration up to the point of instability: for $\varphi = 20°, 30°$ with $k = 4$ as well as for all roll angles with $k \geq 5$, velocity, pitch and roll gains had to be reduced to ensure stability. For $\varphi = 20°$ with $k = 6$ and $\varphi = 30°$ with $k = 4, 5, 6$, errors were within bounds similar to lower roll angles but the scenario was not considered stable. Compare this to the DFC system, for which all situations were stable with one and the same set of system parameters.

5.2. High-crosswind landings

High-crosswind landings are simulated using a fixed approach trajectory to a set point, called the beacon B. This beacon is located at the center of the start of the target runway. The heading of the runway ψ_R is used to rotate the earth-fixed reference frame $\mathbb{F}_E$ around the Z-axis to obtain the runway frame $\mathbb{F}_R$, with origin in B, the X-axis along the center line of the runway, the Z-axis directly down and the Y-axis to the right to complete the right-handed frame.

5.2.1. Approach Trajectory and Deviations

The approach trajectory is a standard glide slope with $\gamma_s = -3°$ through B on the XZ plane of $\mathbb{F}_R$. The ICE aircraft is placed on this glideslope at an altitude of 3000 ft and trimmed at the conditions for FL=100, $V_{TAS} = 430$ ft/s, lightweight. From this point, the aircraft is required to follow the glide slope and decelerate from the trimmed speed V_{des} to the final approach speed V_{app}. Conditions for the flare are an X-distance smaller than $h_f/tan|\gamma_s|$ and $h \leq h_f$. When both conditions are met, the aircraft performs a flare maneuver and attempts to land with an acceptable rate of descent.

The aircraft gets a fix on the beacon B in a way similar to the lock-on method for the tanker following system. The radar again relays d_R, ψ_d, γ_d to the outer loops, with ψ_R assumed to be available from the FMS as target runway heading is known beforehand. Like for the tanker, the radar signals are calculated by

$$d_R = \sqrt{(X_B - X_I)^2 + (Y_B - Y_I)^2 + (Z_B - Z_I)^2} \tag{5.22}$$

For the remainder of this section *only*, use $X = X_B - X_I$, $Y = Y_B - Y_I$ and $Z = Z_B - Z_I$ in the inertial earth-reference frame and use subscripts E for the aircraft-carried earth reference frame (North East Down) and b the body frame. As the orientations of the inertial and aircraft-carried earth reference frames are equal, we can use $X_E = X$, $Y_E = Y$ and $Z_E = Z$ to calculate the position of B relative to ICE in $\mathbb{F}_b$:

$$\begin{bmatrix} X \\ Y \\ Z \end{bmatrix}_b = \mathbb{T}_{bE} \begin{bmatrix} X \\ Y \\ Z \end{bmatrix}_E = \begin{bmatrix} 1 & 0 & 0 \\ 0 & \cos\varphi & \sin\varphi \\ 0 & -\sin\varphi & \cos\varphi \end{bmatrix} \begin{bmatrix} \cos\theta & 0 & -\sin\theta \\ 0 & 1 & 0 \\ \sin\theta & 0 & \cos\theta \end{bmatrix} \begin{bmatrix} \cos\psi & \sin\psi & 0 \\ -\sin\psi & \cos\psi & 0 \\ 0 & 0 & 1 \end{bmatrix} \begin{bmatrix} X \\ Y \\ Z \end{bmatrix}_E \tag{5.23}$$

$$\psi_d = \text{atan2}(Y_b, X_b) \tag{5.24}$$

$$\gamma_d = \text{atan2}\left(-Z_b, \sqrt{X_b^2 + Y_b^2}\right) \tag{5.25}$$

The outer loops use these radar inputs to calculate the position of the aircraft in $\mathbb{F}_R$:

$$P_R = \begin{bmatrix} X \\ Y \\ Z \end{bmatrix}_R = \mathbb{T}_{Rb} \begin{bmatrix} X \\ Y \\ Z \end{bmatrix}_b = \mathbb{T}_{Rb} \begin{bmatrix} d_t \cos\gamma_d \cos\psi_d \\ d_t \cos\gamma_d \sin\psi_d \\ -d_t \sin\gamma_d \end{bmatrix} \text{ with } \mathbb{T}_{Rb} = \mathbb{T}_{Eb} \text{ for which } \psi = \psi_I - \psi_R \tag{5.26}$$

As P_R is the ICE position in $\mathbb{F}_R$ relative to B, it is easy to see that the lateral error l w.r.t. the glide slope in the XZ-plane is $l = -Y_R$. The vertical error during the first phase of the approach is given by:

$$h_e = h_c - h_a = \sqrt{X_R^2 + Z_R^2} \sin\gamma_s - h_a \tag{5.27}$$

For the flare phase, the vertical error is given by

$$h_e = h_{c_f} - h_a = (h_f + h_o)e^{Kt} - h_o - h_a \text{ with } K = \frac{V_{app}\sin(\gamma_s)}{h_f + h_o} \text{ and } t = 0 \text{ for } h = h_f \tag{5.28}$$

h_o is a term manipulating the flare such that floating is prevented. In addition, the glide slope γ_s during the flare is given by

$$\gamma_s = \sin^{-1}\left(\frac{K(h_f + h_o)e^{Kt}}{V_{app}}\right) \tag{5.29}$$

The commanded total velocity V_c during the approach phase is given by

$$V_c = d_e K_V + V_{app} = \left(\sqrt{X_R^2 + Z_R^2} - d_2\right)\frac{V_{des} - V_{app}}{d_1 - d_2} + V_{app} \tag{5.30}$$

Here, d_1 is the distance from B on the XZ-plane for which deceleration from V_{des} to V_{app} start and d_2 is the distance at which deceleration should be completed. Also, V_c is limited to $[V_{app} \; V_{des}]$ and $V_c = V_{app}$ for $X_R < 0$.

5.2.2. Outer Loop control strategies

Three possible control strategies have been identified for both lateral and vertical control. Each control strategy has a different philosophy and uses a different combination of conventional and DFC control. The rotational and translational outer loops are shown in figs. 5.6 and 5.7, respectively.

The lateral strategies are A to C corresponding to $S_l = 1$ to 3. The vertical strategies are 1 to 3, which correspond to S_v. This gives a total of 9 possible combined control strategies. All control laws are given in

Figure 5.6: Rotational Outer loops

Figure 5.7: Translational Outer loops

tables 5.4 and 5.5 and eq. (5.31). For the symmetrical Degree of Freedom surge along the X-axis, the control law is always the same:

$$V_{R_{X_c}} = \sqrt{V_c^2 - V_{R_{Y_a}}^2 - V_{R_{Z_a}}^2} \text{ with } V_{R_a} = \mathbb{T}_{Rb} V_{b_a} \tag{5.31}$$

Table 5.4: Control laws for lateral control

Strategy	φ_e	ψ_e	$V_{R_{Y_c}}$
A	$\varphi_c - \varphi_a$	$\psi_R - \psi_a$	$0, a_{55} = 0$
B	$-\varphi_a$	$\psi_c + \psi_R - \psi_a$	$0, a_{55} = 0$
C	$-\varphi_a$	$\psi_R - \psi_a$	$\dot{l}_c$

Table 5.5: Control laws for vertical control

Strategy	θ_e	$V_{R_{Z_c}}$
1	$\gamma_c + \gamma_s - \theta_a + \alpha_a$	$0, a_{66} = 0$
2	$\theta_{trim} + \gamma_s - \theta_a$	$\dot{h}_c$
3	$\theta_{dyn} - \theta_a$	$\dot{h}_c$

All parameters in tables 5.4 and 5.5 are taken from the aircraft state, previously known or given by the equations in section 5.2.1 or below.

$$V_{R_{Y_c}} = K_{P_{\varphi_1}} l + K_{I_{\varphi_1}} \int l + K_{D_{\varphi_1}} \frac{d}{dt} \tag{5.32}$$

$$\varphi_c = K_{P_{\varphi_2}} (V_{R_{Y_c}} - V_{R_{Y_a}}) + K_{I_{\varphi_2}} \int (V_{R_{Y_c}} - V_{R_{Y_a}}) + K_{D_{\varphi_2}} \frac{d}{dt} (V_{R_{Y_c}} - V_{R_{Y_a}}) \tag{5.33}$$

$$\gamma_c = K_{P_\theta} h_e + K_{I_\theta} \int h_e + K_{D_\theta} \frac{d}{dt} h_e \tag{5.34}$$

$$V_{R_{Y_c}} = K_{P_{\psi_1}} l + K_{I_{\psi_1}} \int l + K_{D_{\psi_1}} \frac{d}{dt} l \tag{5.35}$$

$$\psi_c = K_{P_{\psi_2}} (V_{R_{Y_c}} - V_{R_{Y_a}}) + K_{I_{\psi_2}} \int (V_{R_{Y_c}} - V_{R_{Y_a}}) + K_{D_{\psi_2}} \frac{d}{dt} (V_{R_{Y_c}} - V_{R_{Y_a}}) \tag{5.36}$$

$$\begin{bmatrix} \dot{l}_c \\ \dot{h}_c \end{bmatrix} = K_{P_Y} \begin{bmatrix} l \\ h_e \end{bmatrix} + K_{I_Y} \int \begin{bmatrix} l \\ h_e \end{bmatrix} + K_{D_Y} \frac{d}{dt} \begin{bmatrix} l \\ h_e \end{bmatrix} \tag{5.37}$$

Note that even though eqs. (5.32) and (5.35) are similar their PID gains are not, nor is their usage in of the calculated value in eqs. (5.33) and (5.36), respectively. Controller gains can be found in appendix B.1.

The value of θ_{dyn} is derived from a lookup table containing the trimmed pitch angle values for all trim points for all weight conditions, sorted from low to high dynamic pressure. Therefore, the pitch angle of the aircraft is such that it best matches the current dynamic pressure. As such, there is no exact formula for θ_{dyn}. The approximation is given in eq. (5.38). All lookup table data points are shown in table B.2.

$$\theta_{dyn} = f(h, V_{TAS}, m) \tag{5.38}$$

Strategies A to C and 1 & 2 use one active DoF for each direction, which is responsible for control of that direction's error. For strategy 3, a auxiliary DoF aids the primary DoF if the situation requires this, which can be seen as a hybrid control strategy.

For conversion to the inner loop inputs ω_c and V_{b_c}, the following equations are used:

$$\omega_c = \begin{bmatrix} p_c \\ q_c \\ r_c \end{bmatrix} = \begin{bmatrix} 1 & 0 & -\sin\theta \\ 0 & \cos\varphi & \sin\varphi\cos\theta \\ 0 & -\sin\varphi & \cos\varphi\cos\theta \end{bmatrix} \left(K_{P_\omega} \begin{bmatrix} \varphi_e \\ \gamma_e \\ \psi_e \end{bmatrix} + K_{I_\omega} \int \begin{bmatrix} \varphi_e \\ \gamma_e \\ \psi_e \end{bmatrix} + K_{D_\omega} \frac{d}{dt} \begin{bmatrix} \varphi_e \\ \gamma_e \\ \psi_e \end{bmatrix} \right) \tag{5.39}$$

$$V_{b_c} = \mathbb{T}_{bR} V_{R_c} - V_0 \tag{5.40}$$

5.2.3. Control strategy comparisons

The control strategies given in section 5.2.2 are tested by means of flying the approach and flare outlined in section 5.2.1. The aircraft is offset 300 ft to the left of the top of the glideslope and is trimmed for steady straight flight with no wind. To evaluate crosswind landing performance, a crosswind component is implemented by means of enabling the built-in Wind Shear model. Performance will be evaluated in terms of rise time to glide slope, RMS errors, maximum deviation and touchdown situation. Crosswinds of 0, 10 20 and 30 knots are used, with a wind direction of $\psi_R + 90°$. For details on how this crosswind is implemented in the model, please see the explanation accompanying table 5.3. Values of other parameters are $V_{des} = 430$ ft/s, $V_{app} = 230$ ft/s, $d_1 = 30000$ ft, $d_1 = 3000$ ft and $b = 30$ (see eq. (4.6)), unless stated otherwise.

Control loops for each strategy have been tuned for performance in the the zero-wind conditions and, where possible, kept the same throughout wind-enabled scenarios. If applicable, changing of control gains and the reason behind it is discussed. A list of the zero-wind controller settings and any changes between scenarios can be found in appendix B.1.

There are 9 control strategies tested for four conditions, giving a total of 36 datasets. Landing situation parameters, together with any notes, are givin in table 5.6. For each control strategy, general observations are discussed. As in section 5.1.4, specific cases are highlighted to paint a picture of the strengths and weaknesses of each strategy. Selection may vary for different performance criteria as deemed necessary.

Control Strategy		Wind [ft/s]	X [ft]	Y [ft]	$\dot{l}$ [ft/s]	$\dot{h}$ [ft/s]	φ [°]	θ [°]	ψ [°]	Notes
A	1	0	-131	0.48	-0.14	-6.73	0.45	13.5	0.00	Stable
		10	-58.6	0.68	-0.06	-9.20	-0.38	12.5	0.00	Stable
		20	-48.2	1.21	-0.06	-9.22	-0.05	12.5	0.00	Stable
		30	-690	2.68	0.19	-1.58	-0.15	13.7	0.01	Stable, initial vertical oscillations
	2	0	-65.9	-0.26	0.03	-17.5	-0.25	2.89	0.00	Unstable vertical end, $V_{app} = 350$
		10	-84.1	-0.72	0.14	-19.4	0.86	2.87	0.00	Unstable vertical end, $V_{app} = 380$
		20	-92.2	0.96	0.17	-18.5	0.30	2.84	0.01	Unstable vertical end, $V_{app} = 370$
		30	-399	0.78	0.14	-18.6	0.82	2.87	0.00	Unstable vertical end, $V_{app} = 360$
	3	0	176	-0.23	0.03	-10.2	-0.05	12.9	0.00	Stable
		10	207	0.66	0.06	-10.5	0.11	12.9	0.00	Stable
		20	290	-0.26	0.16	-11.6	0.77	12.8	0.00	Stable
		30	-98.9	0.68	0.49	-6.55	0.41	12.8	0.02	Stable, initial vertical oscillations
B	1	0	-224	21.5	-1.95	-6.69	0.03	8.41	-2.63	Unstable lateral, $V_{app} = 310$
		10	-93.0	-21.3	2.19	-8.89	0.00	10.9	2.47	Unstable lateral, $V_{app} = 250$
		20	-214	-22.7	1.78	-8.02	0.06	6.56	3.32	Unstable lateral, $V_{app} = 350$
		30	-167	-18.8	1.41	-10.5	0.02	4.45	6.28	Unstable lateral, $V_{app} = 410$
	2	0	-51.5	7.42	-0.50	-17.9	0.00	2.89	-1.07	Unstable lateral & vertical, $V_{app} = 350$
		10	-71.6	-11.9	0.58	-17.8	0.01	2.86	2.17	Unstable lateral, $V_{app} = 360$
		20	-73.3	-14.1	0.65	-19.8	-0.09	2.69	5.10	Unstable lateral & vertical, $V_{app} = 380$
		30	-77.0	-21.5	1.24	-18.4	0.03	2.83	7.65	Unstable lateral & vertical, $V_{app} = 370$
	3	0	162	18.4	-0.33	-11.8	-0.01	10.2	-3.96	Unstable lateral, $V_{app} = 280$
		10	107	8.44	-4.08	-10.5	0.00	10.8	2.64	Unstable lateral, $V_{app} = 270$
		20	204	-24.5	1.50	-15.2	0.03	6.74	4.11	Unstable lateral, $V_{app} = 350$
		30	-121	-22.8	1.73	-9.40	0.02	8.12	7.51	Unstable lateral, $V_{app} = 320$
C	1	0	-132	0.00	0.00	-6.95	0.00	12.9	0.00	Stable, large lateral overshoot
		10	-143	-0.02	0.00	-6.60	0.02	12.4	0.00	Stable
		20	-70.6	0.01	0.00	-8.45	0.07	12.0	0.01	Stable
		30	-604	-0.03	0.00	-3.24	0.02	13.0	0.00	Stable, initial lateral undershoot
	2	0	-45.4	0.01	0.01	-18.2	0.00	2.85	0.01	Unstable vertical end, $V_{app} = 350$
		10	-76.2	-0.19	-0.13	-19.8	0.09	2.78	-0.42	Unstable vertical end, $V_{app} = 380$
		20	30.9	-0.16	-0.22	-17.8	0.06	2.89	-0.16	Unstable lateral & vertical, $V_{app} = 360$
		30	34.6	0.06	0.10	-18.9	0.07	2.88	0.07	Unstable lateral & vertical, $V_{app} = 380$
	3	0	17.2	0.00	0.00	-7.74	0.01	12.9	0.00	Stable
		10	29.0	0.00	0.00	-7.84	0.04	12.9	0.01	Stable, lateral overshoot
		20	-812	0.19	-0.02	-2.01	0.00	12.8	0.01	Semi-stable, large lateral oscillations
		30	-816	0.14	-0.02	-2.00	0.02	12.8	0.01	Stable, slow vertical error correction

Table 5.6: Approach trajectory results

A1

The most conventional strategy – save for keeping ψ_a at ψ_R – performs adequately for all wind conditions. The nonzero roll angle does deteriorate initial vertical tracking performance due to cross-coupling effects, but the strategy performs decently overall.

A2

When active flight path control in the pitch channel is replaced with a steady pitch, initial vertical oscillations are reduced, but at the cost of a slowly decreasing vertical steady-state error. Keeping pitch at a fixed value does improve lateral tracking, as the roll-pitch cross-coupling does not exist. It is more smooth and accurate compared to A1.

The problem with this strategy, however, is that the final approach speed needs to be increased a lot to ensure the vertical DFC control can handle the requested vertical velocities and accelerations. This is because the dynamic pressure decreases to unacceptable levels for the normal approach, which causes the aircraft to simply start dropping from the sky. The effector suite does not have enough force generation power to keep the aircraft in the sky at the requested descent rate.
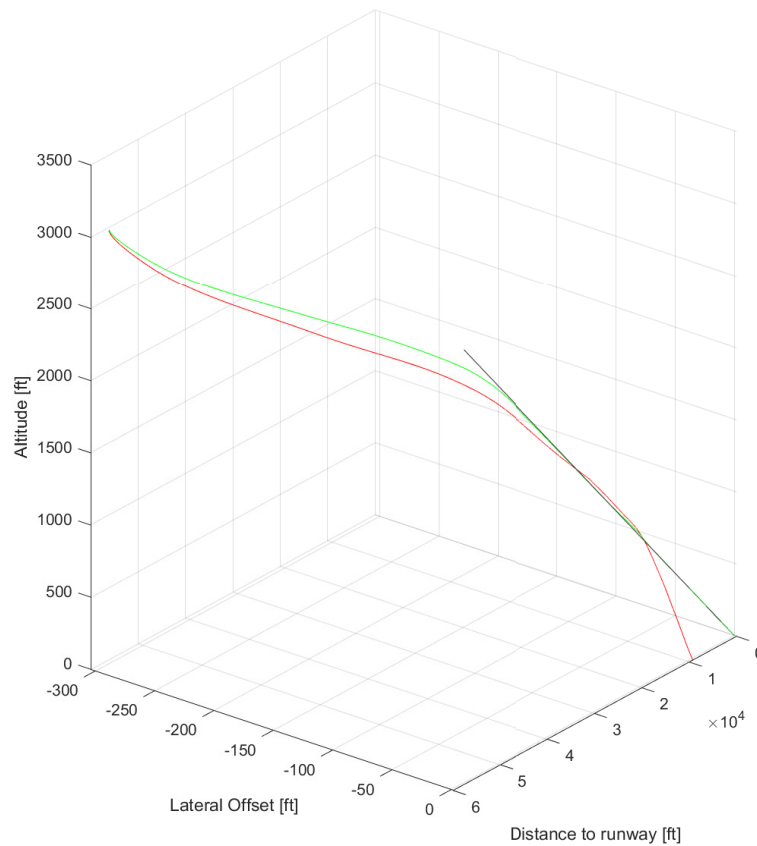
Figure 5.8: Comparison of static (A2, red) and dynamic (A3, green) passive pitch control

A3

The problem with vertical control in A2 is solved by using a dynamic commanded pitch angle as explained in the text accompanying eq. (5.38). This modification enables the airframe to do the heavy lifting in terms of lift generation, while vertical DFC is used to correct the vertical error to the glide slope. The benefit is that lateral control is as sharp as for A2, but the aircraft actually maintains altitude at lower dynamic pressures. This is shown in fig. 5.8. The downside of not actively using pitch angle is reflected in the fact that the flare is poorly executed – as seen in the values for $\dot{h}$. This can easily be corrected by enabling active pitch control during the flare phase (which has not been done in this study as it is not a topic of interest). The advantage is the absence of roll-pitch coupling.

The long-standing vertical steady state error also seen in A2 remains, but the error is acceptable. Therefore integrator gain for $\dot{h}_c$ in K_T is kept at zero, as use of a nonzero integrator term was difficult in terms of stability and applicability for all crosswind values. This is the reason behind this trade-off. The result is a slower (but still adequate) response in terms of vertical error settling time (see table B.3) but a more stable vertical flight path than for A1 due to the suppression of roll-pitch coupling, especially for high-crosswind values. That makes this strategy the preferred option.

All B strategies

The use of yaw as primary control channel for countering crosswind might seem like a good idea due to the widespread usage of crabbed approached in general aviation. The opposite is true, however. None of twelve approaches tested was stable for the nominal approach conditions; all required final approach speeds in excess of 300 ft/s, save for two exceptions. This result is mildly surprising, and it also is not. Due to the absence of a vertical tail, sideslip has very little effect on the aircraft (also see fig. 4.5). Therefore, keeping wings level and yawing to use thrust to control lateral velocity seems like a good strategy.

Except, it isn't. Yaw authority is maintained throughout all scenarios, but that is exactly what is the issue at hand. The problem lies in the fact that lateral force is not controlled. Therefore, by yawing to the right to generate a velocity to the right, the effectors create a lateral force to the left. It is like rotating a boat to the right by paddling from left to right behind the stern. Heading angle is controlled just fine, but at the cost of generating a force in the wrong direction. When dynamic pressure increases, yaw control can be achieved by smaller deflections, thus generating smaller lateral forces while thrust is about the same or slightly larger.

Things might be different if the aircraft had a vertical tail, as this would largely prevent "drifting" in the wrong direction and therefore enforce yaw control while countering collaterally generated lateral force. Unfortunately, this would defeat the entire purpose of having an agile tailless fighter aircraft with a small RCS, so yawing for crosswind landings is simply a bad idea.

C1

The problem encountered by the B strategy is solved by using the yaw channel to control heading and using DFC to control lateral forces. The initial offset creates overshoot for the windless condition, but response for other crosswind conditions is adequate. What's more, due to the absence of roll-pitch coupling the vertical performance is extremely predictable between crosswind conditions, with vertical error pattern differing at most 10 feet. Lateral reaction is slower than for the A strategies but final command is much more precise.

C2

As the no. 2 vertical strategy does not provide with any stable approaches due to problems similar to A2, this strategy shall not be discussed any further. A note on lateral control though: it is better than for A2 and C1 with the same speeds, but regrettably not of any use.

C3

With the good results of vertical control for A3 and the good lateral control in C1 and C2, one would expect C3 to be the sweet spot for crosswind approach control. Unfortunately, this is not the case. A lot of between-crosswind tuning is needed to obtain satisfactory results (see table B.1), making this strategy unsuitable for variable-wind approaches. In addition, error reduction becomes sequential: first the vertical error is corrected, with lateral error reducing to acceptable levels only after vertical error has done so (see fig. 5.9). The reverse is also possible, depending on the wind condition. The control effector suite simply cannot actively control a nonzero pitch moment and translational forces simultaneously. Control of roll and yaw angle is excellent, however. The mentioned sequentiality causes massive swerves in both lateral and vertical error. The final landing situations are excellent, but the approach is anything but stable for most of the glide slope.

It is possible to solve this issue by re-weighing the control weights used in the INCA algorithm to improve pitch, lateral and vertical control in lieu of roll and yaw. The sequential nature of error reduction now shifts to the less-controlled DoFs and therefore re-weighing is more of a symptom-combating tactic than it is a permanent solution. It also does not improve landing situation.
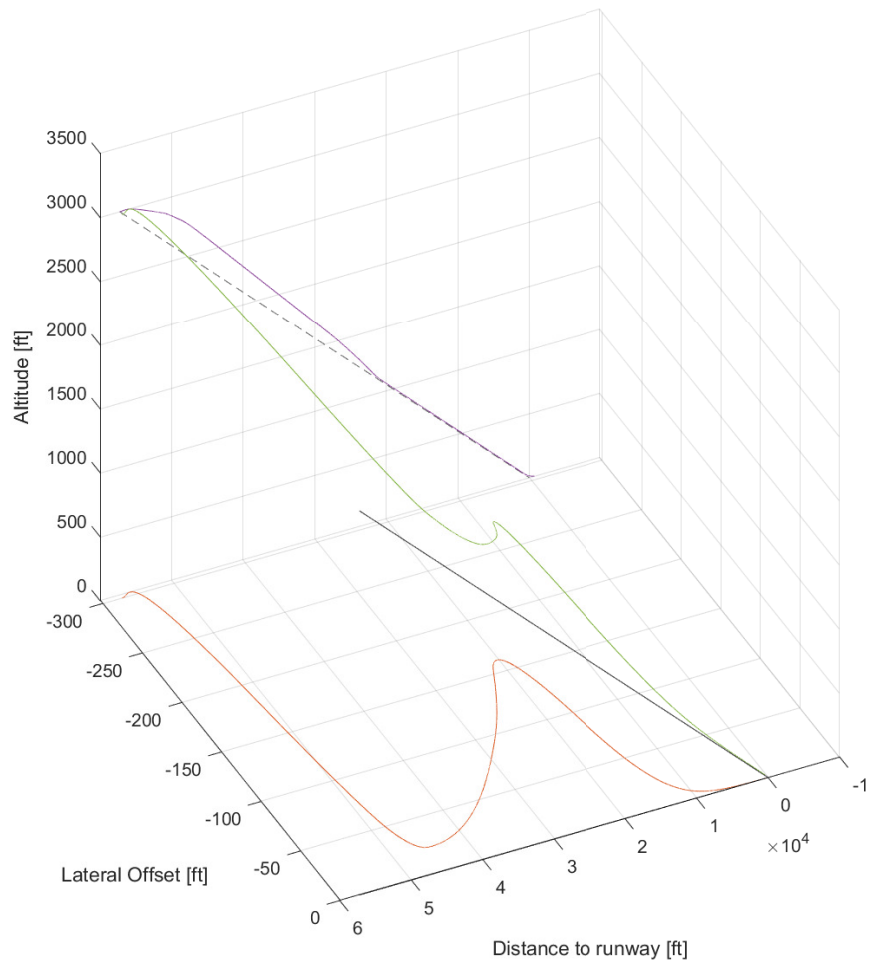
Figure 5.9: Approach with strategy C3 and a crosswind of 20 ft/s with track (green) and projections (red, purple)

6

Conclusions

The work and results presented in chapters 4 and 5 bears some additional reflection and summary. Clearly, a Flight Control System based on DFC is possible and has merit, but what exactly are the strong and weak points of this control philosophy? Section 6.1 recaps the results of the DFC theory and inner loop design (section 6.1.1) and each of the two use cases (sections 6.1.2 and 6.1.3). In addition, section 6.2 treats a number of recommendations that can be drawn from the results and the interpretation thereof.

6.1. Results Interpretation

It can confidently be said that the hypothesis stated in section 3.4 has been proven true: it is indeed possible to control all six Degrees of Freedom simultaneously and independently. Each different situation has its caveats, however, and a number of other observations is stated here as well. Chapter 4 is recapped first, followed by both use cases in order of appearance in chapter 5.

6.1.1. DFC Theory

The main research goal of devising an FCS that is able to employ DFC is realized, which can unequivocally be called a success. It turns out that the INCA method from Matamoros and de Visser (2018) is perfectly suited to handle an extension of the $\Delta\tau_R$ vector, enabling input of both moment and force increments into the CA algorithm. Adaption of other input parameters proved straightforward and yielded a Full-DoF algorithm usable in the DFC FCS. The newly developed method of employing control weights to enable or disable certain DoFs without the need for different set-ups proved extremely useful and might pave the way for seamless flight mode switching.

The inner translational loops are designed in similar fashion to the rotational loops, following its incremental approach. The feedback signals used in these loops – body accelerations, AoA and body velocities – can be assumed to be readily available in a real-life aircraft FCS. Filtering might be in order, but this is outside the scope of this thesis and the point of availability still stands.

In contrast with the rotational loops, no universal hedge was used. A 3DoF translational hedge was initially inserted into the translational inner loops, but this measure greatly deteriorated performance and was therefore left out. A counterargument can be made that this can be expected of a hedge system due to the very purpose of controlling inputs. Because implementing the translational hedge would have interfered with achieving the main research goals, however, the choice was made to disregard universal translational hedging. Instead, a different form of hedging was used: α-hedging was used to limit the maximum commanded vertical acceleration. This prevented unachievable commands from saturating the CA algorithm. In addition, commanded translational accelerations were restricted to ± 40 ft/s in lateral and vertical direction. These proved to be adequate measures to ensure both stability and controllability.

Full DoF control was subsequently achieved by enabling all control weights. Interestingly, near-equal weighting of [1 2 1 0.5 1 1] proved to yield the best results. Initially, the rotational DoFs were heavily prioritized by increasing their weights statically, bit this did not yield any favorable results. Other methods like using the rotational and translational errors as a measure of weighting, either for all groups or between groups, did not

yield better results than the aforementioned weighting settings. The weight for pitch was set to 2 because this prevented vertical force generation from dominating the symmetric DoFs and "hijacking" the control effectors also used for pitch control. The weight for axial acceleration was set to 0.5 because this proved to be the best setting to enable axial control but prevent saturation and deteriorate lateral & vertical control.

6.1.2. Air-to-air refueling

The subject of air-to-air refueling provided the ideal test scenario for DFC control: the system was designed with this use case in mind. The availability of direct translational velocity control should, in theory, be of great assistance to pilots and automatic control systems alike. That hypothesis proved to be true, as the refueling task was executed with more precision and stability by the DFC system compared to the conventional system.

This use case also demonstrated what a DFC control system is *not* designed for: traversing large distances. Travelling large lateral and/or vertical distances is still done best by controlling aircraft attitude and using the airframe's aerodynamic properties instead of using control deflections. It is possible to do so with DFC, but simply not as effective as conventional flight.

When presented with short distances, however, the DFC system can hold its own. Station-keeping in a turn is also done best by an FCS with the ability to employ translational control. By using rotational control to match tanker attitude and translational control to minimize position error, the system performs better than a conventional system using position error as rotational control input. Turbulence is also handled much better by using translational control. This has been proven to be true for both straight flight and steady turns. In short, the automatic DFC system executes the refueling task much better than a conventional system.

6.1.3. High-crosswind landings

Six and three different control strategies for lateral and vertical control, respectively, were designed to test performance on high-crosswind landings with partial or full DFC employment. A standard $3/degree$ glide slope to the start of a runway formed the reference track, with a flare command starting at 30 ft altitude. To better judge lateral error response, a 300 ft lateral offset was implemented.

Roll control and lateral force control provided the best lateral control properties, with yaw control being unstable under any standard circumstance. The benefit of roll control is that it combines better with all vertical modes, although roll-pitch coupling affected initial vertical control when the vertical control mode was pure pitch control. Lateral force control prevents the aforementioned pitch-roll coupling, but does not work well with the hybrid vertical control strategy.

Vertical control is best executed by a hybrid of pitch control based on dynamic pressure and vertical error control by means of vertical force control. Only using translational vertical control is impossible as dynamic pressure falls too far to enable continued upward force generation. Relying solely on pitch control is adequate but induces oscillations when used with lateral roll control and flare execution is not as good as for the hybrid strategy. Therefore, roll control and a hybrid vertical control strategy provide the best results in terms of stability and smoothness.

6.2. Recommendations

Below are a number of recommendations based on both the experiences of the author during the research project as well as the results presented in this thesis. They are given in no particular order.

Investigate the possibility of using a parallel global optimum finder
The INCA algorithm and the Active Set method provide excellent CA performance. The problem with a Jacobian-based approach is that the optimum found – respecting rate and position constraints – is a *local* optimum and not a global one. For rotational control, this is not much of a problem as sustained moments are nearly never necessary and therefore local optima suffice for short time periods.

The issue for translational control is that it *does* employ sustained generation of forces. There were a number of cases in which very small changes in command sequences would result in very different optima for force generation, for example. This clearly illustrates the found optimum's dependence on the actuator deflection path travelled, so to speak. Therefore, there is real merit in finding a global optimum, as this optimum can provide with better CA performance over longer periods of time. An investigation into and successful application of a method to use this approach could yield even better results than the set of results presented in this thesis.

Test the DFC system in manual control tasks
DFC has demonstrated benefits for an automatic control system. A case can be made for the hypothesis that precision manual control tasks will also benefit from DFC FCS usage (also see section 5.1). Until tested, this hypothesis stays exactly that: a presumption based on data from similar-but-not-equal use cases, previous research and intuition.

A study into the manual control performance using a DFC system and comparing this to a conventional baseline therefore is warranted. An affirmative answer to the aforementioned hypothesis could pave the way to more safety, stability and controllability for manual control tasks in specific situations.

Investigate improved weight usage, control loop tuning & adaption and mode switching
The FCS design laid out in this thesis is on the cutting edge of DFC development. Although exciting, the design can be improved by reviewing the usage of CA solver parameters or the usage of the algorithm altogether, control loop structure and feedback loops, and even situation usage. Therefore, the author is of the opinion that there is much to be gained in terms of design improvement. The mentioned examples are but few in a wide variety of improvement possibilities.

Explore connection to other relevant current topics
Research into fault-tolerant control, flight envelope estimation and protection and upset recovery, to name a few, is at the forefront of academic flight control research globally. Perhaps not immediately obvious, DFC usage could be of benefit to such areas. Therefore, reviewing such topics in the light of the findings presented in this thesis might provide new avenues of research or improvement of existing theories and techniques.

$$\text{\Huge A}$$
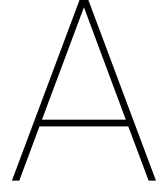
Jacobian Derivation

This appendix treats the complete derivation of the Jacobian intended to form the core of the INDI-based flight control system to be constructed. It is analogous to the Jacobian used in Matamoros and de Visser (2018), with the difference being the fact that the to-be-constructed Jacobian contains the control effectiveness coefficients of all six degrees of freedom instead of only the rotational degrees of freedom. The derivation is split into two parts: the theoretical construction of the derivation of a B-spline and the construction of the Jacobian for this particular spline model.

Spline model Jacobian

As stated in section 3.3, the aerodynamic data made available by Niestroy et al. is converted into a multivariate B-spline model using the method outlined in Tol et al. (2016) to counter aerodynamic uncertainties. Matamoros (2017) gives an excellent description of the spline model structure. Consider for the splines of the total coefficient for each of aerodynamic forces and moments the following construction:

$$
\begin{aligned}
C_i = {} & + C_{i_1}^s(\alpha, M) + C_{i_2}^s(\alpha, \beta, M) + C_{i_3}^s(\alpha, \delta_{\mathrm{ls}}, \delta_{\mathrm{le}}, M) + C_{i_4}^s(\alpha, \delta_{\mathrm{rs}}, \delta_{\mathrm{re}}, M) \\
& + C_{i_5}^s(\alpha, \beta, \delta_{\mathrm{lfi}}) + C_{i_6}^s(\alpha, \beta, \delta_{\mathrm{rfi}}) + C_{i_7}^s(\alpha, \delta_{\mathrm{lfi}}, \delta_{\mathrm{lfo}}, M) + C_{i_8}^s(\alpha, \beta, \delta_{\mathrm{rfi}}, \delta_{\mathrm{rfo}}, M) \\
& + C_{i_9}^s(\alpha, \delta_{\mathrm{lfo}}, \delta_{\mathrm{la}}) + C_{i_{10}}^s(\alpha, \delta_{\mathrm{rfo}}, \delta_{\mathrm{ra}}) + C_{i_{11}}^s(\alpha, \delta_{\mathrm{la}}, \delta_{\mathrm{le}}) + C_{i_{12}}^s(\alpha, \delta_{\mathrm{ra}}, \delta_{\mathrm{re}}) \\
& + C_{i_{13}}^s(\alpha, \delta_{\mathrm{rs}}, \delta_{\mathrm{ls}}, \delta_{\mathrm{pf}}, M) + C_{i_{14}}^s(\alpha, \beta, \delta_{\mathrm{la}}) + C_{i_{15}}^s(\alpha, \beta, \delta_{\mathrm{ra}}) + C_{i_{16}}^s(\alpha, \beta, \delta_{\mathrm{ls}}), \\
& + C_{i_{17}}^s(\alpha, \beta, \delta_{\mathrm{rs}}) + \frac{pb}{2V} C_{i_{18}}^s(\alpha, M) + \frac{q\bar{c}}{2V} C_{i_{19}}^s(\alpha, M) + \frac{rb}{2V} C_{i_{20}}^s(\alpha, M)
\end{aligned}
\tag{A.1}
$$

Where $i = (X, Y, Z, l, m, n)$ and every term $C_{i_n}^s$ is a multivariate B-spline with 0-th order continuity defined over a simplex triangulation.

It is possible to take the directional derivative of each of the spline models constituting C_i in all directions of $\boldsymbol{\delta}$, which is the vector containing all thirteen control effectors. This will give a 6×13 matrix containing the control effectiveness of a particular control effector on a particular aerodynamic force or moment by summing all of the partial derivatives of the 20 spline models for that aerodynamic force or moment. The obtained matrix is the desired Jacobian and is given in eq. (A.2) below.

$$
J(\alpha, \beta, M, \boldsymbol{\delta}) =
\begin{bmatrix}
\sum_{j=1}^{20} \frac{\partial C_{X_j}^s(\boldsymbol{x}, \boldsymbol{\delta})}{\partial \delta_1} & \sum_{j=1}^{20} \frac{\partial C_{i_j}^s(\boldsymbol{x}, \boldsymbol{\delta})}{\partial \delta_2} & \cdots & \sum_{j=1}^{20} \frac{\partial C_{X_j}^s(\boldsymbol{x}, \boldsymbol{\delta})}{\partial \delta_{13}} \\
\sum_{j=1}^{20} \frac{\partial C_{Y_j}^s(\boldsymbol{x}, \boldsymbol{\delta})}{\partial \delta_1} & \sum_{j=1}^{20} \frac{\partial C_{i_j}^s(\boldsymbol{x}, \boldsymbol{\delta})}{\partial \delta_2} & \cdots & \sum_{j=1}^{20} \frac{\partial C_{Y_j}^s(\boldsymbol{x}, \boldsymbol{\delta})}{\partial \delta_{13}} \\
\vdots & \vdots & \ddots & \vdots \\
\sum_{j=1}^{20} \frac{\partial C_{n_j}^s(\boldsymbol{x}, \boldsymbol{\delta})}{\partial \delta_1} & \sum_{j=1}^{20} \frac{\partial C_{n_j}^s(\boldsymbol{x}, \boldsymbol{\delta})}{\partial \delta_2} & \cdots & \sum_{j=1}^{20} \frac{\partial C_{n_j}^s(\boldsymbol{x}, \boldsymbol{\delta})}{\partial \delta_{13}}
\end{bmatrix}
\tag{A.2}
$$

Partial derivative of a B-spline

This section treats the steps necessary to calculate the partial derivative of a simplex polynomial function as presented by Tol et al.. In order to understand what exactly constitutes a B-spline function, first observe a simplex spline function made up of a number of individual polynomials of degree d, each defined on an individual simplex t_j:

$$s(\boldsymbol{x}) = \delta_1(\boldsymbol{x})p^{t_1}(\boldsymbol{x}) + \delta_2(\boldsymbol{x})p^{t_2}(\boldsymbol{x}) + \cdots + \delta_j(\boldsymbol{x})p^{t_j}(\boldsymbol{x}) = \sum_{j=1}^{J}\delta_j(\boldsymbol{x})p^{t_j}(\boldsymbol{x}) \tag{A.3}$$

Here, J is the total number of individual simplices and δ_j is equal to 1 when $\boldsymbol{x} \in t_j$ and zero otherwise. An n-simplex t is defined as the convex hull of a set of $n+1$ unique, nondegenerate points in n-dimensional space:

$$t = \langle \boldsymbol{v}_0, \boldsymbol{v}_1, \dots \boldsymbol{v}_n \rangle \tag{A.4}$$

On this simplex, there exists a local coordinate system known as the barycentric coordinate system, in which each point $\boldsymbol{x}$ on the simplex can be described as a unique weighted vector sum of all of the vertices of the simplex t:

$$\boldsymbol{x} = \sum_{i=0}^{n} b_i \boldsymbol{v}_i \quad \text{with} \quad \sum_{i=0}^{n} b_i = 1 \tag{A.5}$$

The barycentric coordinates of a point $\boldsymbol{x}$ can consequently be calculated as :

$$\begin{bmatrix} b_1 \\ b_2 \\ \vdots \\ b_n \end{bmatrix} = \left[(\boldsymbol{v}_1 - \boldsymbol{v}_0) \quad (\boldsymbol{v}_1 - \boldsymbol{v}_0) \right]^{-1} (\boldsymbol{x} - \boldsymbol{v}_0) = \Lambda(\boldsymbol{x} - \boldsymbol{v}_0) \tag{A.6}$$

From eq. (A.5) it then follows that $b_0 = 1 - \sum_{i=1}^{n} b_i$. Now that all of the barycentric coordinates have been obtained, it is possible to express an individual polynomial $p^{t_j}(b(\boldsymbol{x}))$ in the B-form as

$$p^{t_j}(b(\boldsymbol{x})) = \sum_{|\kappa|=d} c_\kappa^{t_j} \frac{d!}{\kappa!} \prod_{i=1}^{n} b_i^{\kappa_i} = \sum_{|\kappa|=d} c_\kappa^{t_j} B_\kappa^d(b(\boldsymbol{x})) \tag{A.7}$$

This can again be rewritten into a vector notation (see Tol et al. (2014, p.3) for the complete set of steps) as

$$p^{t_j}(b(\boldsymbol{x})) = B_{t_j}^d(b(\boldsymbol{x}))\boldsymbol{c}^{t_j} \tag{A.8}$$

This gives us the vector expression of the B-form definition of an individual polynomial on a simplex t. For the calculation of the gradient of a polynomial in the form shown in eq. (A.8), however, we need an affine expression for the the barycentric coordinates as a function of $\boldsymbol{x}$. This can be achieved by rewriting eq. (A.6) into the following form:

$$\begin{bmatrix} b_1 \\ b_2 \\ \vdots \\ b_n \end{bmatrix} = \Lambda(\boldsymbol{x} - \boldsymbol{v}_0) = \Lambda\boldsymbol{x} - \Lambda\boldsymbol{v}_0 = \Lambda\boldsymbol{x} - \boldsymbol{k}_n \tag{A.9}$$

Calculating b_0 in analogous fashion as before (see Tol et al. (2014, p.10) for details) by using the new definition for $\begin{bmatrix} b_1 & b_2 & \cdots & b_n \end{bmatrix}^T$ and combining this result with eq. (A.9) yields the new definition of $b(\boldsymbol{x})$ on a simplex t:

$$b(\boldsymbol{x}) = \begin{bmatrix} \boldsymbol{a}_1 & \boldsymbol{a}_2 & \cdots & \boldsymbol{a}_n \end{bmatrix}_{t_j} \begin{bmatrix} x_1 \\ x_2 \\ \vdots \\ x_n \end{bmatrix} + \boldsymbol{k} = A_{t_j}\boldsymbol{x} + \boldsymbol{k} \tag{A.10}$$

This definition can be used in the vector expression of the B-form given in eq. (A.8). Now use the multivariable chain rule to obtain the partial derivative of a B-form basis polynomial in the direction of x_i:

$$\frac{\partial B_\kappa^d(b(\boldsymbol{x}))}{\partial x_i} = \frac{\partial B_\kappa^d(b(\boldsymbol{x}))}{\partial b_0}\frac{\partial b_0(\boldsymbol{x})}{\partial x_i} + \frac{\partial B_\kappa^d(b(\boldsymbol{x}))}{\partial b_1}\frac{\partial b_1(\boldsymbol{x})}{\partial x_i} + \cdots + \frac{\partial B_\kappa^d(b(\boldsymbol{x}))}{\partial b_n}\frac{\partial b_n(\boldsymbol{x})}{\partial x_i} = \sum_{k=0}^{n}\frac{\partial B_\kappa^d(b(\boldsymbol{x}))}{\partial b_k}\frac{\partial b_k(\boldsymbol{x})}{\partial x_i} \qquad \text{(A.11)}$$

This summation can be rewritten into vector form:

$$\frac{\partial B_\kappa^d(b(\boldsymbol{x}))}{\partial x_i} = \boldsymbol{a}_i^T \nabla_b B_\kappa^d(b(\boldsymbol{x})) \qquad \text{(A.12)}$$

The above expression can be used to obtain a vector notation of the partial derivative of the entire simplex polynomial $p^{t_j}(b(\boldsymbol{x}))$ with respect to one direction x_i of the total simplex state $\boldsymbol{x}$ using the definition given in eq. (A.7) and taking said partial derivative:

$$\frac{\partial p^{t_j}(b(\boldsymbol{x}))}{\partial x_i} = \frac{\partial}{\partial x_i}\sum_{|\kappa|=d} c_\kappa^{t_j} B_\kappa^d(b(\boldsymbol{x})) = \sum_{|\kappa|=d} c_\kappa^{t_j}\frac{\partial}{\partial x_i} B_\kappa^d(b(\boldsymbol{x})) = \sum_{|\kappa|=d} c_\kappa^{t_j}\frac{\partial B_\kappa^d(b(\boldsymbol{x}))}{\partial x_i} \qquad \text{(A.13)}$$

Now we see the use for the expression derived in eq. (A.12), because it enables reformulation of the partial derivative into:

$$\frac{\partial p^{t_j}(b(\boldsymbol{x}))}{\partial x_i} = \sum_{|\kappa|=d} c_\kappa^{t_j} \boldsymbol{a}_i^T \nabla_b B_\kappa^d(b(\boldsymbol{x})) = \boldsymbol{a}_i^T \sum_{|\kappa|=d} c_\kappa^{t_j} \nabla_b B_\kappa^d(b(\boldsymbol{x})) \qquad \text{(A.14)}$$

Finally, by the same method that enabled conversion of the expression in eq. (A.7) into the expression found in eq. (A.8), the expression in eq. (A.14) can be rewritten (see Tol et al., 2014, p.11) into an expression capable of calculating the partial derivative of a simplex polynomial with respect to a particular direction x_i of the simplex state $\boldsymbol{x}$:

$$\frac{\partial p^{t_j}(b(\boldsymbol{x}))}{\partial x_i} = \boldsymbol{a}_i^T \nabla_b B_\kappa^d(b(\boldsymbol{x}))\boldsymbol{c}^{t_j} \qquad \text{(A.15)}$$

This equation can be used to calculate the partial derivatives of the spline functions $C_{i_n}^s$ (see eq. (A.1)) with respect to one particular control effector δ_j out of the total set of control effectors $\boldsymbol{\delta}$. The sum of the 20 individual partial derivatives then gives the total control effectiveness coefficient of a specific control effector for one of the six aerodynamic forces and moments. The result is the desired Jacobian given in eq. (A.2).

B

Additional Data

B.1. Controller Gains

Basic setup

$$K_{\varphi_1} = \begin{bmatrix} 0.2 & 0 & 0.1 \end{bmatrix} \text{ with } -30\,\text{ft/s} \leq V_{R_{Y_c}} \leq 30\,\text{ft/s} \tag{B.1}$$

$$K_{\varphi_2} = \begin{bmatrix} 0.05 & 0.001 & 0.01 \end{bmatrix} \text{ with } -30° \leq \varphi_c \leq 30° \tag{B.2}$$

$$K_{\theta} = \begin{bmatrix} 0.001 & 0.0001 & 0.0015 \end{bmatrix} \text{ with } -5° \leq \gamma_c \leq 5° \tag{B.3}$$

$$K_{\psi_1} = \begin{bmatrix} 0.2 & 0 & 0.1 \end{bmatrix} \text{ with } -30\,\text{ft/s} \leq V_{R_{Y_c}} \leq 30\,\text{ft/s} \tag{B.4}$$

$$K_{\psi_2} = \begin{bmatrix} 0.02 & 0.000 & 0.01 \end{bmatrix} \text{ with } -30° \leq \psi_c \leq 30° \tag{B.5}$$

$$K_{\omega} = \begin{bmatrix} 2 & 0 & 0.5 \\ 0.5 & 0.01 & 1 \\ 1 & 0 & 0 \end{bmatrix} \tag{B.6}$$

$$K_T = \begin{bmatrix} 1 & 0 & 5 \\ 1 & 0.01 & 1 \end{bmatrix} \tag{B.7}$$

Table B.2: Lookup table data for θ_{dyn} in radians for each mass configuration

	Dynamic Pressure [slug/(ft s^2)]								
	71.14	109.06	162.28	356.16	490.36	652.13	825.77	1000.43	1154.04
lightweight	0.2130	0.1550	0.1087	0.05178	0.04056	0.03491		0.008770	-1.7e-23
nominal	0.2262	0.1856	0.1344	0.06241	0.04846		0.03490	0.006500	
heavyweight	0.2678	0.2031	0.1500	0.06933	0.05361	0.04303	0.01612	0.02928	1.7e-23

Table B.1: Changelog for control parameters for approach trajectories

A	1	0	No changes, stable
		10	No changes, stable
		20	No changes, stable
		30	No changes, stable
	2	0	No changes, unstable in Z, $V_{app} = 350$
		10	No changes, unstable in Z, $V_{app} = 380$
		20	No changes, unstable in Z, $V_{app} = 370$
		30	No changes, unstable in Z, $V_{app} = 360$
	3	0	No changes, stable
		10	No changes, stable
		20	No changes, stable
		30	No changes, stable
B	1	0	No changes, unstable in Y, $V_{app} = 310$
		10	No changes, unstable in Y, $V_{app} = 250$
		20	No changes, unstable in Y, $V_{app} = 350$
		30	$K_{\psi_{2_P}} = 0.04$, unstable in Y, $V_{app} = 420$
	2	0	No changes, unstable in Y and Z, $V_{app} = 350$
		10	No changes, unstable in Y and Z, $V_{app} = 360$
		20	$K_{\psi_{2_P}} = 0.04$, unstable in Y and Z, $V_{app} = 380$
		30	$K_{\psi_{2_P}} = 0.04$, unstable in Y and Z, $V_{app} = 370$
	3	0	No changes, unstable in Y, $V_{app} = 280$
		10	No changes, unstable in Y, $V_{app} = 270$
		20	No changes, unstable in Y, $V_{app} = 350$
		30	unstable in Y and Z, $K_{\omega_{\theta_P}} = 1$, $K_{\psi_{2_P}} = 0.04$ $V_{app} = 320$
C	1	0	No changes, stable
		10	No changes, stable
		20	No changes, stable
		30	No changes, stable
	2	0	No changes, unstable in Z, $V_{app} = 350$
		10	No changes, unstable in Z, $V_{app} = 380$
		20	No changes, unstable in Z, $V_{app} = 360$
		30	No changes, unstable in Y and Z, $V_{app} = 370$
	3	0	$K_{\omega_{\theta_P}} = 2$, $K_{T_{h_P}} = 0.5$, $K_{T_{h_D}} = 4$, stable
		10	$K_{\omega_{\theta_P}} = 2$, $K_{T_{h_P}} = 0.5$, $K_{T_{h_D}} = 4$, stable
		20	$K_{\omega_{\theta_P}} = 2$, $K_{T_{h_P}} = 5$, $K_{T_{h_I}} = 0$, $K_{T_{l_P}} = 0.75$
		30	$K_{\omega_{\theta_P}} = 2$, $K_{T_{h_P}} = 5$, $K_{T_{h_I}} = 0$, $K_{T_{l_P}} = 0.75$

B.2. Approach Data

Table B.3: Settling time pairs [lateral vertical] in seconds for all control strategies and wind conditions. * denotes unstable for standard settings.

	wind	Lateral Strategy		
		A	B	C
	0	[16.42 5.75]	[145.15 18.59]*	[42.28 16.65]
1	10	[17.21 3.23]	[154.38 18.46]*	[37.81 19.29]
	20	[18.03 6.21]	[140.37 17.71]*	[25.13 16.68]
	30	[20.42 20.84]	[113.9 16.11]*	[39.47 16.27]
	0	[16.05 6.66]*	[26.53 9.52]*	[16.57 10.82]*
2	10	[16.83 3.63]*	[18.58 8.89]*	[23.15 11.13]*
	20	[18.21 2.89]*	[19.41 8.73]*	[34.23 25.70]*
	30	[19.66 118.28]*	[135.49 9.09]*	[30.54 27.05]*
	0	[16.11 52.43]	[32.34 50.38]*	[18.24 29.79]
3	10	[16.93 58.55]	[132.86 48.75]*	[20.42 31.84]
	20	[17.54 62.13]	[141.69 58.92]*	[112.29 85.00]
	30	[19.10 30.74]	[144.17 21.63]*	[33.92 99.71]

Table B.4: Lateral 10%-90% rise times in seconds for all control strategies and wind conditions. * denotes unstable for standard settings.

	wind	Lateral Strategy		
		A	B	C
	0	12.04	11.37*	11.40
1	10	12.17	12.73*	20.89
	20	12.32	14.73*	15.04
	30	13.95	14.63*	16.14
	0	11.69*	10.21*	10.91*
2	10	12.00*	12.16*	14.89*
	20	12.67*	11.77*	11.16*
	30	12.53*	14.28*	19.38*
	0	11.86	10.33*	12.55
3	10	12.07	14.30*	15.66
	20	12.38	14.30*	15.66
	30	12.53	14.28*	19.38

Vertical Strategy (row group label for both tables)

Bibliography

James I. Arnold and Frank B. Murphy. B-52 Control Configured Vehicles: Flight Test Results. In *NASA. Dryden Flight Res. Center Advanced Control Technol. and its Potential for Future Transport Aircraft*, page 16. The Boeing Company, Witchita Division, 1973.

Michael A. Bolender and David B. Doman. Method for Determination of Nonlinear Attainable Moment Sets. *Journal of Guidance, Control, and Dynamics*, 27(5):907–914, 9 2004. ISSN 0731-5090. doi: 10.2514/1.9548.

John A. Bowlus, Dieter Multhopp, and Siva S. Banda. Challenges and Opportunities in Tailless Aircraft Stability and Control. *Control*, pages 1713–1718, 1997. doi: 10.2514/6.1997-3830.

Robert V. Brulle. Dive bombing simulation results using direct side force control modes. In *Guidance and Control Conference*, Reston, Virigina, 8 1977. American Institute of Aeronautics and Astronautics. doi: 10.2514/6.1977-1118.

CHRISXTR3M3GAMING. DCS World | Su-27 Cobra Landing on First Attempt!!!!!, 2015. URL https://www.youtube.com/watch?v=tITtO90-wMo&t=66shttps://www.youtube.com/watch?v=tITtO90-wMo.

Wenyao Cui, Jian Liu, Yuanhao Sun, Qibing Li, and Zhixiang Xiao. Airbrake controls of pitching moment and pressure fluctuation for an oblique tail fighter model. *Aerospace Science and Technology*, 81:294–305, 10 2018. ISSN 1270-9638. doi: 10.1016/J.AST.2018.08.016.

Kenneth M. Dorsett and David R. Mehl. Innovative Control Effectors (ICE). Technical report, Lockheed Martin Tactical Aircraft Systems, Fort Worth, TX, 1996.

Kenneth M. Dorsett, Heather P. Houlden, and Scott P. Fears. Innovative Control Effectors (ICE) Phase II. Technical report, Lockheed Martin Tactical Aircraft Systems, Forth Worth, TX, 1997.

Douglas Aircraft Company. Simulator study of Direct-Lift Control during carrier landing approaches. Technical report, Douglas Aircraft Division, 1963.

W.C. Durham. Constrained control allocation. *Journal of Guidance, Control, and Dynamics*, 16(4):717–725, 1993. doi: 10.2514/3.21072.

W.C. Durham. Attainable moments for the constrained control allocation problem. *Journal of Guidance, Control, and Dynamics*, 17(6):1371–1373, 1994a. doi: 10.2514/3.21360.

W.C. Durham. Constrained control allocation: Three-Moment problem. *Journal of Guidance, Control, and Dynamics*, 17(2):330–336, 1994b. doi: 10.2514/3.21201.

Rowena Eberhardt and David Ward. Indirect adaptive flight control of a tailless fighter aircraft. In *Guidance, Navigation, and Control Conference and Exhibit*, pages 466–476, 1999. ISBN 0008-5472. doi: 10.1158/0008-5472.CAN-03-3227.

Wendong Gai, Jie Liu, Jing Zhang, and Yuxia Li. A New Closed-loop Control Allocation Method with Application to Direct Force Control. *International Journal of Control, Automation and Systems*, 16(3):1355–1366, 2018. ISSN 20054092. doi: 10.1007/s12555-017-0294-9.

William Gillard and Kenneth M. Dorsett. Directional control for tailless aircraft using all moving wing tips. In *22nd Atmospheric Flight Mechanics Conference*, pages 51–58, 1997. ISBN 9780000000002. doi: 10.2514/6.1997-3487.

William D. Grantham, Robert W. Sommer, and Perry L. Deal. Simulator study of flight characteristics of a jet-flap STOL transport airplane during approach and landing. Technical report, Langley Research Center, Hampton, VA, 2 1971.

S.L. Grunwald and R.F. Stengel. Design and flight testing of digital direct side-force control laws. *Journal of Guidance, Control, and Dynamics*, 8(2):188–193, 3 1985. ISSN 0731-5090. doi: 10.2514/3.19958.

Ola Härkegård. Efficient active set algorithms for solving constrained least squares problems in aircraft control allocation. In *Proceedings of the 41st IEEE Conference on Decision and Control, 2002.*, volume 2, pages 1295–1300, 2002. ISBN 0-7803-7516-5. doi: 10.1109/CDC.2002.1184694.

Ola Härkegård. Dynamic Control Allocation Using Constrained Quadratic Programming. *Journal of Guidance, Control, and Dynamics*, 27(6):1028–1034, 2004. ISSN 0731-5090. doi: 10.2514/1.11607.

Roger H. Hoh, Thomas T. Myers, Irving L. Ashkenas, Robert F. Ringland, and Samuel J. Craig. Development of Handling Quality Criteria for Aircraft with Independent Control of Six Degrees of Freedom. Technical report, Systems Technology Inc., Hawthore, CA, 1981.

M. Jenkins. Direct side-force control for STOL transport aircraft. In *Guidance and Control Conference*, Reston, Virigina, 8 1973. American Institute of Aeronautics and Astronautics. doi: 10.2514/6.1973-887.

T.A. Johansen and T.I. Fossen. Control allocation - A survey. *Automatica*, 49(5):1087–1103, 2013. doi: 10.1016/j.automatica.2013.01.035.

R.W. Johnson, R.C. Lorenzetti, and G.L. Nelsen. Direct lift control for approach and landing., 1969. ISSN 0021-8669.

Douglas A. Joyce. Flying Beyond the Stall: The X-31 and the Advent of Supermaneuverability, 2014. URL https://ntrs.nasa.gov/search.jsp?R=20170002288.

Z. Liu, Y. Wang, and X. Hao. Coordinated landing control of Unmanned Aerial Vehicle. In *2011 International Conference on Electronics, Communications and Control, ICECC 2011 - Proceedings*, pages 1965–1970, 2011. ISBN 9781457703218. doi: 10.1109/ICECC.2011.6066471.

Ismael Matamoros. *Nonlinear Control Allocation for a High-Performance Tailless Aircraft with Innovative Control Effectors.* PhD thesis, Delft University of Technology, 2017.

Ismael Matamoros and Coen C. de Visser. Incremental Nonlinear Control Allocation for a Tailless Aircraft with Innovative Control Effectors. In *2018 AIAA Guidance, Navigation, and Control Conference*, number 210039, Reston, Virginia, 1 2018. American Institute of Aeronautics and Astronautics. ISBN 978-1-62410-526-5. doi: 10.2514/6.2018-1116.

Walter E. Mcneill, Ronald M. Gerdes, Robert C. Innis, and Jack D. Ratcliff. A Flight Study of Direct Lift Control Flaps to Improve Station Keeping During In-Flight Refuelling. Technical report, Ames Research Center, Moffett Field, CA, 1973.

D.T. McRuer and H.R. Jex. A Review of Quasi-Linear Pilot Models. *IEEE Transactions on Human Factors in Electronics*, HFE-8:231–249, Sept. 1967. ISSN 2168-2852. doi: 10.1109/THFE.1967.234304.

David Mercier and Robert Duffy. Application of direct side force control to commercial transport. In *Guidance and Control Conference*, page 11, Key Biscayne, FL, 8 1973. American Institute of Aeronautics and Astronautics. doi: 10.2514/6.1973-886.

B. Anil Mertol. An Airbrake Design Methodology for Steep Approaches. In *New Results in Numerical and Experimental Fluid Mechanics VI*, volume 96, pages 1–8, Berlin, Heidelberg, 2008. Springer Berlin Heidelberg. ISBN 9783540744580. doi: 10.1007/978-3-540-74460-3.

Clark A. Mitchell and Barbara J. Vogel. The Canard Rotor Wing (CRW) Aircraft–A New Way to Fly. In *AIAA International Air and Space Symposium and Exposition: The Next 100 Years*, page 2517, Reston, Virigina, 7 2003. American Institute of Aeronautics and Astronautics. ISBN 978-1-62410-165-6. doi: 10.2514/6.2003-2517.

Csaba Moravszki, József Rohács, and Gottfried Sachs. Tunnel/Predictor Display for Trajectory Control in Hypersonic Flight. *Periodica Polytechnica Transportation Engineering*, 3 2018. ISSN 1587-3811. doi: 10.3311/PPtr.10342.

Tim Morgan. How Fighter Jets Lock On (and How the Targets Know). URL https://gizmodo.com/how-fighter-jets-lock-on-and-how-the-targets-know-1644871272.

NATO Standardization Organization. NATO Standard ATP-3.3.4.2 Air-to-Air Refuelling ATP-56 Edition C Version 1. Technical report, NATO, 2013.

Anhtuan Ngo, William Reigelsperger, Siva Banda, and John Bessolo. Multivariable control law design for a tailless airplane. In *Guidance, Navigation, and Control Conference*, number July, pages 1–11, Reston, Virigina, 7 1996. American Institute of Aeronautics and Astronautics. doi: 10.2514/6.1996-3866.

Michael A. Niestroy, Kenneth M. Dorsett, and Katherine Markstein. A Tailless Fighter Aircraft Model for Control-Related Research and Development. In *AIAA Modeling and Simulation Technologies Conference*, 2017. ISBN 978-1-62410-451-0. doi: 10.2514/6.2017-1757.

W.J.G. Pinsker. The Control Characteristics of Aircraft Employing Direct-Lift Control. Technical report, Aerodynamics Dept., R.A.E., Bedford, 1968.

L. Stewart Rolls, Anthony M. Cook, and Robert C. Innis. Flight-determined aerodynamic properties of a jet-augmented, auxiliary-flap, direct-lift- control system including correlation with wind-tunnel results. Technical report, Ames Research Center, Mofett Field, CA, 7 1969.

Edmund G. Rynaski and Norman C. Weingarten. Flight Control Principles for Control Configured Vehicles. Technical report, Cornell Aeronautical Laboratory Inc., Buffalo, NY, 1972.

Gottfried Sachs and Florian Holzapfel. Predictor-Tunnel Display and Direct Force Control for Improving Flight Path Control. In *AIAA Guidance, Navigation and Control Conference and Exhibit*, number August, Reston, Virigina, 8 2008. American Institute of Aeronautics and Astronautics. ISBN 978-1-60086-999-0. doi: 10.2514/6.2008-6644.

San Diego Air and Space Museum. F 2248 General Dynamics F-16 Falcon Control Configured Vehicle, 2015. URL https://www.youtube.com/watch?v=xiX07hscvS8.

Gunther Schänzer. Direct lift control for flight path control and gust alleviation. In *AGARD CONFERENCE PROCEEDINGS No. 240 Guidance and Control Design Considerations for Low-Altitude and Terminal-Area Flight*, pages 289–302, Dayton, OH, 1977.

Carl A. Shollenberger, John W. Humphreys, Frank S. Heiberger, and Robert M. Pearson. Results of Winglet Development Studies for DC-10 Derivatives. NASA Contractor Report 3677, McDonnell Douglas Corporation, March 1983.

S. Sieberling, Q.P. Chu, and J.A. Mulder. Robust Flight Control Using Incremental Nonlinear Dynamic Inversion and Angular Acceleration Prediction. *Journal of Guidance, Control, and Dynamics*, 33(6):1732–1742, 11 2010. ISSN 0731-5090. doi: 10.2514/1.49978.

Jeremy J. Smith. Simulation of the Dynamically Coupled KC-135 Tanker and Refueling Boom. Master's thesis, Air Force Institute of Technology, March 2007.

Joseph W. Stickle, James M. Patton, and Robert C. Henry. Flight tests of a direct lift control system during approach and landing. Technical report, Langley Research Center, Langley Station, VA, 1968.

Charles R. Taylor Jr. Flight test results of a trailing edge flap designed for direct-lift control. Technical report, The Boeing Company, Seattle, WA, 1969.

H.J. Tol, Coen C. de Visser, Erik-Jan Van Kampen, and Q.P. Chu. Nonlinear Multivariate Spline-Based Control Allocation for High-Performance Aircraft. *Journal of Guidance, Control, and Dynamics*, 37(6):1840–1862, 11 2014. ISSN 0731-5090. doi: 10.2514/1.G000065.

H.J. Tol, Coen C. de Visser, L.G. Sun, Erik-Jan Van Kampen, and Q.P. Chu. Multivariate Spline-Based Adaptive Control of High-Performance Aircraft with Aerodynamic Uncertainties. *Journal of Guidance, Control, and Dynamics*, 39(4):781–800, 2016. ISSN 0731-5090. doi: 10.2514/1.G001079.

Andrzej Tomczyk. Evaluation of maneuverability of aircraft equipped with direct lift control system. In *23rd Atmospheric Flight Mechanics Conference*, pages 174–181, 1998.

Andrzej Tomczyk. Aircraft maneuverability improvement by direct lift control system application. *Aerospace Science and Technology*, 9(8):692–700, 2005. ISSN 12709638. doi: 10.1016/j.ast.2005.09.004.

United States Navy. *NATOPS FLIGHT MANUAL NAVY MODEL F-14D AIRCRAFT*. United States Navy, 2004. doi: NAVAIR01-F14AAD-1.

D.J. Van Oorspronk. *Upset Recovery Controller Based on Maximum Control Effectiveness for a High-Performance Over-Actuated Aircraft*. PhD thesis, Delft University of Technology, 2018.

Ronald van 't Veld, Erik-Jan Van Kampen, and Q.P. Chu. Stability and Robustness Analysis and Improvements for Incremental Nonlinear Dynamic Inversion Control. In *2018 AIAA Guidance, Navigation, and Control Conference*, Reston, Virginia, 1 2018. American Institute of Aeronautics and Astronautics. ISBN 978-1-62410-526-5. doi: 10.2514/6.2018-1127.

Xuerui Wang, Erik-Jan Van Kampen, and Q.P. Chu. Gust Load Alleviation and Ride Quality Improvement with Incremental Nonlinear Dynamic Inversion. In *AIAA Atmospheric Flight Mechanics Conference*, Reston, Virginia, 1 2017. American Institute of Aeronautics and Astronautics. ISBN 978-1-62410-448-0. doi: 10.2514/6.2017-1400.

Xuerui Wang, Erik-Jan Van Kampen, Q.P. Chu, and Peng Lu. Stability Analysis for Incremental Nonlinear Dynamic Inversion Control. In *2018 AIAA Guidance, Navigation, and Control Conference*, Reston, Virginia, 1 2018. American Institute of Aeronautics and Astronautics. ISBN 978-1-62410-526-5. doi: 10.2514/6.2018-1115.

Zhiqiang Zhou. Nonlinear decoupling control of aircraft motion. *Journal of Guidance, Control, and Dynamics*, 18(4):812–816, 7 1995. ISSN 0731-5090. doi: 10.2514/3.21463.